JMIR Biomedical Engineering

Engineering for health technologies, medical devices, and innovative medical treatments and procedures
Volume 10 (2025) ISSN 2561-3278 Editor in Chief: Javad Sarvestan, PhD

Contents

Review

Original Papers

Research Letter

Review

Cardiac Repair and Regeneration via Advanced Technology: Narrative Literature Review

Yugyung Lee[1], PhD; Sushil Shelke[1], BS; Chi Lee[1], PhD

Division of Pharmacology and Pharmaceutics Sciences, School of Pharmacy, University of Missouri Kansas City, Kansas City, MO, United States

Corresponding Author:
Chi Lee, PhD
Division of Pharmacology and Pharmaceutics Sciences
School of Pharmacy
University of Missouri Kansas City
5000 Holmes St
Kansas City, MO, 64110
United States
Phone: 1 8162352408
Fax: 1 8162355990
Email: leech@umkc.edu

Abstract

Background: Cardiovascular diseases (CVDs) are the leading cause of death globally, and almost one-half of all adults in the United States have at least one form of heart disease. This review focused on advanced technologies, genetic variables in CVD, and biomaterials used for organ-independent cardiovascular repair systems.

Objective: A variety of implantable and wearable devices, including biosensor-equipped cardiovascular stents and biocompatible cardiac patches, have been developed and evaluated. The incorporation of those strategies will hold a bright future in the management of CVD in advanced clinical practice.

Methods: This study employed widely used academic search systems, such as Google Scholar, PubMed, and Web of Science. Recent progress in diagnostic and treatment methods against CVD, as described in the content, are extensively examined. The innovative bioengineering, gene delivery, cell biology, and artificial intelligence–based technologies that will continuously revolutionize biomedical devices for cardiovascular repair and regeneration are also discussed. The novel, balanced, contemporary, query-based method adapted in this manuscript defined the extent to which an updated literature review could efficiently provide research on the evidence-based, comprehensive applicability of cardiovascular devices for clinical treatment against CVD.

Results: Advanced technologies along with artificial intelligence–based telehealth will be essential to create efficient implantable biomedical devices, including cardiovascular stents. The proper statistical approaches along with results from clinical studies including model-based risk probability prediction from genetic and physiological variables are integral for monitoring and treatment of CVD risk.

Conclusions: To overcome the current obstacles in cardiac repair and regeneration and achieve successful therapeutic applications, future interdisciplinary collaborative work is essential. Novel cardiovascular devices and their targeted treatments will accomplish enhanced health care delivery and improved therapeutic efficacy against CVD. As the review articles contain comprehensive sources for state-of-the-art evidence for clinicians, these high-quality reviews will serve as a first outline of the updated progress on cardiovascular devices before undertaking clinical studies.

(JMIR Biomed Eng 2025;10:e65366) doi:10.2196/65366

KEYWORDS

advanced technologies; genetics; biomaterials; bioengineering; medical devices; implantable devices; wearables; cardiovascular repair and regeneration; cardiac care; cardiovascular disease

Introduction

Cardiovascular diseases (CVDs) are the leading cause of death globally, accounting for an estimated 17.9 million deaths in 2019 according to a report from the World Health Organization. Almost one-half of all adults in the United States have at least one form of heart disease [1]. Myocardial infarction (MI) is caused by ischemia in the coronary artery, primarily due to blocked arteries resulting from atherosclerosis [2]. This blockage damages the myocardium, reducing its contractile capacity, which leads to a decreased ejection fraction and, ultimately, heart failure [3]. In the United States, one healthy heart becomes infarcted every 40 seconds [4].

Preserving tissue and cellular function is crucial for maintaining heart functionality. Numerous signaling pathways and genetic factors associated with MI survival have been periodically reviewed [5-7]. There is a growing emphasis on understanding the mechanisms involved in myocardial repair and regeneration [8]. Reports from organizations such as the Transnational Alliance for Regenerative Therapies in Cardiovascular Syndromes highlight the importance of these mechanisms. Key principles affecting reparative and regenerative potential include survival and protection, cell-cell communication, angiogenesis and vascularization, cardiomyogenesis, molecular regulation of the cell cycle and proliferation, inflammation reduction, and cardiac aging [7,9].

An increase in reactive oxygen species (ROS) is a hallmark of ischemic cardiomyopathy [10]. ROS, such as hydrogen peroxide (H_2O_2) and hydroxyl radicals, play a significant role in MI and can be considered ideal regulators for patients post-MI [11]. The concentration of H_2O_2 in healthy cells is about 0.02 mM, whereas intracellular concentrations above 0.1 mM induce oxidative stress and cell death [12,13]. Given that extracellular H_2O_2 concentrations can be 10 to 100 times higher than intracellular levels [14], careful monitoring of H_2O_2 levels in cells is essential for prevention and treatment. As ROS play an integral role in platelet aggregation and vasodilation, inhibitors of vasodilation and platelet aggregation are commonly adapted as a therapeutic means against MI [15].

Regarding the treatment methods against CVD, organ transplant has been the most efficient strategy. Despite the preference for organ donor replacement in treating CVD, the shortage of organ donors has driven significant research into human-scale cardiovascular organs and functional tissue substitutes [16,17]. Challenges such as complex fabrication processes [18], poor mechanical properties [19], and biocompatibility and immunogenic issues [20] remain unresolved.

Designing prostheses requires fabricating matrix constructs with complex shapes and sizes for clinical applications [21]. Prostheses and implantable devices have varying requirements that are categorized into chemical, mechanical, electrical, and thermal characteristics [22]. Additionally, these devices must be biocompatible, be nonimmunogenic, and maintain functional capabilities within the body's biological environment [23]. Although serious infections or side effects from cardiovascular prostheses are rare, infected prostheses can be fatal [24].

Hydrogels, which are hydrophilic polymeric scaffolds with unique 3-dimensional structures, can absorb large amounts of water or biological fluids, making them potential candidates for cardiovascular tissue engineering [23]. Various synthetic and natural polymers are used in implantable hydrogels, with natural polymers like collagen offering higher immunity and biodegradable properties over synthetic ones.

This review focused on genetic variables in CVD, advanced technologies, and biomaterials for organ-independent cardiovascular repair systems (Figure 1). A variety of implantable and wearable devices, including biosensor-equipped cardiovascular stents and biocompatible cardiac patches, have been developed and evaluated. Finally, future research directions in the rapidly evolving fields of 3D-printed biomedical devices, artificial intelligence (AI), and multifunctional sensing devices are discussed.

Figure 1. Cardiac repair and regeneration via advanced technologies and gene therapy.

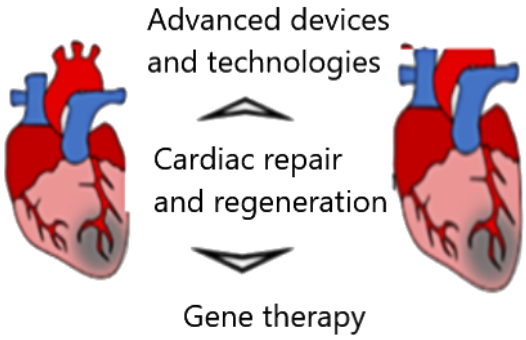

Advanced Assessment Technologies for Cardiac Image and Genetic Factors

Image Features Extracted From Imaging Modalities

Risk variables used for the classification of CVD progression include radiological imaging features and genetic factors. The complex nature of cardiovascular structures makes stenosis assessment from image modalities a serious challenge. In general, imaging features are considered radiomic-based biomarkers or indicators rather than pathological symptoms. An assessment of imaging features can serve as a quantitative index extractable from such imaging modalities as magnetic resonance imaging, computed tomography angiography (CTA), and optical coherence tomography [25]. Even though a semiquantitative estimation of coronary stenosis is feasible via

a thorough assessment of image features over an extended period, this process requires advanced technology expertise and labor-intensive effort.

In particular, coronary CTA, a noninvasive examination technique, plays an integral role in the evaluation and treatment of coronary artery disease (CAD) [26]. For instance, dual-source CTA allows for improved resolutions of implantable devices, including intrinsically higher-density stents, whose adversities are due to distortion reduction stemming from thick strut slices [27]. This approach makes it possible to conduct advanced cardiac imaging analysis, even though its invasive nature sometimes yields a high risk of fatality and complications [28-30].

As the number of images exponentially grows, the lack of ability to accurately label those images causes intrinsic limitations in the interpretation of the data [31]. A recent surge of AI techniques could serve as an ideal solution, enhancing the accuracy of a quantitative assessment of segmented features, including intima-media thickness ascertained by such computed algorithms as convolutional neural networks, UNet, UNet+, and DenseNet [32]. AI techniques and associated programmed models are for accurate identification of patterns, abnormalities, and defects in images, leading to enhanced efficiency and a reduction in errors inherent in human inspection [33].

Evolving Gene Therapy Against CVD

Genetic Factors in the Assessment of CVD Risk

Genes are involved in most cardiovascular functions, starting with the robustness of blood vessels to the way cells interact. People with a family history of heart disease could share common environmental factors, such as the intake habits of drinking water and daily food and exposure to chemicals, including carbon monoxide, in the air. As most cardiac disorders, including arrhythmias, congenital heart disease, cardiomyopathy, and high blood cholesterol, can be inherited [34], assessing genetic variants or biomarkers to identify at-risk individuals is integral to the prevention and treatment of CVD [35].

Genetic variations acquired by children from parents in the DNA of the eggs and sperm can influence every cell of a child's body, not only in the development process but also in the onset of heart disease [36]. An 8-year follow-up study found that CVD risk increased by 75% with a paternal history and about 60% with a maternal history of premature CVD, implying that certain genes can significantly enhance the risk of heart disease [37]. In the same study, a 16-year follow-up investigation found that a family history of premature CAD (age <50 years) marked a 44% higher risk of CVD mortality.

The pooled cohort equations for risk classification have been adapted based on genetic variants and medication decisions, including statins [38]. On the other hand, polygenic risk score (PRS) generation based on the relationships between the amount and frequency of genetic variants and the onset of specific diseases [39-41] has been explored for the assessment of genetic risk and extrapolation of individual outcomes [42]. The PRS could be accompanied by family history, lifestyle, and environmental factors [43,44] and fortified with emerging technologies, including proteomics, when determining an individual's genetic predisposition to CVD [45,46]. PRS mostly outperforms traditional risk scores in the prediction of individual outcomes, and additional AI-based transfer learning could further upgrade the relatively less accurate performance on translating PRS from ancestry to different ethnicities that are mostly unknown and unvalidated [47].

Genes that could reduce the development of plaque around infected regions would prevent neointimal formation [48]. The primary CVD endogenous biological variants include C-reactive protein, a liver protein released in response to inflammation [8,49], and plasma levels of low-density lipoprotein cholesterol [50], a seminal risk factor for the development of coronary heart disease. In addition, pro-inflammatory CD4+ cells with CD28 expression [49,51], cardiac troponin I [52], and the number of regulatory T lymphocytes [53] are frequently examined as specific biomarkers for the diagnosis of acute MI. Also, specific genes (eg, APOB, LDLR, and PCSK9 genes for familial hypercholesterolemia and BAG3, LMNA, MYH7, PLN, RBM20, SCN5A, TTN, TNNC1, TNNI3, TNNT2, and TPM1 genes for dilated cardiomyopathy) were recommended by the American Heart Association to be tested for the diagnosis of monogenic CVDs [54].

Along with those biological variants, pathological genetic factors or symptoms assessed for CVD include carotid intima thickness [55,56] and vascular function (which occur in the early stage of familial hypercholesterolemia) [57,58]. Detection of those genetic markers as part of familial cascade screening programs in familial hypercholesterolemia can lead to preventive effects, where subsequent medical therapy can lower long-term CVD risk [55,59]. A combined application of various genetic factors based on each patient's genetic profile may guarantee an efficient treatment strategy against CVD [35].

Even though genetic factors play a significant role in developing conditions of CVD, the screening processes including a health DNA test can only reveal certain genetic mutations that increase the risk and responses [60]. Subsequently, the relationship between genetic factors and risk scores is sometimes poor due to the fact that those having the genetic mutation do not necessarily have the same lifestyle factors, including basic health measures. Therefore, proper statistical approaches along with the results from clinical studies including model-based risk probability prediction from each or combined genetic variables are integral for genetic-based prediction of the CVD risk [61].

AI for Cardiovascular Gene Therapy

Genes (DNA, small interfering RNA, and microRNA) that could interfere with the development of plaque around infected regions are conjugated on biomedical devices like cardiovascular stents to prevent neointimal formation. An advanced monitoring process of genetic data and clinical data from electronic health records could lead to a fast and precise clinical decision and achieve customized treatment, eventually alleviating CVD via the detection of CVD symptoms at an early stage. However, the efficiency of cardiovascular gene therapy has been hampered by some obstacles, such as insufficient gene propagation, a lack of delivery mechanisms, and insufficient cell-vector interactions [62]. Moreover, health care providers may negatively influence

clinical outcomes due to the lack of discipline in the treatment algorithms and the absence of established regulations to handle early-onset data [63,64].

Combined AI models will address highly complicated cardiovascular clinical genetics [65]. AI profoundly apprehends complex patterns in imaging profiles and offers quantitative assessments of radiographic properties, serving as a valuable tool for enhancing imaging postprocessing. For instance, a combined convolutional neural network and recurrent neural network has achieved enhanced accuracy in predicting stenosis (≥50%) upon examining genetic variables grouped into training and testing samples [32,66]. This approach has obtained similar outcomes in the quantitative assessment of the growing number of segmented image features, including intima-media thickness for CVD [31,32].

In general, the advanced technology involved with AI is revolutionizing the method that ensures the accuracy, completeness, consistency, and validity of clinically applicable gene data [67]. In parallel, researchers should follow established guidance on using information from the digital world, as several guidelines have already been issued by institutional review boards to properly maintain genetic data integrity [68]. As a result of the increase in genetic testing and the fear of privacy breaches by health providers, employers, and society, the disciplines of ethics, public health, and genetics have also emerged. The health professional should make a compromise between providing proper arrangements for patient care and protecting personal privacy. In the near future, the adaptation of AI in radiomics will lead to precise and automated analysis of genetic variables involved with disease onset and progress.

Telehealth Genetic Counseling Between Patients and Genetic Counselors

To improve the efficacy of the diagnosis and assessment of CVD risk, the prediction tools, including telehealth systems, should assess endogenous genetic compounds involved with heart failure, atherosclerosis, and CAD [67,69]. Telehealth genetic counseling, including videoconferencing and telephone counseling, was compared with in-person genetic counseling for the degree of outcomes specific to patient experiences and accessibility to various treatment methods. The patients expressed the highest satisfaction with genetic counseling provided by media devices, such as telephone and video [70-72]. Moreover, telehealth genetic counseling is considered equitable to in-person genetic counseling across numerous domains, even though those studies were conducted with telehealth systems that were less robust and accurate than what is available today.

The benefits and limitations of telehealth from the perspectives of the patients and genetic counselors have been thoroughly examined to resolve potential uncertainty in the analysis processes [73-75]. Those limitations include technical challenges, difficulty in rapport and the subsequent psychosocial issues, and lack of clinical complement [74,76]. There needs to be some conceptual changes in the current status of telehealth approaches over time, providing continuous advancement in involved technologies [76,77].

Mobile Sensors for Cardiovascular Information Systems

Remote monitoring is considered the ambulatory tracing of vital signs and other medical indicators of a patient's health and recovery status via a telemedicine system without the patient meeting doctors or being present in the clinic (Figure 2) [78]. The Food and Drug Administration has recognized the importance of devices such as continuous temperature monitoring or continuous glucose monitoring devices that allow health care providers to remotely monitor patients, including those that measure body temperature, respiratory rate, heart rate, and blood pressure. In addition, a new approach based on advanced technologies for various physiological variables and biomarkers has performed continuous in-time monitoring as well as subsequent customized treatment strategies.

Figure 2. Schematic Representation of Remote Monitoring System of Biosensor/Cardiac Implantable Electronic Device.

The current roles of mobile sensors explored in telehealth technologies and further challenges in CVD will specifically emphasize (1) accurate assessment and diagnosis of vital signs or biomarkers from CVDs, (2) reliable and reproducible sensing systems to monitor the progress of a patient's disease status, and (3) wearable devices with maintenance of battery life and restoration of interaction sensitivity capable of assessing cardiovascular information of patients at risk [79-81].

The problem arises when analyzing data from mobile sensors due to a lack of normalization and implementation of proprietary interfaces to the respective device or platform. In daily life, numerous portals provided by each sensor manufacturer should be simultaneously traced and aggregated into the existing database for each cardiovascular patient [82]. Thus, the integration of data obtained from patients with heart failure or implantable cardiac devices needs to be properly conducted to store data in a structured and interoperable way for timely clinical and scientific evaluations [83,84].

Advanced Systems Currently Available for CVD

Biomaterials for Organ-Independent Cardiovascular Repair Systems

Required Properties for Organ-Independent Cardiovascular Repair Systems

The highly ordered myocardium capacity for electrical integrity and electrical conduction between healthy and infarcted cells starts to diminish as the relatively disordered fibrous scar tissue disposition increases in the myocardium, leading to systolic and diastolic dysfunction and cardiac arrhythmia [85]. As heart transplantation is limited due to a shortage of organ donors, organ-independent systems, including cardiac patches, grafts, and scaffolds, play an essential role in cardiac repair and treatment of MI [86].

Biomaterial systems function like normal cardiac tissues, providing excellent electrical conductivity, mechanical strength, and biological activities to infarcted heart tissues [87]. Novel biomaterial-based systems offer self-renewal and regeneration in the damaged heart, serving as various resources for cardiac tissue repair for those with CVD. For instance, cardiac patches provide mechanical support to the myocardial wall and passively prevent the infarcted myocardium following MI by reducing myocardial wall stress and preventing left ventricular dilation and remodeling [88].

Hydrogels for Organ-Independent Cardiovascular Repair Systems

Hydrogels are soft and moist injectable biomaterials with properties similar to those of human soft tissues. They are minimally invasive and serve as a vehicle for the delivery of therapeutic agents in situ [89,90]. Conductive hydrogel systems based on low-dimensional inorganic nanomaterials, such as carbon nanotubes and graphene derivatives [23], and simultaneously loaded with stem cells, growth factors, cytokines, or oligonucleotides, are found to alleviate cardiac casualties by promoting angiogenesis and cardiomyocyte proliferation and reducing fibrosis and apoptosis.

In addition, a complex hydrogel patch is produced by principles of fabrication via Fe^{+3}-induced ionic coordination between a homogeneous network of dopamine-gelatin conjugates and dopamine-functionalized polypyrrole [91]. The Schiff base reaction between oxidized sodium hyaluronic acid and hydrazided hyaluronic acid was explored to form an injectable hydrogel patch. Added bioactive peptides, a 7-amino acid peptide, loaded in collagen-based hydrogel reduced cell apoptosis, enhanced Sca-1+ recruitment and differentiation of stem cells, and enhanced neovascularization formation, which resulted in improved heart function in a mouse MI model [90].

Cardiac Patch

Therapeutic Patch as an Effective Strategy

All the delivery methods for MI recovery drugs, primarily via the oral route but occasionally via an intravenous route, direct injection to the heart, and drug-eluting stents, have their own limitations in resolving MI-induced loss of cardiomyocytes [92]. Advanced formulations, including cardiac patches, have demonstrated their efficiencies in functional recovery for drug carriers with targeted and local delivery of cardiovascular drugs, nutrients, and cells. Moreover, patches not only are capable of providing necessary mediators in multiple therapies to recover the affected area but also strengthen the damaged area with induced cell attachment and proliferation [93].

Types of Patches and Their Applications for MI Recovery

Therapeutic patches are divided into two types based on the presence or absence of cells: cell-based patches and acellular patches. As there is a lack of regeneration of cardiomyocytes, cells such as human-induced pluripotent stem cells, mesenchymal stem cells, and skeletal myoblasts are often introduced to restore cardiac function [94].

Newly introduced cells can lead to enhanced angiogenesis, lowered fibrosis, and apoptosis of cardiomyocytes [2]. Due to the inefficiency of generating new heart tissue from cardiomyocytes, acellular cardiac patches, which might include paracrine factors such as proteins, RNA, growth factors, or small molecules, are occasionally explored to accomplish cardioprotective effects [95].

The biocompatibility of the source biomaterial often entails a serious challenge in designing any implantable patches [96]. Moreover, the biomaterial should be similar to that of host tissues from the perspectives of biochemical, mechanical, and topographical properties [97,98]. For instance, poly(hydroxyethyl) methacrylate (pHEMA) polymer has demonstrated biocompatibility and has been used for biomedical applications, including drug delivery [99,100], contact lenses [101,102], and tissue engineering [103,104]. However, the low viscous nature of pHEMA makes it a challenging task to develop pHEMA-based biomedical devices, including a cardiac patch that is capable of successfully delivering agents like ROS scavengers against MI.

3D Printing Technology for Cardiac Patch Development

3D printing can be used to create patient-specific devices, such as organ implants and tissue models that mimic human physiology. 3D printing can generate surgical planning models and reduce the need for animal testing. 3D printing can be used to create personalized medicines and their delivery systems that specifically adapt to each patient's genetic makeup [105].

There are numerous methods, including electrospinning, solvent evaporation, and decellularization, used for the development of patches [106]. Each of these methods has its own challenges, such as material selectivity, limitations in complex shapes, and cost and time efficiency [107]. Additionally, 3D printing has emerged as a low-cost and fast method to develop patches produced from a vast range of materials with the utmost efficacy.

As previously mentioned, a novel patch based on biocompatible pHEMA polymers was developed with the aid of direct-light 3D printing technology. Stereolithography-based 3D printing, where the ink is placed on a platform, was successfully used to prepare 3D-printed acellular cardiac patches or cardiovascular stents [21]. In 3D-printed systems, the immunosuppressive drug, like sirolimus, dispersed within the patch matrix will be released when the linker, like an ROS-responsive thioketal linker, that connects the polymers is cleaved [108]. The ratio of the polymer and crosslinker can be customized to achieve controllable drug release.

3D- or 4D-Printable Smart Devices for CVD

3D printing provides geometric flexibility, which has been explored to produce metal or polymer-embedded 3D construct microsystems with high flexibility [23,109]. 3D-printed systems or smart devices use advanced materials with characteristics such as thermal and electrical conductivity and piezo-resistivity [110]. Electric units or components, including resistors, capacitors, inductors, circuits, and passive wireless sensors and batteries, have been incorporated into 3D-printed products for potential practical applications.

3D tactile sensors capable of detection and differentiation of human movements, including pulse monitoring and finger motions via detection of endogenous compounds, were fabricated using multimaterial, multiscale, and multifunctional approaches under ambient conditions conformally onto freeform surfaces [111]. As lactate levels have been associated with heart failure as well as diabetes, the portable luminometer, a disposable minicartridge produced by 3D printing and stored in cell phones, was used to detect chemiluminescence from enzyme-coupled reactions [112]. Lactate oxidase was coupled with horseradish peroxidase to noninvasively detect the lactate levels within 5 minutes at a detection limit of 0.5 mM/L and 0.1 mM/L in oral fluids and sweat, respectively.

By adapting AI to additive manufacturing, 3D designers can optimize cardiovascular biosensors or implants to be more efficient and robust. AI-mediated 3D printing tools can synchronize with high-quality imaging data, such as computed tomography and magnetic resonance imaging scans, and generate personalized designs, enabling thorough control over the otherwise unavoidably complicated, time-consuming, and exhaustive process [3].

An optimal combination of 3D printing based on novel or hybrid 3D printing methods and AI can achieve the next generation of cardiovascular systems [113]. Subsequently, advanced 3D or 4D printing, once nearly overcoming the cost and scalability barriers, could lead to more effective and targeted treatments against CVD, accomplishing improved treatment outcomes and enhanced health care delivery [67].

Advanced Cardiovascular Stents for CVD

Gene-Eluting Stents

Advanced biomedical gene carriers have been intensively explored in vascular cell biology and CVD treatment. The identification of critical regulators, such as noncoding RNAs, including microRNA, long noncoding RNA, and circular RNA presence in such cell types as vascular smooth muscle cells, endothelial cells, and macrophages, has served as an efficient therapeutic target in the field of CVD.

Among biomedical carriers, multifunctional gene-loaded stents and integrated stents equipped with self-reporting sensors are often explored as promising technologies against CVD, including atherosclerosis and MI [114,115]. Cardiovascular stents keep the vessel open and prevent it from re-occluding (ie, restenosis), but vessel injury by stent struts leads to the activation of platelets and mural thrombus formation, leading to the activation of circulating neutrophils and tissue macrophages [116-118]. As the cardiovascular stent produces late-stage restenosis [119,120], people with stents are at risk of high blood pressure. Therefore, it is integral to find a more advanced and sensitive stent capable of real-time monitoring of blood flow.

Gene-loaded stents coated with synthetic and natural polymers such as polylactic-polyglycolic acid (PLGA), collagen, hydroxyapatite, and matrix metalloproteins can overcome major limitations of cardiovascular gene therapy, including insufficient cell-vector interactions, a lack of delivery mechanisms, and insufficient gene propagation [121]. Gene-loaded stents also allow for maintaining a curative gene, serving as a carrier to convey the gene and administer the vector and avoiding immune responses [62].

The first successful in vivo transfection of green fluorescent protein plasmid DNA loaded in a DNA-PLGA coated stent was efficiently expressed in cell cultures (7.9%, SD 0.7% vs 0.6%, SD 0.2% control; $P<.001$) of rat aortic smooth muscle cells [122]. In addition, PLGA nanoparticle-coated stents encapsulated with vascular endothelial growth factor and paclitaxel [123] or Ang-1 proteins [124] were developed as an alternative therapy, reducing in-stent restenosis and accomplishing complete re-endothelialization. In addition, an Akt1 small interfering RNA–embedded stent alleviated restenosis, reducing cell growth via muting RNA [125,126]. Furthermore, bare-metal stents with a synthetic complex for reversible vector binding produced prominent green fluorescent protein positivity in A10 cells proximal to the strut after 72 hours in culture [127].

A collagen-coated stent covalently coupled with anti-DNA immunoglobulin M antibody and loaded with plasmid DNA was efficiently developed for localized gene delivery to smooth

muscle cells in an artery, accomplishing high-level protein production through reporter gene expression [125]. In addition, a stent coated with biomimetic hyaluronic acid and deposited with DNA/polyethylenimine polyplexes was explored to deliver plasmid DNA to the artery, exerting its efficacy in alleviating restenosis with a higher neointimal transfection rate while maintaining structural stability [128].

Stents Equipped With Cardiovascular Self-Reporting Sensors

Continuous blood flow surveillance can serve as screening, advanced detection, and alert for cardiovascular health using noninvasive technology that can be placed in the coronary arteries [129]. Remote monitoring of patient progress is feasible by creating an application-specific integrated circuit that features a voltage regulator and radio frequency power element loaded in biomedical devices, including cardiovascular stents.

For instance, a remote monitoring stent was combined with a tiny heart pressure sensor as well as a wireless transmitter that continuously monitors vascular conditions and the status of implanted devices. To minimize the number of antenna components for the conservation of space, the stent was used as an inductive antenna to create a wireless network [130,131], transmitting quantified solubilization to the immediate neighborhood via a wireless telemetry transmitter [132]. Reviewing the admittance of an antenna close to the implant component and connected to it via electromagnetic coupling will enable this function [133]. A radio frequency–powering component was implanted on the chip in the finished device as an ideal power distribution feature. Microelectromechanical modules were crammed with an application-specific integrated circuit for data collection [134].

As shown in Figure 3, a blood flow sensor enclosed in graphene-embedded silicon rings subsequently equipped with a digital wireless transmission microchip was developed as a unit of the smart theranostic cardiovascular stent (Figure 3C). Numerous commercial devices, including pressure sensors, use the piezoresistive effect of silicon, whose gauge factors can be 2 orders of magnitude larger than those observed in most metals [135,136]. Thus, a flow sensor enclosed in the stent was able to continuously monitor real-time blood flow with high inductance and pressure resolution and transmit corresponding data to a cardiologist outside the body. In addition to superior moisture barrier property, the high thermal conductivity of graphene (which has a negative thermal expansion coefficient [-8.0×10^{-6}/K] between 0 and 700 K) guaranteed dimensional stability upon exposure to body temperature and continuous blood flow.

The pressure sensors and the microchip were mounted on the rectangular areas of the stent structure, as shown in Figure 3C. The pressure sensors bound to the steel stent [137,138] were molded into graphene-embedded silicone rings, and the pattern was cut on a thin stainless-steel foil. These digital transmission techniques reduced the power radiated by the external reader, thus minimizing the patient's exposure to electromagnetic fields.

In electromagnetic coupling, a continuous electromagnetic wave with relatively large power is radiated by the reader, and the microchip modulates the impedance of the antenna by connecting or disconnecting a load to it according to the data to be transmitted [130].

Figure 3. (1) stent and rings, (2) dimension and size of rings (A: Ring inner diameter (i.e., same as stent outer diameter); B: Stent inner diameter), (3) 3-Dimentional Stent (C: Stent length; D: Ring outer diameter) and (4) application of external electromagnetic stimuli.

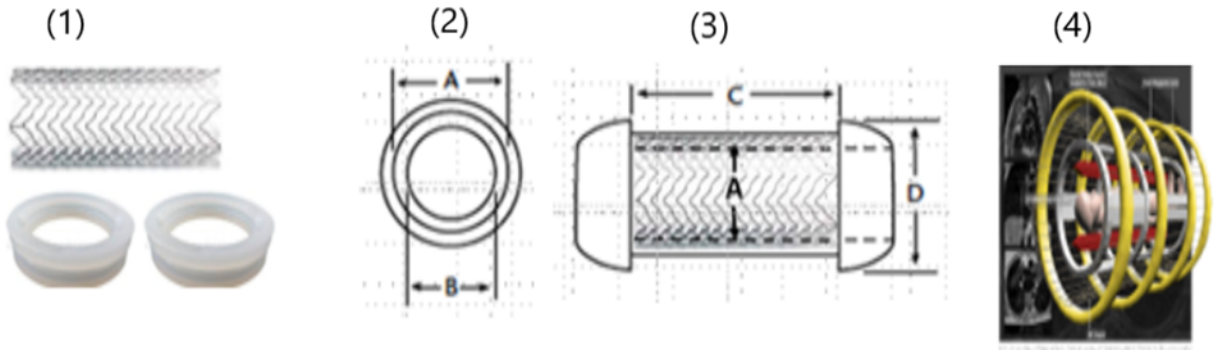

Conclusion

Biotechnologies play an important role in cardiovascular repair and regeneration. Genetic variables in CVD, currently available technology, and biomaterials for organ-independent cardiovascular repair systems were updated in this article in a timely manner. Advanced biotechnologies aimed at target-specific therapeutics are designed for customized and personalized cardiac treatment strategies with one or multiple administration routes whose methods should be further improved to enhance targeting and treatment efficacy.

The goal of gene therapy for cardiac repair and regeneration is to achieve cardiac transfection outcomes via the selection of proper gene vectors and modifying a gene or genetic pathways. Moreover, 3D bioprinting technology has been widely used in cardiac repair by integrating biomaterials with various manufacturing processes to customize cardiac conditions. 3D scaffolds with varying cell types have demonstrated better biocompatibility, delivery efficiency, and low immunogenicity. In the future, screening and designing of viral vectors through structure evolution mediated by 3D printing would enhance cardiac gene therapy.

To overcome the current obstacles in cardiac repair and regeneration and achieve successful therapeutic applications, future interdisciplinary collaborative work should be integral. Advanced new material and cell biology, along with AI-based telehealth, will be essential to create efficient implantable biomedical devices, including cardiovascular stents. Advanced innovative bioengineering, gene delivery, and cell biology technologies will continuously revolutionize medical devices for cardiovascular repair and regeneration in the future.

Acknowledgments

This study was supported by a Funding for Excellence award from the Office of Research Development, University of Missouri-Kansas City.

Conflicts of Interest

None declared.

References

1. Martin S, Aday A, Almarzooq Z, Anderson C, Arora P, Avery C, American Heart Association Council on EpidemiologyPrevention Statistics CommitteeStroke Statistics Subcommittee. 2024 heart disease and stroke statistics: a report of US and global data from the American Heart Association. Circulation 2024 Feb 20;149(8):e347-e913 [FREE Full text] [doi: 10.1161/CIR.0000000000001209] [Medline: 38264914]
2. Braunwald E. Cell-based therapy in cardiac regeneration. Circulation Research 2018 Jul 06;123(2):132-137. [doi: 10.1161/circresaha.118.313484]
3. Zhu Z, Ng DWH, Park HS, McAlpine MC. 3D-printed multifunctional materials enabled by artificial-intelligence-assisted fabrication technologies. Nat Rev Mater 2020 Oct 12;6(1):27-47. [doi: 10.1038/s41578-020-00235-2]
4. Tsao C, Aday A, Almarzooq Z, Alonso A, Beaton A, Bittencourt M, et al. Heart disease and stroke statistics-2022 update: a report from the American Heart Association. Circulation 2022 Feb 22;145(8):e153-e639 [FREE Full text] [doi: 10.1161/CIR.0000000000001052] [Medline: 35078371]
5. Kolwicz SC, Purohit S, Tian R. Cardiac metabolism and its interactions with contraction, growth, and survival of cardiomyocytes. Circulation Research 2013 Aug 16;113(5):603-616. [doi: 10.1161/circresaha.113.302095]
6. O'Neal WT, Griffin WF, Kent SD, Virag JAI. Cellular pathways of death and survival in acute myocardial infarction. J Clin Exp Cardiolog 2012;S6(003):1-9. [doi: 10.4172/2155-9880.S6-003]
7. Broughton KM, Wang BJ, Firouzi F, Khalafalla F, Dimmeler S, Fernandez-Aviles F, et al. Mechanisms of cardiac repair and regeneration. Circ Res 2018 Apr 13;122(8):1151-1163. [doi: 10.1161/circresaha.117.312586]
8. Anzai T, Yoshikawa T, Shiraki H, Asakura Y, Akaishi M, Mitamura H, et al. C-reactive protein as a predictor of infarct expansion and cardiac rupture after a first Q-wave acute myocardial infarction. Circulation 1997 Aug 05;96(3):778-784. [doi: 10.1161/01.cir.96.3.778] [Medline: 9264482]
9. Chingale M, Zhu D, Cheng K, Huang K. Bioengineering technologies for cardiac regenerative medicine. Front Bioeng Biotechnol 2021 Jun 3;9:681705 [FREE Full text] [doi: 10.3389/fbioe.2021.681705] [Medline: 34150737]
10. Bolli R. Oxygen-derived free radicals and postischemic myocardial dysfunction ("stunned myocardium"). J Am Coll Cardiol 1988 Jul;12(1):239-249 [FREE Full text] [doi: 10.1016/0735-1097(88)90381-6] [Medline: 3288676]
11. Hori M, Nishida K. Oxidative stress and left ventricular remodelling after myocardial infarction. Cardiovasc Res 2009 Feb 15;81(3):457-464. [doi: 10.1093/cvr/cvn335] [Medline: 19047340]
12. Sies H. Hydrogen peroxide as a central redox signaling molecule in physiological oxidative stress: Oxidative eustress. Redox Biol 2017 Apr;11:613-619 [FREE Full text] [doi: 10.1016/j.redox.2016.12.035] [Medline: 28110218]
13. Weng X, Tan H, Huang Z, Chen J, Zhang N, Wang Q, et al. Targeted delivery and ROS-responsive release of Resolvin D1 by platelet chimeric liposome ameliorates myocardial ischemia-reperfusion injury. J Nanobiotechnology 2022 Oct 20;20(1):454 [FREE Full text] [doi: 10.1186/s12951-022-01652-x] [Medline: 36266658]
14. Forman HJ, Bernardo A, Davies KJ. What is the concentration of hydrogen peroxide in blood and plasma? Arch Biochem Biophys 2016 Aug 01;603:48-53. [doi: 10.1016/j.abb.2016.05.005] [Medline: 27173735]
15. Heusch G, Gersh BJ. The pathophysiology of acute myocardial infarction and strategies of protection beyond reperfusion: a continual challenge. Eur Heart J 2017 Mar 14;38(11):774-784. [doi: 10.1093/eurheartj/ehw224] [Medline: 27354052]
16. D'Amore A, Yoshizumi T, Luketich SK, Wolf MT, Gu X, Cammarata M, et al. Bi-layered polyurethane - extracellular matrix cardiac patch improves ischemic ventricular wall remodeling in a rat model. Biomaterials 2016 Nov;107:1-14. [doi: 10.1016/j.biomaterials.2016.07.039] [Medline: 27579776]
17. Sebastião MJ, Gomes-Alves P, Reis I, Sanchez B, Palacios I, Serra M, et al. Bioreactor-based 3D human myocardial ischemia/reperfusion in vitro model: a novel tool to unveil key paracrine factors upon acute myocardial infarction. Transl Res 2020 Jan;215:57-74 [FREE Full text] [doi: 10.1016/j.trsl.2019.09.001] [Medline: 31541616]
18. Kim M, Choe Y, Kim G. Injectable hierarchical micro/nanofibrous collagen-based scaffolds. Chemical Engineering Journal 2019 Jun;365:220-230. [doi: 10.1016/j.cej.2019.02.044]

19. Hou S, Niu X, Li L, Zhou J, Qian Z, Yao D, et al. Simultaneous nano- and microscale structural control of injectable hydrogels via the assembly of nanofibrous protein microparticles for tissue regeneration. Biomaterials 2019 Dec;223:119458. [doi: 10.1016/j.biomaterials.2019.119458] [Medline: 31491598]
20. Bian T, Zhao K, Meng Q, Tang Y, Jiao H, Luo J. The construction and performance of multi-level hierarchical hydroxyapatite (HA)/collagen composite implant based on biomimetic bone Haversian motif. Materials Design 2019 Jan;162:60-69. [doi: 10.1016/j.matdes.2018.11.040]
21. Veerubhotla K, Lee CH. Design of biodegradable 3D-printed cardiovascular stent. Bioprinting 2022 Jun;26:e00204. [doi: 10.1016/j.bprint.2022.e00204]
22. Ravindran S. Materials for Advanced Packaging (Lu, D. and Wong, C.P.) [Book reviews]. IEEE Nanotechnology Mag 2009 Sep;3(3):27-28. [doi: 10.1109/mnano.2009.934216]
23. Veerubhotla K, McGraw H, Lee CH. Assessment of biocompatibility of 3D‐printed cardiovascular stent. Adv Ther 2023 Mar 15;6(5):1. [doi: 10.1002/adtp.202200292]
24. Sugarman B, Young EJ. Infections associated with prosthetic devices: magnitude of the problem. Infect Dis Clin North Am 1989 Jun;3(2):187-198 [FREE Full text] [doi: 10.1016/S0891-5520(20)30257-9]
25. Hamon M, Champ-Rigot L, Morello R, Riddell JW, Hamon M. Diagnostic accuracy of in-stent coronary restenosis detection with multislice spiral computed tomography: a meta-analysis. Eur Radiol 2008 Feb 1;18(2):217-225. [doi: 10.1007/s00330-007-0743-6] [Medline: 17763854]
26. Dai T, Wang J, Hu P. Diagnostic performance of computed tomography angiography in the detection of coronary artery in-stent restenosis: evidence from an updated meta-analysis. Eur Radiol 2018 Apr 9;28(4):1373-1382. [doi: 10.1007/s00330-017-5097-0] [Medline: 29124384]
27. Zimmerman SL, Kral BG, Fishman EK. Diagnostic Quality of Dual-Source Coronary CT Examinations Performed Without Heart Rate Control. J Computer Assisted Tomogr 2014;38(6):949-955. [doi: 10.1097/rct.0000000000000135]
28. Flohr TG, McCollough CH, Bruder H, Petersilka M, Gruber K, Süss C, et al. First performance evaluation of a dual-source CT (DSCT) system. Eur Radiol 2006 Feb 10;16(2):256-268. [doi: 10.1007/s00330-005-2919-2] [Medline: 16341833]
29. Liu W, Li G, Liu H, Lei J. Diagnostic accuracy of dual-source computed tomography angiography for the detection of coronary in-stent restenosis: A systematic review and meta-analysis. Echocardiography 2018 Apr 23;35(4):541-550. [doi: 10.1111/echo.13863] [Medline: 29569751]
30. Carrabba N, Schuijf JD, de Graaf FR, Parodi G, Maffei E, Valenti R, et al. Diagnostic accuracy of 64-slice computed tomography coronary angiography for the detection of in-stent restenosis: a meta-analysis. J Nucl Cardiol 2010 Jun;17(3):470-478 [FREE Full text] [doi: 10.1007/s12350-010-9218-2] [Medline: 20379863]
31. Byrne RA, Serruys PW, Baumbach A, Escaned J, Fajadet J, James S, et al. Report of a European Society of Cardiology-European Association of Percutaneous Cardiovascular Interventions task force on the evaluation of coronary stents in Europe: executive summary. Eur Heart J 2015 Oct 07;36(38):2608-2620 [FREE Full text] [doi: 10.1093/eurheartj/ehv203] [Medline: 26071600]
32. Tang X. The role of artificial intelligence in medical imaging research. BJR Open 2020 Nov;2(1):20190031 [FREE Full text] [doi: 10.1259/bjro.20190031] [Medline: 33178962]
33. Valente J, António J, Mora C, Jardim S. Developments in image processing using deep learning and reinforcement learning. J Imaging 2023 Sep 30;9(10):207 [FREE Full text] [doi: 10.3390/jimaging9100207] [Medline: 37888314]
34. Kolber MR, Scrimshaw C. Family history of cardiovascular disease. Can Fam Physician 2014 Nov;60(11):1016 [FREE Full text] [Medline: 25392442]
35. Tahir UA, Gerszten RE. Molecular biomarkers for cardiometabolic disease: risk assessment in young individuals. Circulation Research 2023 Jun 09;132(12):1663-1673. [doi: 10.1161/circresaha.123.322000]
36. Inherited Cardiac Conditions (Genetic Disorders). University of Ottawa Heart Institute. URL: https://www.ottawaheart.ca/heart-condition/inherited-cardiac-conditions-genetic-disorders [accessed 2025-02-21]
37. Lloyd-Jones DM, Nam B, D'Agostino RB, Levy D, Murabito JM, Wang TJ, et al. Parental cardiovascular disease as a risk factor for cardiovascular disease in middle-aged adults: a prospective study of parents and offspring. JAMA 2004 May 12;291(18):2204-2211. [doi: 10.1001/jama.291.18.2204] [Medline: 15138242]
38. Grundy SM, Stone NJ, Bailey AL, Beam C, Birtcher KK, Blumenthal RS, et al. 2018 AHA/ACC/AACVPR/AAPA/ABC/ACPM/ADA/AGS/APhA/ASPC/NLA/PCNA Guideline on the Management of Blood Cholesterol: a report of the American College of Cardiology/American Heart Association Task Force on Clinical Practice Guidelines. Circulation 2019 Jun 18;139(25):e1082-e1143 [FREE Full text] [doi: 10.1161/CIR.0000000000000625] [Medline: 30586774]
39. Márquez-Luna C, Loh P, South Asian Type 2 Diabetes (SAT2D) Consortium, SIGMA Type 2 Diabetes Consortium, Price AL. Multiethnic polygenic risk scores improve risk prediction in diverse populations. Genet Epidemiol 2017 Dec 07;41(8):811-823 [FREE Full text] [doi: 10.1002/gepi.22083] [Medline: 29110330]
40. Widen E, Raben TG, Lello L, Hsu SDH. Machine learning prediction of biomarkers from SNPs and of disease risk from biomarkers in the UK Biobank. Genes (Basel) 2021 Jun 29;12(7):991 [FREE Full text] [doi: 10.3390/genes12070991] [Medline: 34209487]

41. Collister JA, Liu X, Clifton L. Calculating polygenic risk scores (PRS) in UK Biobank: a practical guide for epidemiologists. Front Genet 2022 Feb 18;13:818574 [FREE Full text] [doi: 10.3389/fgene.2022.818574] [Medline: 35251129]
42. Inouye M, Abraham G, Nelson CP, Wood AM, Sweeting MJ, Dudbridge F, UK Biobank CardioMetabolic Consortium CHD Working Group. Genomic risk prediction of coronary artery disease in 480,000 adults: implications for primary prevention. J Am Coll Cardiol 2018 Oct 16;72(16):1883-1893 [FREE Full text] [doi: 10.1016/j.jacc.2018.07.079] [Medline: 30309464]
43. Aung N, Vargas JD, Yang C, Cabrera CP, Warren HR, Fung K, et al. Genome-wide analysis of left ventricular image-derived phenotypes identifies fourteen loci associated with cardiac morphogenesis and heart failure development. Circulation 2019 Oct 15;140(16):1318-1330. [doi: 10.1161/circulationaha.119.041161]
44. Axelrud LK, Santoro ML, Pine DS, Talarico F, Gadelha A, Manfro GG, et al. Polygenic risk score for Alzheimer's disease: implications for memory performance and hippocampal volumes in early life. Am J Psychiatry 2018 Jun 01;175(6):555-563 [FREE Full text] [doi: 10.1176/appi.ajp.2017.17050529] [Medline: 29495896]
45. Gola D, Erdmann J, Müller-Myhsok B, Schunkert H, König IR. Polygenic risk scores outperform machine learning methods in predicting coronary artery disease status. Genet Epidemiol 2020 Mar 10;44(2):125-138. [doi: 10.1002/gepi.22279] [Medline: 31922285]
46. Hajar R. Genetics in cardiovascular disease. Heart Views 2020;21(1):55. [doi: 10.4103/heartviews.heartviews_140_19]
47. Martin AR, Kanai M, Kamatani Y, Okada Y, Neale BM, Daly MJ. Clinical use of current polygenic risk scores may exacerbate health disparities. Nat Genet 2019 Apr 29;51(4):584-591 [FREE Full text] [doi: 10.1038/s41588-019-0379-x] [Medline: 30926966]
48. Efovi D, Xiao Q. Noncoding RNAs in vascular cell biology and restenosis. Biology (Basel) 2022 Dec 22;12(1):24 [FREE Full text] [doi: 10.3390/biology12010024] [Medline: 36671717]
49. Padua L, Cuccagna C, Pazzaglia C. Novel sensory paradigms for neuromodulation in disorders of consciousness in traumatic brain injury. Curr Opin Neurol 2019 Dec;32(6):844-849. [doi: 10.1097/WCO.0000000000000747] [Medline: 31567499]
50. Ference B, Ginsberg H, Graham I, Ray K, Packard C, Bruckert E, et al. Low-density lipoproteins cause atherosclerotic cardiovascular disease. 1. Evidence from genetic, epidemiologic, and clinical studies. A consensus statement from the European Atherosclerosis Society Consensus Panel. Eur Heart J 2017 Aug 21;38(32):2459-2472 [FREE Full text] [doi: 10.1093/eurheartj/ehx144] [Medline: 28444290]
51. Sato K, Kaikita K, Nakayama N, Horio E, Yoshimura H, Ono T, et al. Coronary vasomotor response to intracoronary acetylcholine injection, clinical features, and long‐term prognosis in 873 consecutive patients with coronary spasm: analysis of a single‐center study over 20 years. JAHA 2013 Aug 22;2(4):1. [doi: 10.1161/jaha.113.000227]
52. Eshlaghi SN, Syedmoradi L, Amini A, Omidfar K, Omidfar K. A label-free electrochemical aptasensor based on screen printed carbon electrodes with gold nanoparticles-polypyrrole composite for detection of cardiac troponin I. IEEE Sensors J 2023 Feb 15;23(4):3439-3445. [doi: 10.1109/jsen.2023.3235740]
53. Montone R, Niccoli G, Fracassi F, Russo M, Gurgoglione F, Cammà G, et al. Patients with acute myocardial infarction and non-obstructive coronary arteries: safety and prognostic relevance of invasive coronary provocative tests. Eur Heart J 2018 Jan 07;39(2):91-98. [doi: 10.1093/eurheartj/ehx667] [Medline: 29228159]
54. Musunuru K, Hershberger RE, Day SM, Klinedinst NJ, Landstrom AP, Parikh VN, et al. Genetic testing for inherited cardiovascular diseases: a scientific statement from the American Heart Association. Circ: Genomic and Precision Medicine 2020 Aug;13(4):1. [doi: 10.1161/hcg.0000000000000067]
55. Wiegman A, de Groot E, Hutten BA, Rodenburg J, Gort J, Bakker HD, et al. Arterial intima-media thickness in children heterozygous for familial hypercholesterolaemia. The Lancet 2004 Jan;363(9406):369-370. [doi: 10.1016/s0140-6736(04)15467-6]
56. Kusters DM, Wiegman A, Kastelein JJ, Hutten BA. Carotid intima-media thickness in children with familial hypercholesterolemia. Circulation Research 2014 Jan 17;114(2):307-310. [doi: 10.1161/circresaha.114.301430]
57. Vlahos AP, Naka KK, Bechlioulis A, Theoharis P, Vakalis K, Moutzouri E, et al. Endothelial dysfunction, but not structural atherosclerosis, is evident early in children with heterozygous familial hypercholesterolemia. Pediatr Cardiol 2014 Jan 3;35(1):63-70. [doi: 10.1007/s00246-013-0742-0] [Medline: 23821294]
58. de Jongh S, Lilien MR, Bakker HD, Hutten BA, Kastelein JJ, Stroes ES. Family history of cardiovascular events and endothelial dysfunction in children with familial hypercholesterolemia. Atherosclerosis 2002 Jul;163(1):193-197. [doi: 10.1016/s0021-9150(02)00003-5] [Medline: 12048139]
59. Lozano P, Henrikson NB, Dunn J, Morrison CC, Nguyen M, Blasi PR, et al. Lipid screening in childhood and adolescence for detection of familial hypercholesterolemia: evidence report and systematic review for the US Preventive Services Task Force. JAMA 2016 Aug 09;316(6):645-655. [doi: 10.1001/jama.2016.6176] [Medline: 27532919]
60. Schrodi SJ, Mukherjee S, Shan Y, Tromp G, Sninsky JJ, Callear AP, et al. Genetic-based prediction of disease traits: prediction is very difficult, especially about the future. Front Genet 2014 Jun 02;5:162 [FREE Full text] [doi: 10.3389/fgene.2014.00162] [Medline: 24917882]
61. Ajufo EC, Aragam KG. Improving polygenic risk scores for coronary artery disease: what helps and by how much? JACC Basic Transl Sci 2023 Dec;8(12):1500-1502 [FREE Full text] [doi: 10.1016/j.jacbts.2023.10.005] [Medline: 38205353]

62. Sharif F, Daly K, Crowley J, O'Brien T. Current status of catheter- and stent-based gene therapy. Cardiovasc Res 2004 Nov 01;64(2):208-216. [doi: 10.1016/j.cardiores.2004.07.003] [Medline: 15485679]
63. Vaishya R, Javaid M, Khan IH, Haleem A. Artificial intelligence (AI) applications for COVID-19 pandemic. Diabetes Metab Syndr 2020 Jul;14(4):337-339 [FREE Full text] [doi: 10.1016/j.dsx.2020.04.012] [Medline: 32305024]
64. van der Schaar M, Alaa AM, Floto A, Gimson A, Scholtes S, Wood A, et al. How artificial intelligence and machine learning can help healthcare systems respond to COVID-19. Mach Learn 2021 Dec 09;110(1):1-14 [FREE Full text] [doi: 10.1007/s10994-020-05928-x] [Medline: 33318723]
65. Krittanawong C, Johnson KW, Choi E, Kaplin S, Venner E, Murugan M, et al. Artificial intelligence and cardiovascular genetics. Life (Basel) 2022 Feb 14;12(2):279 [FREE Full text] [doi: 10.3390/life12020279] [Medline: 35207566]
66. Zreik M, van Hamersvelt RW, Wolterink JM, Leiner T, Viergever MA, Isgum I. A recurrent CNN for automatic detection and classification of coronary artery plaque and stenosis in coronary CT angiography. IEEE Trans. Med. Imaging 2019 Jul;38(7):1588-1598. [doi: 10.1109/tmi.2018.2883807]
67. Shelke S, Veerubhotla K, Lee Y, Lee CH. Telehealth of cardiac devices for CVD treatment. Biotechnol Bioeng 2024 Mar 27;121(3):823-834. [doi: 10.1002/bit.28637] [Medline: 38151894]
68. James S, Rao SV, Granger CB. Registry-based randomized clinical trials--a new clinical trial paradigm. Nat Rev Cardiol 2015 May 17;12(5):312-316. [doi: 10.1038/nrcardio.2015.33] [Medline: 25781411]
69. Lauschensky A, Hayn D, Eggerth A, Modre-Osprian R, Pfeifer B, Egelseer-Bründl T, et al. Concept for visualisation of guideline adherence of medication prescriptions in a heart failure telehealth system. Stud Health Technol Inform 2020 Jun 23;271:49-56. [doi: 10.3233/SHTI200073] [Medline: 32578540]
70. Bradbury A, Patrick-Miller L, Harris D, Stevens E, Egleston B, Smith K, et al. Utilizing remote real-time videoconferencing to expand access to cancer genetic services in community practices: a multicenter feasibility study. J Med Internet Res 2016 Feb 01;18(2):e23 [FREE Full text] [doi: 10.2196/jmir.4564] [Medline: 26831751]
71. Boothe E, Greenberg S, Delaney CL, Cohen SA. Genetic counseling service delivery models: a study of genetic counselors' interests, needs, and barriers to implementation. J Genet Couns 2021 Feb 03;30(1):283-292. [doi: 10.1002/jgc4.1319] [Medline: 32885542]
72. Peshkin BN, Kelly S, Nusbaum RH, Similuk M, DeMarco TA, Hooker GW, et al. Patient perceptions of telephone vs. in-person BRCA1/BRCA2 genetic counseling. J Genet Couns 2016 Jun 12;25(3):472-482 [FREE Full text] [doi: 10.1007/s10897-015-9897-6] [Medline: 26455498]
73. Athens BA, Caldwell SL, Umstead KL, Connors PD, Brenna E, Biesecker BB. A systematic review of randomized controlled trials to assess outcomes of genetic counseling. J Genet Couns 2017 Oct 02;26(5):902-933 [FREE Full text] [doi: 10.1007/s10897-017-0082-y] [Medline: 28255928]
74. Gorrie A, Gold J, Cameron C, Krause M, Kincaid H. Benefits and limitations of telegenetics: a literature review. J Genet Couns 2021 Aug 04;30(4):924-937. [doi: 10.1002/jgc4.1418] [Medline: 33817891]
75. Hilgart JS, Hayward JA, Coles B, Iredale R. Telegenetics: a systematic review of telemedicine in genetics services. Genet Med 2012 Sep;14(9):765-776 [FREE Full text] [doi: 10.1038/gim.2012.40] [Medline: 22498847]
76. Cohen AJ, Shur N, Starin D, MacLeod E, Roshan Lal T, Leon E, et al. Pediatric medical genetics house call: telemedicine for the next generation of patients and providers. Am J Med Genet C Semin Med Genet 2021 Mar 11;187(1):55-63. [doi: 10.1002/ajmg.c.31882] [Medline: 33427371]
77. Mills R, MacFarlane IM, Caleshu C, Ringler MA, Zierhut HA. Genetic counselor experiences with telehealth before and after COVID-19. J Genet Couns 2021 Aug 07;30(4):999-1009 [FREE Full text] [doi: 10.1002/jgc4.1465] [Medline: 34231953]
78. Vandenberk B, Raj SR. Remote patient monitoring: what have we learned and where are we going? Curr Cardiovasc Risk Rep 2023 Apr 22;17(6):103-115 [FREE Full text] [doi: 10.1007/s12170-023-00720-7] [Medline: 37305214]
79. Tayal M, Mukherjee A, Chauhan U, Uniyal M, Garg S, Singh A, et al. Evaluation of remote monitoring device for monitoring vital parameters against reference standard: a diagnostic validation study for COVID-19 preparedness. Indian J Community Med 2020;45(2):235. [doi: 10.4103/ijcm.ijcm_317_20]
80. Ding X, Clifton D, Ji N, Lovell NH, Bonato P, Chen W, et al. Wearable sensing and telehealth technology with potential applications in the coronavirus pandemic. IEEE Rev. Biomed. Eng 2021;14:48-70. [doi: 10.1109/rbme.2020.2992838]
81. Watson AR, Wah R, Thamman R. The value of remote monitoring for the COVID-19 pandemic. Telemed J E Health 2020 Sep 01;26(9):1110-1112. [doi: 10.1089/tmj.2020.0134] [Medline: 32384251]
82. Mishra N, Duke J, Lenert L, Karki S. Public health reporting and outbreak response: synergies with evolving clinical standards for interoperability. J Am Med Inform Assoc 2020 Jul 01;27(7):1136-1138 [FREE Full text] [doi: 10.1093/jamia/ocaa059] [Medline: 32692844]
83. Henkel AG, Spinner C. IT-STRATEGIE: Digitalumbau bei laufendem Betrieb. kma 2020 Apr 15;25(04):51-54. [doi: 10.1055/s-0040-1709870]
84. Munos B, Baker P, Bot B, Crouthamel M, de Vries G, Ferguson I, et al. Mobile health: the power of wearables, sensors, and apps to transform clinical trials. Ann N Y Acad Sci 2016 Jul;1375(1):3-18. [doi: 10.1111/nyas.13117] [Medline: 27384501]

85. Song X, Wang X, Zhang J, Shen S, Yin W, Ye G, et al. A tunable self-healing ionic hydrogel with microscopic homogeneous conductivity as a cardiac patch for myocardial infarction repair. Biomaterials 2021 Jun;273:120811. [doi: 10.1016/j.biomaterials.2021.120811] [Medline: 33882404]
86. Pecha S, Eschenhagen T, Reichenspurner H. Myocardial tissue engineering for cardiac repair. J Heart Lung Transplant 2016 Mar;35(3):294-298. [doi: 10.1016/j.healun.2015.12.007] [Medline: 26856673]
87. Lee M, Kim MC, Lee JY. Nanomaterial-based electrically conductive hydrogels for cardiac tissue repair. IJN 2022 Dec;Volume 17:6181-6200. [doi: 10.2147/ijn.s386763]
88. Lin X, Liu Y, Bai A, Cai H, Bai Y, Jiang W, et al. A viscoelastic adhesive epicardial patch for treating myocardial infarction. Nat Biomed Eng 2019 Aug 15;3(8):632-643. [doi: 10.1038/s41551-019-0380-9] [Medline: 30988471]
89. Wu T, Liu W. Functional hydrogels for the treatment of myocardial infarction. NPG Asia Mater 2022 Feb 18;14(1):1. [doi: 10.1038/s41427-021-00330-y]
90. Toyoda Y, Guy TS, Kashem A. Present status and future perspectives of heart transplantation. Circ J 2013;77(5):1097-1110 [FREE Full text] [doi: 10.1253/circj.cj-13-0296] [Medline: 23614963]
91. Zhang Y, Zhu D, Wei Y, Wu Y, Cui W, Liuqin L, et al. A collagen hydrogel loaded with HDAC7-derived peptide promotes the regeneration of infarcted myocardium with functional improvement in a rodent model. Acta Biomater 2019 Mar 01;86:223-234. [doi: 10.1016/j.actbio.2019.01.022] [Medline: 30660010]
92. Wu T, Cui C, Huang Y, Liu Y, Fan C, Han X, et al. Coadministration of an adhesive conductive hydrogel patch and an injectable hydrogel to treat myocardial infarction. ACS Appl Mater Interfaces 2020 Jan 15;12(2):2039-2048. [doi: 10.1021/acsami.9b17907] [Medline: 31859471]
93. Nguyen-Truong M, Li Y, Wang Z. Mechanical considerations of electrospun scaffolds for myocardial tissue and regenerative engineering. Bioengineering (Basel) 2020 Oct 03;7(4):122 [FREE Full text] [doi: 10.3390/bioengineering7040122] [Medline: 33022929]
94. Li Z, Yi N, Chen R, Meng Y, Wang Y, Liu H, et al. miR-29b-3p protects cardiomyocytes against endotoxin-induced apoptosis and inflammatory response through targeting FOXO3A. Cell Signal 2020 Oct;74:109716 [FREE Full text] [doi: 10.1016/j.cellsig.2020.109716] [Medline: 32707074]
95. Hodgkinson CP, Bareja A, Gomez JA, Dzau VJ. Emerging concepts in paracrine mechanisms in regenerative cardiovascular medicine and biology. Circulation Research 2016 Jan 08;118(1):95-107. [doi: 10.1161/circresaha.115.305373]
96. Williams DF. On the mechanisms of biocompatibility. Biomaterials 2008 Jul;29(20):2941-2953. [doi: 10.1016/j.biomaterials.2008.04.023] [Medline: 18440630]
97. Chan BP, Leong KW. Scaffolding in tissue engineering: general approaches and tissue-specific considerations. Eur Spine J 2008 Dec 13;17 Suppl 4(Suppl 4):467-479 [FREE Full text] [doi: 10.1007/s00586-008-0745-3] [Medline: 19005702]
98. Shapira A, Feiner R, Dvir T. Composite biomaterial scaffolds for cardiac tissue engineering. International Materials Reviews 2024 Jul 29;61(1):1-19. [doi: 10.1179/1743280415y.0000000012]
99. Cocarta A, Hobzova R, Trchova M, Svojgr K, Kodetova M, Pochop P, et al. 2 - hydroxyethyl methacrylate hydrogels for local drug delivery: study of topotecan and vincristine sorption/desorption kinetics and polymer-drug interaction by ATR - FTIR spectroscopy. Macro Chemistry & Physics 2021 May 04;222(13):1. [doi: 10.1002/macp.202100086]
100. Ghamkhari A, Abbaspour-Ravasjani S, Talebi M, Hamishehkar H, Hamblin MR. Development of a graphene oxide-poly lactide nanocomposite as a Smart Drug Delivery System. Int J Biol Macromol 2021 Feb 01;169:521-531. [doi: 10.1016/j.ijbiomac.2020.12.084] [Medline: 33340628]
101. Kazemi Ashtiani M, Zandi M, Shokrollahi P, Ehsani M, Baharvand H. Surface modification of poly(2 - hydroxyethyl methacrylate) hydrogel for contact lens application. Polymers for Advanced Techs 2018 Jan 12;29(4):1227-1233. [doi: 10.1002/pat.4233]
102. Rossos A, Banti C, Kalampounias A, Papachristodoulou C, Kordatos K, Zoumpoulakis P, et al. pHEMA@AGMNA-1: a novel material for the development of antibacterial contact lens. Mater Sci Eng C Mater Biol Appl 2020 Jun;111:110770. [doi: 10.1016/j.msec.2020.110770] [Medline: 32279741]
103. Macková H, Plichta Z, Hlídková H, Sedláček O, Konefal R, Sadakbayeva Z, et al. Reductively degradable poly(2-hydroxyethyl methacrylate) hydrogels with oriented porosity for tissue engineering applications. ACS Appl Mater Interfaces 2017 Mar 29;9(12):10544-10553. [doi: 10.1021/acsami.7b01513] [Medline: 28287694]
104. Passos MF, Carvalho NMS, Rodrigues AA, Bavaresco VP, Jardini AL, Maciel MRW, et al. PHEMA hydrogels obtained by infrared radiation for cartilage tissue engineering. International Journal of Chemical Engineering 2019 Jan 31;2019:1-9. [doi: 10.1155/2019/4249581]
105. Kalinke C, Muñoz RAA. 3D-printed microdevices: from design to applications. Micromachines (Basel) 2024 Jun 15;15(6):791 [FREE Full text] [doi: 10.3390/mi15060791] [Medline: 38930761]
106. Li M, Wu H, Yuan Y, Hu B, Gu N. Recent fabrications and applications of cardiac patch in myocardial infarction treatment. VIEW 2021 Sep 16;3(2):1. [doi: 10.1002/viw.20200153]
107. Mei X, Cheng K. Recent development in therapeutic cardiac patches. Front Cardiovasc Med 2020 Nov 27;7:610364 [FREE Full text] [doi: 10.3389/fcvm.2020.610364] [Medline: 33330673]

108. Rinaldi A, Caraffi R, Grazioli MV, Oddone N, Giardino L, Tosi G, et al. Applications of the ROS-responsive thioketal linker for the production of smart nanomedicines. Polymers (Basel) 2022 Feb 11;14(4):687 [FREE Full text] [doi: 10.3390/polym14040687] [Medline: 35215600]
109. Wu S, Yang C, Hsu W, Lin L. 3D-printed microelectronics for integrated circuitry and passive wireless sensors. Microsyst Nanoeng 2015 Jul 20;1(1):1. [doi: 10.1038/micronano.2015.13]
110. Joe Lopes A, MacDonald E, Wicker R. Integrating stereolithography and direct print technologies for 3D structural electronics fabrication. Rapid Prototyping Journal 2012;18(2):43 [FREE Full text] [doi: 10.1108/13552541211212113]
111. Guo S, Qiu K, Meng F, Park SH, McAlpine MC. 3D printed stretchable tactile sensors. Adv Mater 2017 Jul 05;29(27):1 [FREE Full text] [doi: 10.1002/adma.201701218] [Medline: 28474793]
112. Roda A, Guardigli M, Calabria D, Calabretta MM, Cevenini L, Michelini E. A 3D-printed device for a smartphone-based chemiluminescence biosensor for lactate in oral fluid and sweat. Analyst 2014 Dec 21;139(24):6494-6501. [doi: 10.1039/c4an01612b] [Medline: 25343380]
113. Sun P. How AI Helps Physicians Improve Telehealth Patient Care in Real-Time. Arizona Telemedicine Program. 2022 Jun 23. URL: https://telemedicine.arizona.edu/blog/how-ai-helps-physicians-improve-telehealth-patient-care-real-time [accessed 2025-02-21]
114. Lafont A, Guzman LA, Whitlow PL, Goormastic M, Cornhill JF, Chisolm GM. Restenosis after experimental angioplasty. Intimal, medial, and adventitial changes associated with constrictive remodeling. Circ Res 1995 Jun;76(6):996-1002. [doi: 10.1161/01.res.76.6.996] [Medline: 7758171]
115. Thiele H, Oettel S, Jacobs S, Hambrecht R, Sick P, Gummert JF, et al. Comparison of bare-metal stenting with minimally invasive bypass surgery for stenosis of the left anterior descending coronary artery. Circulation 2005 Nov 29;112(22):3445-3450. [doi: 10.1161/circulationaha.105.578492]
116. Komatsu R, Ueda M, Naruko T, Kojima A, Becker AE. Neointimal tissue response at sites of coronary stenting in humans: macroscopic, histological, and immunohistochemical analyses. Circulation 1998 Jul 21;98(3):224-233. [doi: 10.1161/01.cir.98.3.224] [Medline: 9697822]
117. Liu MW, Hearn JA, Luo JF, Anderson PG, Roubin GS, Iyer S, et al. Reduction of thrombus formation without inhibiting coagulation factors does not inhibit intimal hyperplasia after balloon injury in pig coronary arteries. Coron Artery Dis 1996 Sep;7(9):667-671. [doi: 10.1097/00019501-199609000-00008] [Medline: 8950497]
118. Smith-Norowitz TA, Shani J, Weiser W, Schulhoff N, Norowitz K, Lichstein E, et al. Lymphocyte activation in angina pectoris. Clin Immunol 1999 Nov;93(2):168-175. [doi: 10.1006/clim.1999.4776] [Medline: 10527693]
119. Picard FJ, Bergeron MG. Rapid molecular theranostics in infectious diseases. Drug Discov Today 2002 Nov 01;7(21):1092-1101. [doi: 10.1016/s1359-6446(02)02497-2] [Medline: 12546841]
120. Libby P. Atherosclerosis: the new view. Sci Am 2002 May;286(5):46-55. [doi: 10.1038/scientificamerican0502-46] [Medline: 11951331]
121. Lekshmi KM, Che H, Cho C, Park I. Drug- and gene-eluting stents for preventing coronary restenosis. Chonnam Med J 2017 Jan;53(1):14-27 [FREE Full text] [doi: 10.4068/cmj.2017.53.1.14] [Medline: 28184335]
122. Klugherz BD, Jones PL, Cui X, Chen W, Meneveau NF, DeFelice S, et al. Gene delivery from a DNA controlled-release stent in porcine coronary arteries. Nat Biotechnol 2000 Nov;18(11):1181-1184. [doi: 10.1038/81176] [Medline: 11062438]
123. Yang J, Zeng Y, Zhang C, Chen Y, Yang Z, Li Y, et al. The prevention of restenosis in vivo with a VEGF gene and paclitaxel co-eluting stent. Biomaterials 2013 Feb;34(6):1635-1643 [FREE Full text] [doi: 10.1016/j.biomaterials.2012.11.006] [Medline: 23199742]
124. Paul A, Shao W, Shum-Tim D, Prakash S. The attenuation of restenosis following arterial gene transfer using carbon nanotube coated stent incorporating TAT/DNA(Ang1+Vegf) nanoparticles. Biomaterials 2012 Oct;33(30):7655-7664. [doi: 10.1016/j.biomaterials.2012.06.096] [Medline: 22818986]
125. Ji R, Cheng Y, Yue J, Yang J, Liu X, Chen H, et al. MicroRNA expression signature and antisense-mediated depletion reveal an essential role of MicroRNA in vascular neointimal lesion formation. Circulation Research 2007 Jun 08;100(11):1579-1588. [doi: 10.1161/circresaha.106.141986]
126. Che H, Bae I, Lim KS, Song IT, Lee H, Muthiah M, et al. Suppression of post-angioplasty restenosis with an Akt1 siRNA-embedded coronary stent in a rabbit model. Biomaterials 2012 Nov;33(33):8548-8556. [doi: 10.1016/j.biomaterials.2012.07.045] [Medline: 22940215]
127. Fishbein I, Alferiev I, Bakay M, Stachelek SJ, Sobolewski P, Lai M, et al. Local delivery of gene vectors from bare-metal stents by use of a biodegradable synthetic complex inhibits in-stent restenosis in rat carotid arteries. Circulation 2008 Apr 22;117(16):2096-2103. [doi: 10.1161/circulationaha.107.746412]
128. Kim TG, Lee Y, Park TG. Controlled gene-eluting metal stent fabricated by bio-inspired surface modification with hyaluronic acid and deposition of DNA/PEI polyplexes. Int J Pharm 2010 Jan 15;384(1-2):181-188. [doi: 10.1016/j.ijpharm.2009.09.042] [Medline: 19799974]
129. Hannan MA, Mutashar S, Samad SA, Hussain A. Energy harvesting for the implantable biomedical devices: issues and challenges. BioMed Eng OnLine 2014 Jun 20;13(1):1. [doi: 10.1186/1475-925x-13-79]
130. Takahata K, Gianchandani Y. A planar approach for manufacturing cardiac stents: design, fabrication, and mechanical evaluation. J. Microelectromech. Syst 2004 Dec;13(6):933-939. [doi: 10.1109/jmems.2004.838357]

131. Want R. An introduction to RFID technology. IEEE Pervasive Comput 2006 Jan;5(1):25-33. [doi: 10.1109/mprv.2006.2]
132. Chow EY, Beier BL, Francino A, Chappell WJ, Irazoqui PP. Toward an implantable wireless cardiac monitoring platform integrated with an FDA-approved cardiovascular stent. J Interv Cardiol 2009 Oct 05;22(5):479-487 [FREE Full text] [doi: 10.1111/j.1540-8183.2009.00483.x] [Medline: 19807844]
133. Kanda Y. Piezoresistance effect of silicon. Sensors and Actuators A: Physical 1991 Jul;28(2):83-91. [doi: 10.1016/0924-4247(91)85017-I]
134. Zeng S, Baillargeat D, Ho H, Yong K. Nanomaterials enhanced surface plasmon resonance for biological and chemical sensing applications. Chem Soc Rev 2014 May 21;43(10):3426-3452. [doi: 10.1039/c3cs60479a] [Medline: 24549396]
135. Akar O, Akin T, Najafi K. A wireless batch sealed absolute capacitive pressure sensor. Sensors and Actuators A: Physical 2001 Dec;95(1):29-38. [doi: 10.1016/s0924-4247(01)00753-1]
136. Chow EY, Chlebowski AL, Chakraborty S, Chappell WJ, Irazoqui PP. Fully wireless implantable cardiovascular pressure monitor integrated with a medical stent. IEEE Trans. Biomed. Eng 2010 Jun;57(6):1487-1496. [doi: 10.1109/tbme.2010.2041058]
137. Pan CT, Yang H, Shen SC, Chou MC, Chou HP. A low-temperature wafer bonding technique using patternable materials. Journal of Micromechanics and Microengineering 2002 Jun 21;12(5):611-615 [FREE Full text] [doi: 10.1088/0960-1317/12/5/315]
138. Svasek P, Svasek E, Lendl B, Vellekoop M. Fabrication of miniaturized fluidic devices using SU-8 based lithography and low temperature wafer bonding. Sensors and Actuators A: Physical 2004 Sep;115(2-3):591-599. [doi: 10.1016/j.sna.2004.03.055]

Abbreviations

AI: artificial intelligence
CAD: coronary artery disease
CTA: computed tomography angiography
CVD: cardiovascular disease
H2O2: hydrogen peroxide
MI: myocardial infarction
pHEMA: poly(hydroxyethyl) methacrylate
PLGA: polylactic-polyglycolic acid
PRS: polygenic risk score
ROS: reactive oxygen species

Edited by A Teles; submitted 13.08.24; peer-reviewed by Y Xu, W Cui, D Sun; comments to author 13.12.24; revised version received 22.12.24; accepted 08.01.25; published 08.03.25.

Please cite as:
Lee Y, Shelke S, Lee C
Cardiac Repair and Regeneration via Advanced Technology: Narrative Literature Review
JMIR Biomed Eng 2025;10:e65366
URL: https://biomedeng.jmir.org/2025/1/e65366
doi:10.2196/65366
PMID:

Optimizing Voice Sample Quantity and Recording Settings for the Prediction of Type 2 Diabetes Mellitus: Retrospective Study

Atousa Assadi, MSc, MEng; Jessica Oreskovic, MAS; Jaycee Kaufman, MSc; Yan Fossat, MSc

Klick Applied Sciences, 175 Bloor St East, North Tower, 3rd floor, Toronto, ON, Canada

Corresponding Author:
Yan Fossat, MSc
Klick Applied Sciences, 175 Bloor St East, North Tower, 3rd floor, Toronto, ON, Canada

Abstract

Background: The use of acoustic biomarkers derived from speech signals is a promising non-invasive technique for diagnosing type 2 diabetes mellitus (T2DM). Despite its potential, there remains a critical gap in knowledge regarding the optimal number of voice recordings and recording schedule necessary to achieve effective diagnostic accuracy.

Objective: This study aimed to determine the optimal number of voice samples and the ideal recording schedule (frequency and timing), required to maintain the T2DM diagnostic efficacy while reducing patient burden.

Methods: We analyzed voice recordings from 78 adults (22 women), including 39 individuals diagnosed with T2DM. Participants had a mean (SD) age of 45.26 (10.63) years and mean (SD) BMI of 28.07 (4.59) kg/m². In total, 5035 voice recordings were collected, with a mean (SD) of 4.91 (1.45) recordings per day; higher adherence was observed among women (5.13 [1.38] vs 4.82 [1.46] in men). We evaluated the diagnostic accuracy of a previously developed voice-based model under different recording conditions. Segmented linear regression analysis was used to assess model accuracy across varying numbers of voice recordings, and the Kendall tau correlation was used to measure the relationship between recording settings and accuracy. A significance threshold of $P<.05$ was applied.

Results: Our results showed that including up to 6 voice recordings notably improved the model accuracy for T2DM compared to using only one recording, with accuracy increasing from 59.61 to 65.02 for men and from 65.55 to 69.43 for women. Additionally, the day on which voice recordings were collected did not significantly affect model accuracy ($P>.05$). However, adhering to recording within a single day demonstrated higher accuracy, with accuracy of 73.95% for women and 85.48% for men when all recordings were from the first and second days.

Conclusions: This study underscores the optimal voice recording settings to reduce patient burden while maintaining diagnostic efficacy.

(JMIR Biomed Eng 2025;10:e64357) doi:10.2196/64357

KEYWORDS

vocal biomarker; acoustic biomarker; voice analysis; type 2 diabetes; diagnostics; digital phenotyping; voice data

Introduction

Diabetes mellitus is a chronic metabolic disorder characterized by persistent elevated blood glucose levels due to inadequate or impaired insulin production or utilization. It affects 10.5% of the worldwide population (536.6 million people) [1], with type 2 diabetes mellitus (T2DM) accounting for 90% of cases [2]. Uncontrolled diabetes is a major contributors to cardiovascular disorders, blindness, renal failure, and lower limb amputation [2].

Traditional diagnostic methods of fasting plasma glucose and oral glucose tolerance tests involve blood sampling, which can cause inconvenience or discomfort to patients owing to frequent monitoring. Moreover, the lack of a glucometer and the time spent for self-testing are barriers in the self-management of diabetes [3,4]. In response to these challenges, acoustic biomarkers from speech signals have emerged as promising non-invasive alternatives, offering a convenient solution for diagnosing and monitoring diabetes, especially for individuals in remote areas with restricted health care accessibility.

Sustained periods of high blood glucose and the detrimental effects of peripheral neuropathy and myopathy in individuals with T2DM impact the elastic properties of the vocal folds [5], weaken the laryngeal muscles, and induce respiratory changes [6]. These physiological changes can affect voice parameters, leading to voice disorders like hoarseness [7] and dysphagia [8]. Consequently, compared to those without T2DM, individuals with the condition exhibit significant vocal differences, quantified by phonation time, fundamental frequency, jitters, and shimmers [6], highlighting the importance of investigating vocal variations as potential markers of T2DM [9-13].

Our group previously assessed the feasibility of using voice recordings from mobile applications to detect T2DM [14]. Our results demonstrated that voice biomarkers—specifically pitch, jitters, and shimmers—combined with age and BMI could predict T2DM with an accuracy of 0.89 for women and 0.86 for men [14]. However, requiring participants to record their voices at least 6 times daily over a 2-week period posed challenges related to participant burden and recording consistency.

Therefore, this study aims to optimize the voice sampling process by determining (1) the minimum number of voice samples required, and (2) the optimal recording schedule (frequency and timing) needed to maintain diagnostic accuracy while reducing participant burden. We hypothesize that a more streamlined voice sampling protocol can achieve comparable predictive performance to prior studies while improving feasibility for long-term diabetes monitoring.

Methods

Study Design

To address the objectives of this project, we designed a retrospective study based on our previously developed model and the same dataset that yielded the highest balanced accuracy [14]. The original data collection took place between August 30, 2021, and June 30, 2022 in India [14]. In total, 505 participants (mean [SD] age 41.03 [13.29] years, 336 male participants) were recruited and instructed to record a short English phrase ("Hello. How are you? What is my glucose level right now?") up to 6 times daily using their smartphone for 14 consecutive days.

Participants and Measurements

A balanced subset of the original dataset was used for this analysis and included 78 participants (aged >18 years old, 22 women), with 39 diagnosed with T2DM [14]. Participants in the T2DM and non-T2DM groups were matched for age and BMI to minimize the demographic impact on voice recordings (Table 1). A T2DM diagnosis was confirmed by a physician according to the American Diabetes Association guidelines [15]. All participants were nonsmokers, had no diagnosed neurological or speech impairments, and signed the consent forms.

Table . Patient demographic characteristics.

Variable	Total	Non-T2DM[a] group	T2DM group
N (%)	78 (100.0)	39 (50.0)	39 (50.0)
Women	22 (28.21)	11 (50.0)	11 (50.0)
Men	56 (71.79)	28 (50.0)	28 (50.0)
Age (years), mean (SD)	45.26 (10.63)	45.49 (10.8)	45.03 (10.58)
Women	45.82 (10.4)	45.91 (10.85)	45.73 (10.47)
Men	45.04 (10.8)	45.32 (10.98)	44.75 (10.8)
BMI (kg/m^2), mean (SD)	28.07 (4.59)	28.77 (5.01)	27.36 (4.06)
Women	30.25 (5.35)	31.41 (5.4)	29.09 (5.29)
Men	27.21 (3.98)	27.74 (4.53)	26.68 (3.34)

[a]T2DM: type 2 diabetes mellitus.

As part of the study protocol, participants recorded their voice at least 6 times per day over a 2-week period using a custom mobile application installed on their personal cell phones. These recordings took place either at home or in a quiet environment with minimal background noise [12]. To establish a consistent starting point, a participant's first day (d01) was defined as the day they recorded at least 2 voice samples. Voice samples recorded prior to d01 were excluded from the analysis.

Optimizing Voice Recording Quantity and Settings for Enhanced Model Accuracy

To analyze the collected voice recordings, 14 acoustic features were extracted to characterize key parameters related to pitch, intensity, harmonic noise ratio, shimmers, and jitters [14]. Features that were significantly different between the T2DM and non-T2DM groups (P<.05, Cohen d >0.02) were included in he model development pipeline, with separate models for women and men. For women, the key features were pitch SD, mean pitch, RAP jitter, and apq3 shimmer, while for men, mean intensity, apq11 shimmer, intensity SD, and ppq5 jitter were used. A 5-fold cross-validation was performed for feature selection, threshold determination, and model optimization based on the best predictive balanced accuracy [14]. The optimal model for women was a logistic regression model (threshold of 0.3) with BMI and 3 voice features: mean pitch, pitch SD, and RAP jitter. For men, the optimal model was a naive Bayes classifier (threshold of 0.215) with age, BMI, and 2 voice features: mean intensity and apq11 shimmer.

The analysis pipeline included (1) indicating the optimal number of voice recordings for effective T2DM classification based on changes in model accuracy across varying quantities of voice samples, and (2) studying the effect of voice recording configurations on predictive performance (Multimedia Appendix 1).

To study the changes in the model's accuracy trend across varying number of voice samples, we employed segmented linear regression by fitting two distinct linear models to the data before and after the n voice samples breakpoint. The Kendall tau measure of correlation was used to investigate the strength and direction of the relationship between ordinal variables (such as days) and model accuracy. *P* values of .05 were considered statistically significant.

Ethical Considerations

The protocol (ID MGCTS107) received ethics approval by Saanvi Ethical Research LLP (No. MGCTS/20/107 V01), all participants provided informed consent, and data were stored in a secure cloud database with no identifying information. Participants were compensated for their time; each participant received US $56.

Results

Participants and Measurements

The mean (SD) age and mean (SD) BMI of participants were 45.26 (10.63) years and 28.07 (4.59) kg/m^2, respectively (Table 1). In total, 5035 recordings were included in the analysis, and 2620 from participants with T2DM (Table 2). The mean (SD) number of daily recordings for all participants was 4.91 (1.45) with women more adherent to the protocol than men (5.13 [1.38] vs 4.82 [1.46], Multimedia Appendix 2, Figure 1).

Table . Voice recording data.

Variable	Total	Non-T2DM[a] group	T2DM group
N (%)	5035 (100)	2415 (48)	2620 (52)
Women, n (%)	1539 (30.6)	713 (46.3)	826 (53.7)
Men, n (%)	3496 (69.4)	1702 (48.7)	1794 (51.3)
Number of recordings per participant, mean (SD)	64.55 (19.53)	61.92 (21.67)	67.18 (17)
Women	69.95 (16.26)	64.82 (19.12)	75.09 (11.45)
Men	62.43 (20.42)	60.79 (22.82)	64.07 (17.97)

[a]T2DM: type 2 diabetes mellitus.

Figure 1. The accuracy of the model using different number of voice recordings. The lines present the average accuracy for men (blue) and women (red). The shaded area shows the confidence interval. The numbers in the figure show the number of participants whose data were included in the analysis per day.

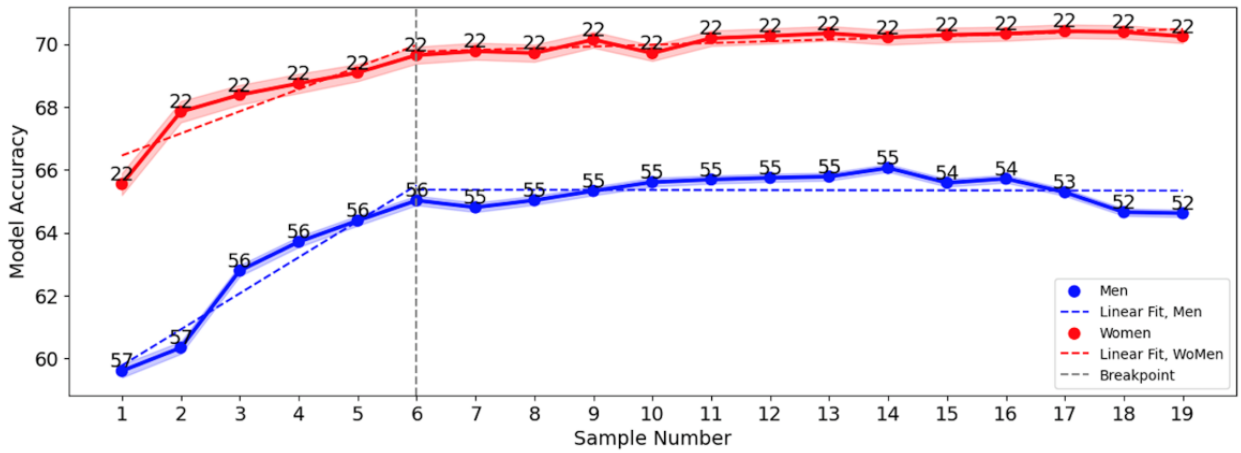

Optimizing Voice Recording Quantity and Settings for Enhanced Model Accuracy

Both in men and women, the model accuracy improved with the inclusion of up to 6 voice samples, after which it stabilized with no significant improvement (Figure 1). The changes in the slope of the linear fit were −1.15 for men and −0.65 for women, indicating a faster accuracy improvement in men than in women with the addition of initial voice samples.

Considering 6 voice samples for effective T2DM diagnosis, the highest model accuracy was achieved with recordings from day 1 in men, while for women, the peak accuracy was observed with recordings from day 10 (Figure 2). However, the variations in model accuracy across different days were not significant, and no statistically discernible trend was observed (*P*=.23 for men, *P*=.27 for women). The model accuracy was generally higher for women than for men on most days, although the difference was not statistically significant, as indicated by the overlapping confidence intervals.

Figure 2. The accuracy of the model using 6 voice recordings per day. d: day.

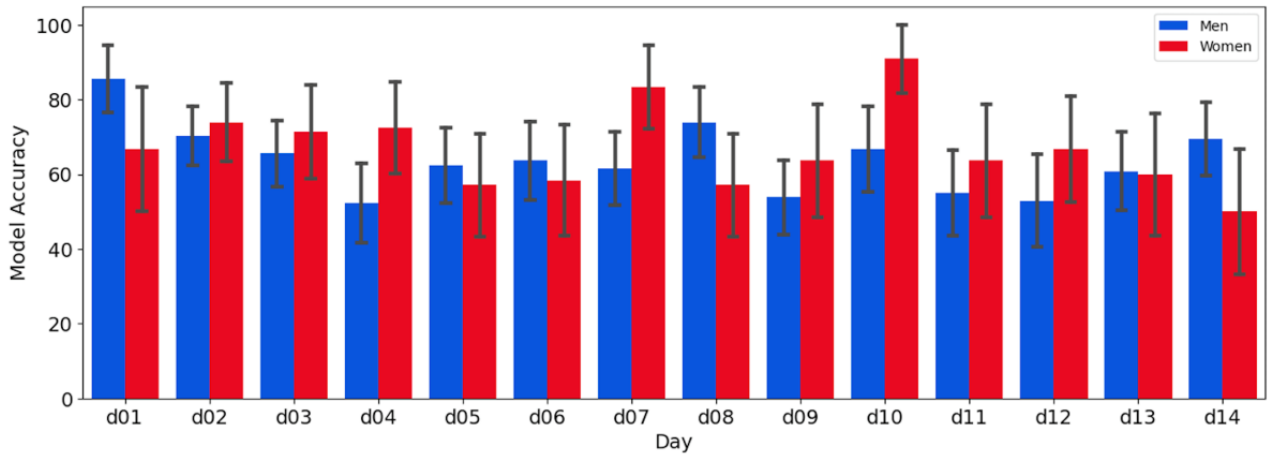

Moreover, we observed that the model accuracy was higher in men than in women when the majority of recordings were from the first day (Figure 3). As the distribution of recordings were balanced between the first and second days, the accuracy gap between men and women narrowed. Finally, when the majority of recordings were from the second day, the model accuracy was slightly higher for women than for men, with the differences in accuracy levels becoming less pronounced. Our statistical test indicated no significant trend in the model accuracy for men when using 6 recordings across 2 days (P>.99). For women, there was a significant increasing trend in the model accuracy when the majority of recordings were taken on the second day (P=.03), suggesting that consistent participation in women can improve the model performance.

Figure 3. The accuracy of the model using total 6 voice recordings from day 1 and day 2. D1: day 1, D2: day 2, N: number of samples from the day.

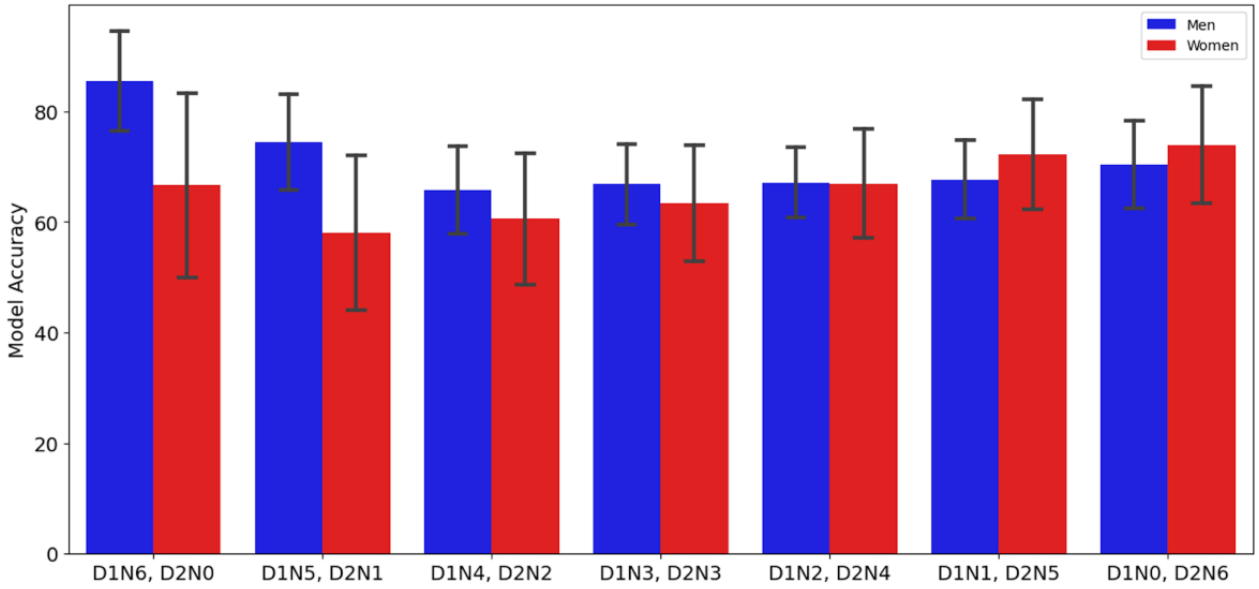

Discussion

Principal Findings

This research, to our knowledge, is the first to investigate the optimal balance between the number and settings of voice recordings for effective T2DM diagnosis, with the goal of reducing patient burden. Our findings indicated that 6 voice recordings are sufficient to maintain diagnostic accuracy, improving patient compliance and accessibility for T2DM screening. No significant differences in model accuracy were observed across different days while adherence to recording in a single day showed higher accuracy. This study lays the groundwork for future research and clinical applications focused on optimizing health care delivery for T2DM.

Comparison to Prior Works

Previous studies have shown that an increased burden from the treatment and self-management of chronic health conditions such as T2DM is associated with higher levels of distress, lower adherence to self-care routines, decreased satisfaction with medications, reduced quality of life, poorer physical and mental health, and greater risk of complications and deaths [4,16-18]. In alignment with these, our study demonstrated that up to 6 voice recordings are sufficient to effectively diagnose T2DM,

thereby reducing patient burden while maintaining diagnostic accuracy.

There are conflicting reports on self-management among men and women. While Zhou et al [19] observed that women exhibited greater compliance in self-care than men did, Mogre et al [20] reported higher self-monitoring of blood glucose in men. In our study, despite the lower number of women participants than men, women showed a higher adherence to the voice recording protocol. This higher adherence among women may explain the observed increase in model accuracy, as recordings were distributed across 2 days, suggesting that consistent participation enhances the model performance.

Prior research has reported no significant day-to-day variability in voice recordings while there exists a significant time-of-day influence on acoustics with voice quality enhanced with increased voice use [21,22]. In alignment with these findings, our results showed that both in men and in women, the model accuracy was not significantly different between days while there was an increase in accuracy when the majority of the recordings were from a single day. Due to the limited distribution of samples across different times of the day, we were unable to assess the time-of-day variability.

Strengths and Limitations

This study provides important insights into optimizing voice-based T2DM diagnostics while minimizing participant burden. However, several limitations should be considered. First, there was a limited sample size of women. The smaller number of women participants may reduce the generalizability of our findings, particularly regarding sex-specific effects. Future studies with larger, more balanced datasets are needed to validate these observations. Second, our relatively small dataset limited the use of more advanced machine learning techniques, such as neural networks. While these models may offer further improvements in the diagnostic accuracy and insight into optimal data collection strategies, future studies with larger datasets are required to fully explore their potential. Third, due to uneven distribution of recordings across different times of the day, we could not assess how the time-of-day influences voice-based diagnostics. Future studies should implement controlled recording schedules to systematically examine these effects.

Acknowledgments

This research was internally funded by Klick Inc.

Data Availability

Data were commissioned by Klick Health, a private business, and are owned by Klick who does not allow sharing them.

Authors' Contributions

All authors contributed to preparing this manuscript. AA selected the analysis pipeline, performed data analysis, and prepared the manuscript. JO contributed to data analysis and revised and edited the manuscript. JK developed the voice classification model and provided feedback in methodology, data analysis, and reviewing the manuscript. YF supervised all aspects of the project, provided funding resources, and was involved in reviewing and submitting the manuscript.

Conflicts of Interest

JO, JK, and YF are employees of Klick Inc.

Multimedia Appendix 1
Methods for optimizing voice recording quantity and settings for enhanced model accuracy.
[DOCX File, 15 KB - biomedeng_v10i1e64357_app1.docx]

Multimedia Appendix 2
Number of daily voice recordings per participant.
[DOCX File, 135 KB - biomedeng_v10i1e64357_app2.docx]

References

1. Sun H, Saeedi P, Karuranga S, et al. IDF diabetes atlas: Global, regional and country-level diabetes prevalence estimates for 2021 and projections for 2045. Diabetes Res Clin Pract 2022 Jan;183:109119. [doi: 10.1016/j.diabres.2021.109119] [Medline: 34879977]
2. Goyal R, Singhal M, Jialal I. Type 2 Diabetes: StatPearls; 2024. URL: https://www.ncbi.nlm.nih.gov/books/NBK513253/ [accessed 2025-06-25]
3. Mogre V, Johnson NA, Tzelepis F, Paul C. Barriers to diabetic self-care: a qualitative study of patients' and healthcare providers' perspectives. J Clin Nurs 2019 Jun;28(11-12):2296-2308. [doi: 10.1111/jocn.14835] [Medline: 30791160]
4. Gonzalez JS, Tanenbaum ML, Commissariat PV. Psychosocial factors in medication adherence and diabetes self-management: Implications for research and practice. Am Psychol 2016 Oct;71(7):539-551. [doi: 10.1037/a0040388] [Medline: 27690483]

5. Sidorova J, Carbonell P, Čukić M. Blood glucose estimation from voice: first review of successes and challenges. J Voice 2022 Sep;36(5):737. [doi: 10.1016/j.jvoice.2020.08.034] [Medline: 33041176]
6. Saghiri MA, Vakhnovetsky A, Vakhnovetsky J. Scoping review of the relationship between diabetes and voice quality. Diabetes Res Clin Pract 2022 Mar;185:109782. [doi: 10.1016/j.diabres.2022.109782] [Medline: 35176400]
7. Hamdan AL, Kurban Z, Azar ST. Prevalence of phonatory symptoms in patients with type 2 diabetes mellitus. Acta Diabetol 2013 Oct;50(5):731-736. [doi: 10.1007/s00592-012-0392-3] [Medline: 22527095]
8. Weinreb SF, Piersiala K, Hillel AT, Akst LM, Best SR. Dysphonia and dysphagia as early manifestations of autoimmune inflammatory myopathy. Am J Otolaryngol 2021;42(1):102747. [doi: 10.1016/j.amjoto.2020.102747] [Medline: 33038783]
9. Pinyopodjanard S, Suppakitjanusant P, Lomprew P, Kasemkosin N, Chailurkit L, Ongphiphadhanakul B. Instrumental acoustic voice characteristics in adults with type 2 diabetes. J Voice 2021 Jan;35(1):116-121. [doi: 10.1016/j.jvoice.2019.07.003] [Medline: 31427120]
10. Gölaç H, Atalik G, Türkcan AK, Yilmaz M. Disease related changes in vocal parameters of patients with type 2 diabetes mellitus. Logoped Phoniatr Vocol 2022 Oct;47(3):202-208. [doi: 10.1080/14015439.2021.1917653] [Medline: 33970753]
11. Chitkara D, Sharma RK. Voice based detection of type 2 diabetes mellitus. Presented at: 2016 2nd International Conference on Advances in Electrical, Electronics, Information, Communication and Bio-Informatics (AEEICB); Feb 27-28, 2016; Chennai, India p. 83-87. [doi: 10.1109/AEEICB.2016.7538402]
12. Kaufman J, Jeon J, Oreskovic J, Fossat Y. Linear effects of glucose levels on voice fundamental frequency in type 2 diabetes and individuals with normoglycemia. Sci Rep 2024 Aug 28;14(1):19012. [doi: 10.1038/s41598-024-69620-z] [Medline: 39198592]
13. Oreskovic J, Kaufman J, Fossat Y. Impact of audio data compression on feature extraction for vocal biomarker detection: validation study. JMIR Biomed Eng 2024 Apr 15;9:e56246. [doi: 10.2196/56246] [Medline: 38875677]
14. Kaufman JM, Thommandram A, Fossat Y. Acoustic analysis and prediction of type 2 diabetes mellitus using smartphone-recorded voice segments. Mayo Clin Proc Digit Health 2023 Dec;1(4):534-544. [doi: 10.1016/j.mcpdig.2023.08.005] [Medline: 40206319]
15. American Diabetes Association Professional Practice Committee. 2. Classification and diagnosis of diabetes: standards of medical care in diabetes-2022. Diabetes Care 2022 Jan 1;45(Suppl 1):S17-S38. [doi: 10.2337/dc22-S002] [Medline: 34964875]
16. Eton DT, Yost KJ, Lai JS, et al. Development and validation of the patient experience with treatment and self-management (PETS): a patient-reported measure of treatment burden. Qual Life Res 2017 Feb;26(2):489-503. [doi: 10.1007/s11136-016-1397-0] [Medline: 27566732]
17. Jannoo Z, Mamode Khan N. Medication adherence and diabetes self-care activities among patients with type 2 diabetes mellitus. Value Health Reg Issues 2019 May;18:30-35. [doi: 10.1016/j.vhri.2018.06.003] [Medline: 30419448]
18. Chen Y, Sloan FA, Yashkin AP. Adherence to diabetes guidelines for screening, physical activity and medication and onset of complications and death. J Diabetes Complications 2015;29(8):1228-1233. [doi: 10.1016/j.jdiacomp.2015.07.005] [Medline: 26316423]
19. Zhou C, Chen J, Tan F, et al. Relationship between self-care compliance, trust, and satisfaction among hypertensive patients in China. Front Public Health 2022;10:1085047. [doi: 10.3389/fpubh.2022.1085047] [Medline: 36743158]
20. Mogre V, Abanga ZO, Tzelepis F, Johnson NA, Paul C. Adherence to and factors associated with self-care behaviours in type 2 diabetes patients in Ghana. BMC Endocr Disord 2017 Mar 24;17(1):20. [doi: 10.1186/s12902-017-0169-3] [Medline: 28340613]
21. Heald SLM, Nusbaum HC. Variability in vowel production within and between days. PLoS ONE 2015;10(9):e0136791. [doi: 10.1371/journal.pone.0136791] [Medline: 26331478]
22. Pierce JL, Tanner K, Merrill RM, Shnowske L, Roy N. Acoustic variability in the healthy female voice within and across days: how much and why? J Speech Lang Hear Res 2021 Aug 9;64(8):3015-3031. [doi: 10.1044/2021_JSLHR-21-00018] [Medline: 34269598]

Abbreviations

T2DM: type 2 diabetes mellitus

Edited by S Rizvi, T Leung; submitted 15.07.24; peer-reviewed by V Martin, Z Wang; revised version received 03.06.25; accepted 04.06.25; published 26.06.25.

Please cite as:
Assadi A, Oreskovic J, Kaufman J, Fossat Y
Optimizing Voice Sample Quantity and Recording Settings for the Prediction of Type 2 Diabetes Mellitus: Retrospective Study
JMIR Biomed Eng 2025;10:e64357
URL: https://biomedeng.jmir.org/2025/1/e64357
doi:10.2196/64357

Using Vibration for Secure Pairing With Implantable Medical Devices: Development and Usability Study

Mo Zhang[1,2], PhD; Chaofan Wang[3], PhD; Weiwei Jiang[4], PhD; David Oswald[1], PhD; Toby Murray[2], PhD; Eduard Marin[5], PhD; Jing Wei[2], PhD; Mark Ryan[1], PhD; Vassilis Kostakos[2], PhD

[1]School of Computer Science, University of Birmingham, Birmingham, United Kingdom

[2]School of Computing and Information Systems, The University of Melbourne, Melbourne Connnect, 700 Swanston Street, Carlton, Melbourne, Australia

[3]College of Computer Science and Artificial Intelligence, Wenzhou University, Wenzhou, China

[4]School of Computer Science, Nanjing University of Information Science and Technology, Nanjing, China

[5]Telefonica Research Spain, Barcelona, Spain

Corresponding Author:
Mo Zhang, PhD
School of Computer Science, University of Birmingham, Birmingham, United Kingdom

Abstract

Background: Implantable medical devices (IMDs), such as pacemakers, increasingly communicate wirelessly with external devices. To secure this wireless communication channel, a pairing process is needed to bootstrap a secret key between the devices. Previous work has proposed pairing approaches that often adopt a “seamless” design and render the pairing process imperceptible to patients. This lack of user perception can significantly compromise security and pose threats to patients.

Objective: The study aimed to explore the use of highly perceptible vibrations for pairing with IMDs and aim to propose a novel technique that leverages the natural randomness in human motor behavior as a shared source of entropy for pairing, potentially deployable to current IMD products.

Methods: A proof of concept was developed to demonstrate the proposed technique. A wearable prototype was built to simulate an individual acting as an IMD patient (real patients were not involved to avoid potential risks), and signal processing algorithms were devised to use accelerometer readings for facilitating secure pairing with an IMD. The technique was thoroughly evaluated in terms of accuracy, security, and usability through a lab study involving 24 participants.

Results: Our proposed pairing technique achieves high pairing accuracy, with a zero false acceptance rate (indicating low risks from adversaries) and a false rejection rate of only 0.6% (1/192; suggesting that legitimate users will likely experience very few failures). Our approach also offers robust security, which passes the National Institute of Standards and Technology statistical tests (with all P values >.01). Moreover, our technique has high usability, evidenced by an average System Usability Scale questionnaire score of 73.6 (surpassing the standard benchmark of 68 for “good usability”) and insights gathered from the interviews. Furthermore, the entire pairing process can be efficiently completed within 5 seconds.

Conclusions: Vibration can be used to realize secure, usable, and deployable pairing in the context of IMDs. Our method also exhibits advantages over previous approaches, for example, lenient requirements on the sensing capabilities of IMDs and the synchronization between the IMD and the external device.

(JMIR Biomed Eng 2025;10:e57091) doi:10.2196/57091

KEYWORDS

implantable medical device; pairing; vibration; security; usability

Introduction

Background

Implantable medical devices (IMDs), such as pacemakers, implantable cardioverter defibrillators, or insulin pumps are widely deployed and evolving at a rapid pace [1]. Modern IMDs typically rely on a wireless interface to communicate with external devices. For instance, doctors use programmer devices to reprogram the patient’s IMD (eg, to change the patient’s therapy) and gather telemetry data. Such wireless connectivity can bring about much convenience to patients and doctors. However, it also poses new security and privacy threats, such as eavesdropping on sensitive medical data or hijacking life-critical functions. The consequences of such attacks can be severe because they can cause serious injuries or even death. However, these risks have often been overlooked. While no real-world attack against an IMD has been confirmed to date, previous research has demonstrated that many IMDs available

on the market today severely lack effective security mechanisms, and that attacks on patients would be practically possible [2-6].

To protect wireless communication links, it is essential for the IMD and external device to undergo a pairing process. This process aims to exchange a cryptographic key between them, which can then be used to secure the wireless channel using standard protocols [7]. However, implementing such a key exchange in a secure manner is challenging because IMDs are resource-constrained with limited memory, computational power, and nonrechargeable and nonreplaceable batteries. Moreover, IMDs do not have physically accessible input or output interfaces, such as a keyboard or a screen once they are implanted. This obstructs traditional pairing methods used in technologies like Bluetooth, where manually typing a 4-digit PIN code on the devices is a standard procedure [8]. Furthermore, network connections with these devices can be ad-hoc. For instance, in an emergency (eg, patients with cardiac implants can experience syncope symptoms and become unconscious [9]), a doctor may quickly have to use a new programmer device to connect to the patient's IMD. Due to these limitations of IMDs, conventional pairing techniques (such as the ones based on symmetric or public keys [10]) are often not a viable option [5,11].

Previous work has proposed a variety of pairing techniques to overcome this challenge [12]. Rasmussen et al [13] propose an approach where the IMD and external device send ultrasound to each other to verify each other's legitimacy and exchange a key. Marin et al [5] and Tomlinson et al [14] propose a pairing method by transmitting a low alternating current through the patient's skin and tissue. Denning et al [15] and Gollakota et al [16] propose to delegate security to a proxy device that the patient can carry around (such as a bracelet). [17-20] propose a pairing process by the IMD and external device synchronously and simultaneously measuring a human physiological signal (such as heartbeats).

Across those previous approaches, a crucial aspect has been systematically overlooked: user perception. We observe that previous work has attempted to follow a "seamless" design approach that makes the IMD pairing as unobtrusive as possible to the patient, rendering the pairing process almost imperceptible at the same time. This can prevent patients from detecting unexpected pairing attempts made by adversaries in proximity, thereby hindering their ability to appropriately respond to such security threats, for example, by seeking assistance or fleeing the scene. Although the "seamless" design principle is common in everyday security systems [21], we question its suitability in the IMD context, where the device is part of the patient, and its security is life-critical.

To address this issue, a pairing protocol needs to incorporate a perceivable and robust (ie, cannot be hidden or canceled by an adversary) signal. This leads us to consider vibration as an out-of-band (OOB) channel (ie, a communication channel other than a wireless channel) for pairing (Figure 1). Vibrations are highly perceivable and have been widely used in smart consumer devices for notification services [22]. In addition, accelerometers, the primary type of vibration receiver used in previous approaches, are already present in state-of-the-art IMDs for medical purposes [23-25]. Another advantage of using vibration is its limited range of reliable reception. In the IMD context, this implies that if an external device intends to transmit a vibration to an IMD, it must be physically attached to the patient's skin for a while [26]. If an adversary overpowers the signal with a very strong vibration from a distance, the patient can easily notice this.

Figure 1. IMD and external device. The vibration channel is used to exchange a key that subsequently secures the wireless channel. IMD: implantable medical device.

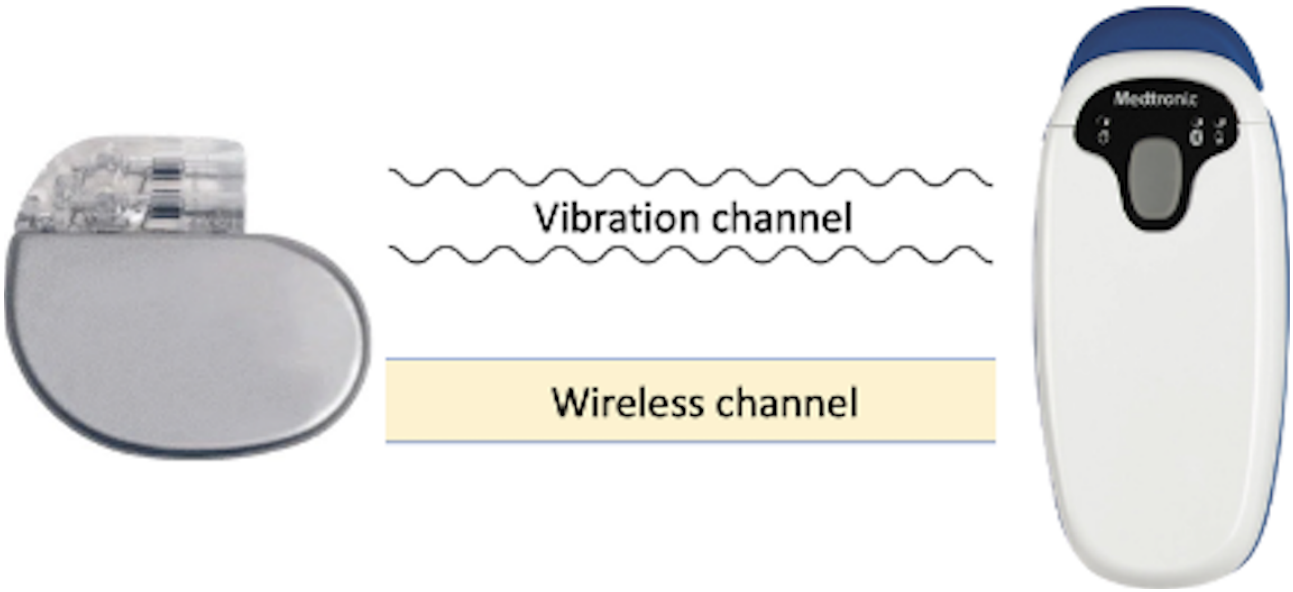

Related Work

Vibration-Based Secret Transmission in Ad-Hoc Networks

Previous work has proposed vibration as an OOB channel for transmitting secrets between 2 devices that physically contact each other [26-32]. Table 1 summarizes their application scenarios and hardware setups. Most are designed for wearables and Internet of Things (IoT) devices that are not implanted in the human body. As a common setup, the transmitter (such as a smartphone) is equipped with a vibration motor and the receiver contains a sensor to detect the vibrations, such as an accelerometer [26,27,29-31], gyroscope [32] or microphone [28].

Table . Setup for previous vibration-based secret transmission. The application context refers to the intended receiver device.

Technique	Application context	Receiver sensor type	Sampling rate (Hz)
Vibrate-to-Unlock [30]	RFID tag	Accelerometer	Not reported
SYNCVIBE [27]	Wearable	Accelerometer	1600
SecureVibe [26]	IMD[a]	Accelerometer	3200
VibroComm [32]	IoT[b] device	Gyroscope	32000
Ripple [29]	Mobile device	Accelerometer	1600
Ripple II [28]	Mobile device	Microphone	48000
Touch-And-Guard [31]	Wristband device	Accelerometer	250

[a]IMD: implantable medical device.

[b]IoT: Internet of Things.

Previous work predominantly directly embeds the secret within the vibration signal itself [26-30,32]: the transmitter encodes the secret into vibration using specific modulation methods (eg, on-off keying [26,27,33]), and the receiver picks up this vibration with a sensor and decodes the secret. Another strategy leverages vibration to "amplify" the secret from humans: Wei et al [31] propose an approach that pairs an IoT device with a wristband device. When the user (who wears the wristband) touches the IoT device, the IoT device emits a vibration that sweeps through a range of frequencies. Contrary to the above methods, the vibration here does not carry the secret and remains consistent across different sessions. Instead, the secret comes from the (to some extent random) resonant properties of the user's hand-arm area, which can be derived from the devices' accelerometer readings.

However, we argue that most work (in their current form) is not deployable in existing IMD products because they have stringent requirements on the receiver sensor. Microphones do not exist in IMDs, while inertial sensors (ie, accelerometer and gyroscope) often require sampling rates in several thousands of Hz or higher. Such high-performance sensors are rare in IMDs [34-36] and are too energy-consuming for IMDs' limited battery capacity [37]. Future studies could certainly explore if previous work remains effective at reduced sensor sampling rates such as a few hundred Hz. Nevertheless, this is likely to significantly impact the performance because vibration signal demodulation often requires sensor data with high resolution [29].

Overall, we find that only [31] demands a lower sampling rate of 250 Hz. This is because the secret relies on the resonant frequencies of the user's hand-arm region, which are situated in the low-frequency domain ranging from several to a few hundred Hz [38,39]. Nonetheless, its practicality was only validated for wristbands but has not been tested in other deployment environments or with different hardware setups.

Suitable Protocols for OOB Channel-Based Pairing

Previous work has extensively proposed using an OOB channel for pairing with resource-constrained devices, including IMDs [5,19,26,40,41]. Typically, the ultimate objective of such pairing is to establish a 128-bit cryptographic key between 2 devices for data encryption [7]. However, these works commonly propose to directly exchange the entire key through the OOB channel, which raises several concerns.

First, OOB channels often have much lower data throughput compared to conventional wireless channels. For instance, the data throughput of the aforementioned vibration-based method [31] is only 7.15 bits per second. As a result, a 128-bit key bootstrap would require at least 18 seconds, potentially posing issues of usability and safety in emergencies. Second, OOB channels face threats from advanced side-channel eavesdropping attacks. For example, a vibration channel might be compromised using microphones in proximity due to acoustic leakage, leading to severe consequences.

To mitigate these concerns, prior work has suggested using a password-authenticated key agreement (PAKE) method [19,42,43], such as Diffie-Hellman Encrypted Key Exchange [44]. PAKE is a cryptographic protocol aiming at exchanging a high-entropy cryptographic key between parties who have previously shared a short and low-entropy secret. This approach allows 2 devices to initially exchange a short bitstring, after which they execute a PAKE to further exchange a 128-bit key. The latter step can be fast and thus largely reduce the impact of the low data rate of OOB channels. In addition, PAKE provides forward secrecy and rules out offline brute-force attacks. This is the approach that we adopt in our work, and therefore we consider that vibration is only to be used to exchange an ephemeral and low-entropy secret between the IMD and the external device.

Objectives

The objective of this paper is to explore the potential of using vibration for pairing with resource-constrained IMDs. This study aimed to (1) propose a novel technique that leverages vibration to extract secrets from the naturally random human motor behavior for pairing, (2) develop a prototype as a proof-of-concept to demonstrate our technique, and (3) evaluate our prototype's accuracy, security, and usability in a lab study involving 24 participants.

Methods

Pairing Technique

The pairing process requires the user (patient or doctor) to repeatedly attach the external device to the patient's body (near the IMD's location) for a few times. In this work, each repetition was referred to as a cycle, and the complete pairing process (including several cycles) was defined as a run. Each cycle comprises three main steps:

1. Device attachment: the user attaches the external device to the body and holds it steadily.
2. Vibration broadcast*:* the external device emits a vibration signal for a short period. The signal is always the same and does not serve as the secret. Both the IMD and external device take a measurement of the acceleration. The user releases the external device when the vibration stops.
3. Randomness extraction: both devices process the sensed acceleration signal and derive a shared secret from it.

The security of pairing relies on the randomness of the shared secret, which originates from the diverse physiological characteristics of the human body as well as the inherent variability of human behavior (eg, the varying attachment position and the grip strength) [45]. The vibration signal itself remains constant in each cycle and is not a source of randomness. Instead, it serves as a "catalyst" that allows the randomness of body and motion to be reflected in the accelerometer measurements.

Obtaining a Shared Secret From Humans

The design of vibration strategy in each cycle—namely, the control of the motor to vibrate at a certain frequency for a certain time frame—is crucial. The feasibility of the aforementioned work [31] was first explored in the context of IMDs. The exact same experimental settings were replicated using our prototype that simulates the human body environment (elaborated in the following sections): the accelerometer sampling rates of the external device and IMD are set as 250 Hz. In each cycle, the motor is programmed to sweep between 20 Hz to 125 Hz within 1.75 seconds. During this period, 2 devices measure the z-axis acceleration data (aligning with the user's sagittal plane) and subsequently generate the frequency spectrum by doing fast Fourier transform (FFT) [46].

One researcher of the team performs 100 cycles as a preliminary test. The results are shown in Figure 2 (the locations of the resonant frequency peaks shared by both devices were regarded as secrets in [31]). Among all, 72 cycles show one stable peak; 17 cycles have 2 common peaks; 2 possess 3 peaks; in 9 cycles, the data is too noisy to capture any shared peaks. The results differ significantly from [31] where an average of 4 - 8 peaks can be obtained per cycle. In addition, the peaks in [31] are somehow uniformly distributed over the whole 20 - 125 Hz range, while ours are almost always in the range of 80 - 110 Hz. Our interpretation for the discrepancy in the performance of this strategy is the presence of the plastic board and shell in our prototype setup, which "masks" the resonant frequencies of the human body. Unfortunately, in the context of IMD pairing, the existence of such components (eg, a plastic or metal device housing) is inevitable.

Figure 2. Performance of the preliminary test (A) with 1 peak (72%), (B) with 2 peaks (17%), (C) with 3 peaks (2%), and (D) the noisy data (9%). IMD: implantable medical device.

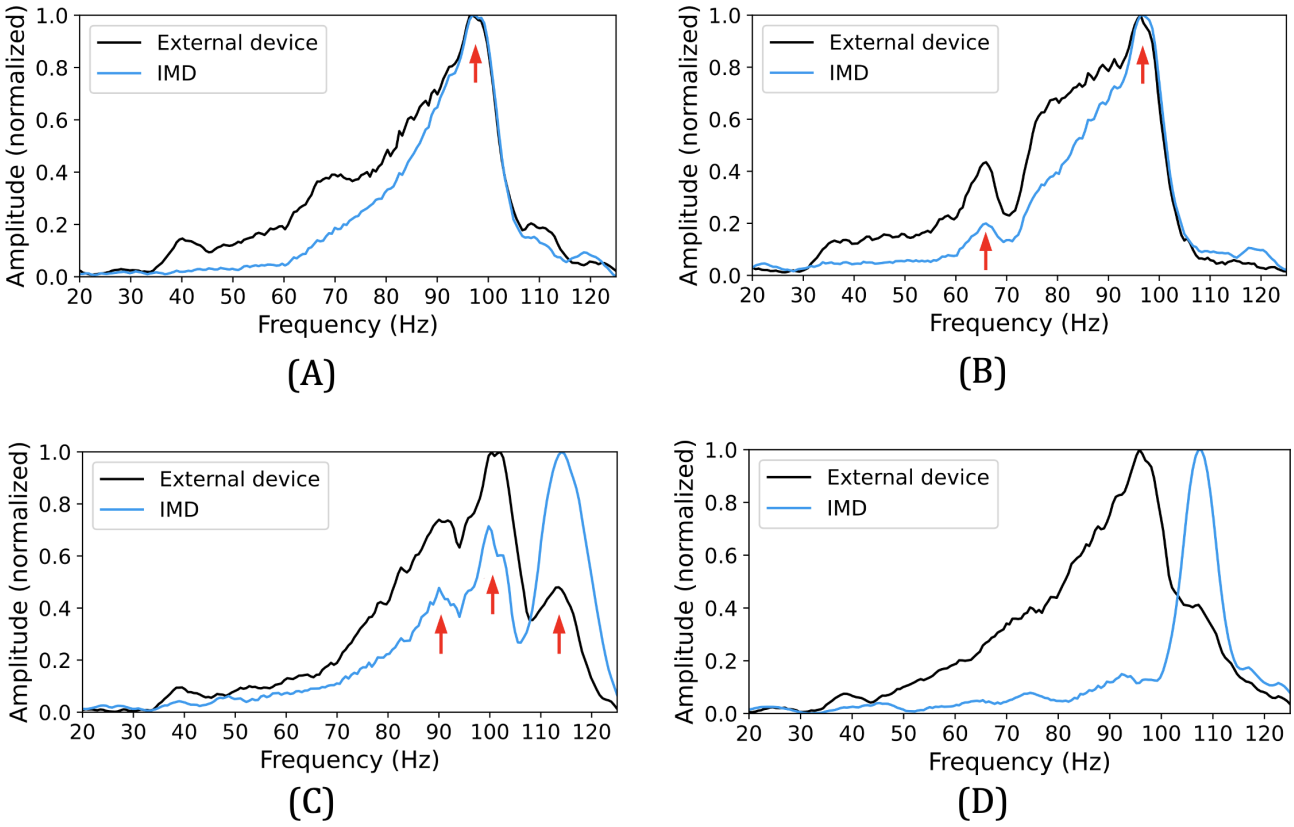

Nevertheless, the above test implies the natural randomness inherent in the user attachment motions. Intuitively, we want to test if a constant-frequency vibration is a viable option. We program the motor to emit a 50 Hz vibration for 1 s per cycle, and the same researcher executes 100 cycles using our prototype. For each cycle, we collect z-axis acceleration data from both devices and generate the frequency spectrum using FFT. Figure 3 shows an example of the frequency spectrum in one cycle. It was observed that 2 devices can obtain very similar data, especially for a prominent amplitude peak. Figure 4 illustrates the spectrum change of the IMD over ten consecutive cycles. Each row in this figure corresponds to a frequency spectrum obtained in 1 cycle, and the bright spots indicate the prominent peaks on the curve. We observe that the peak locations vary around 50 Hz, suggesting the presence of a degree of randomness. These findings indicate that providing an excitement of a constant-frequency vibration, the prominent peak location in the frequency domain is a potentially qualified shared entropy source between the IMD and the external device, which can be used for pairing purposes.

Figure 3. Frequency spectrum given a constant vibration (50 Hz, 1 s) in one cycle. IMD: implantable medical device.

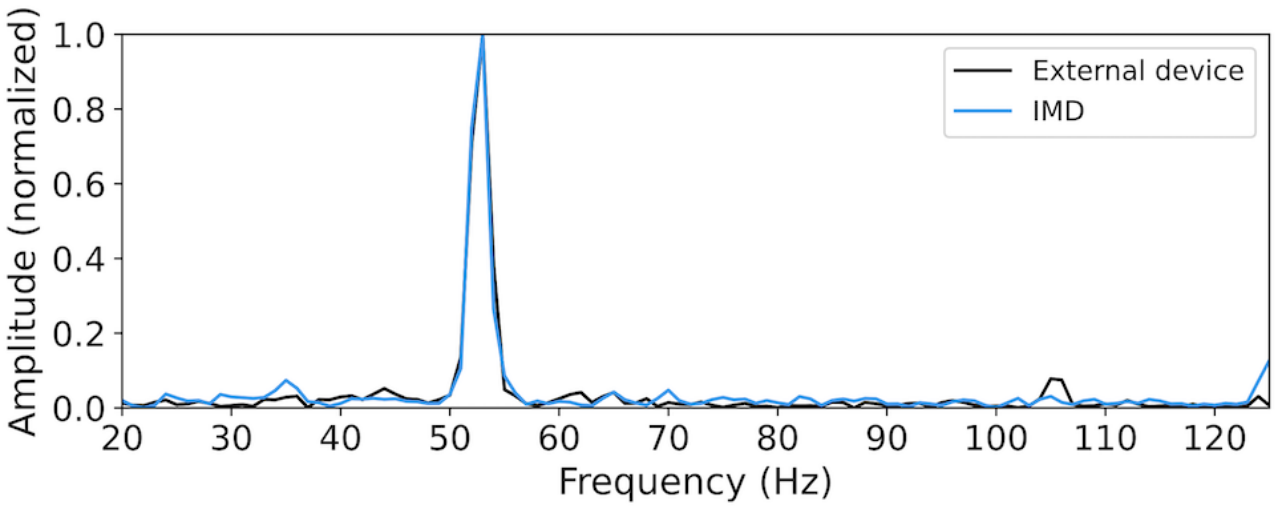

Figure 4. Frequency spectrum of IMD, given a constant vibration (50 Hz, 1 s) in 10 consecutive cycles. IMD: implantable medical device.

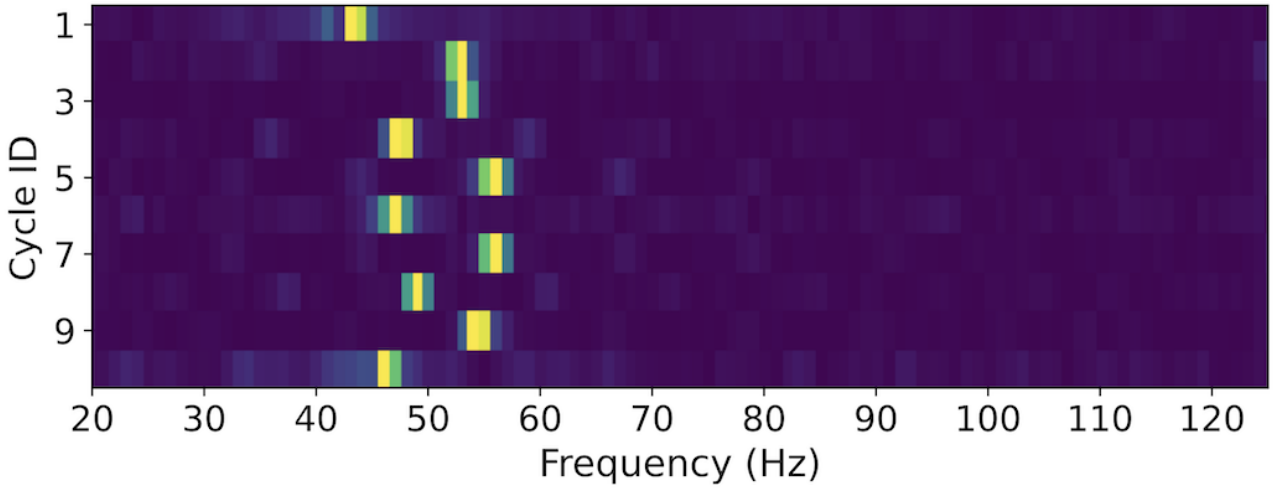

Signal Processing Workflow

Figure 5 shows the workflow of our pairing technique (assuming the IMD is a pacemaker). In each cycle, the patient holds the external device and attaches it on their chest. During the attachment, the motor vibrates, and both the IMD and the external device measure a pair of z-axis acceleration data.

Figure 5. An overview of our pairing technique. acc: accelerometer; FFT: fast Fourier transform; PAKE: password-authenticated key agreement.

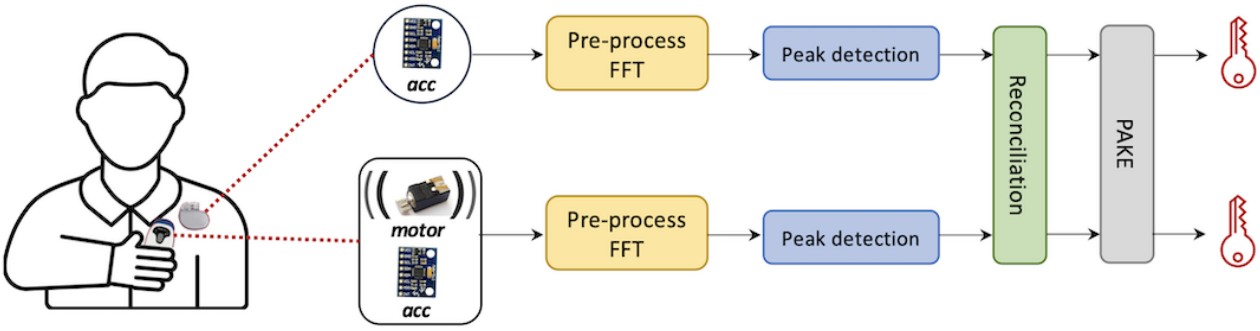

To remove the noise of the direct current component, each device subtracts the acceleration data with its mean value. In addition, when the vibration motor is switched on from standstill or switched off, the generated vibration signal is not amplified or attenuated immediately but with a slow and damped response [26,27]. This means that the transition parts (ie, 2 ends) of a vibration signal segment are often noisy. This is addressed by applying a Hanning window on the data.

Subsequently, each device applies FFT on the acceleration signal to obtain the frequency spectrum. The frequency range of 0 to 20 Hz is then excluded to avoid the effects of noisy motion artifacts like human breathing movements, as well as ambient vibrations present in the patient's environment [47]. As mentioned, there is a prominent amplitude peak in the frequency spectrum. In order to detect the location of this peak, each device simply traverses the frequency domain to find the frequency value corresponding to the maximum amplitude.

Based on the above procedure, after the user completes a pairing (ie, a run) by repeating the attachment for several times, each of the 2 devices will possess a sequence of peak locations. However, these sequences may not be exactly the same due to the measurement noise and human error (eg, hand wobbles). To resolve this, the peak locations are encoded into binary format using Gray code [48]. This coding method ensures minimal bit mismatches if the discrepant peak locations are very close on 2 devices, which is the case of our technique. Then, we use a cryptographic algorithm known as a fuzzy extractor [11,49] to reconcile any remaining bit differences between the 2 bitstrings without revealing the secret itself. If the rate of bit mismatches falls within the error-correcting capability of the fuzzy extractor, the IMD and the external device agree on an identical bitstring as a shared secret.

Adversary Model

Given our review of relevant literature about IMD pairing techniques [3,12,13,16,19,40,50], we assume a sophisticated adversary following the Dolev-Yao model [51] who has full knowledge of our pairing protocol, has full control over the wireless communication channels, and can be a man-in-the-middle (MITM) attacker by intercepting legitimate devices' signals and sending their own messages instead. In particular, the adversary can launch the following attacks relevant in the context of our pairing technique: (1) impersonation attack: the adversary uses a sequence of peak locations in an attempt to impersonate a legitimate device. They could succeed if their sequence closely matches the one measured by the IMD or external device. (2) Brute-Force attack: the adversary brute-forces possible peak location sequences and launches MITM attacks to decipher and manipulate the

communication between legitimate devices. The brute force can be done online, that is, during the pairing process, the adversary tries every possible sequence until they hit a correct one. Alternatively, this can be done offline, where the adversary records the pairing traffic and performs offline analysis to crack the secret after pairing. (3) Acoustic eavesdropping: The adversary may also attempt to eavesdrop on the vibration signals using a microphone near the patient to reveal the secret.

Experimental Setup

The proposed pairing technique was validated through the design and testing of the prototype in a user study. It was assumed that the IMD is a pacemaker implanted beneath the chest and considered the external handheld device to resemble a smartphone with a plastic casing. Moreover, both devices contain an accelerometer, and the external device is equipped with a vibration motor.

Prototype Implementation

We show an overview of our prototype in Figure 6A. The prototype consists of three main parts:

Figure 6. Experiment setup. (A) Prototype overview. (B) Hardware setup. (C) Chest simulator. (D) Participant in user study.

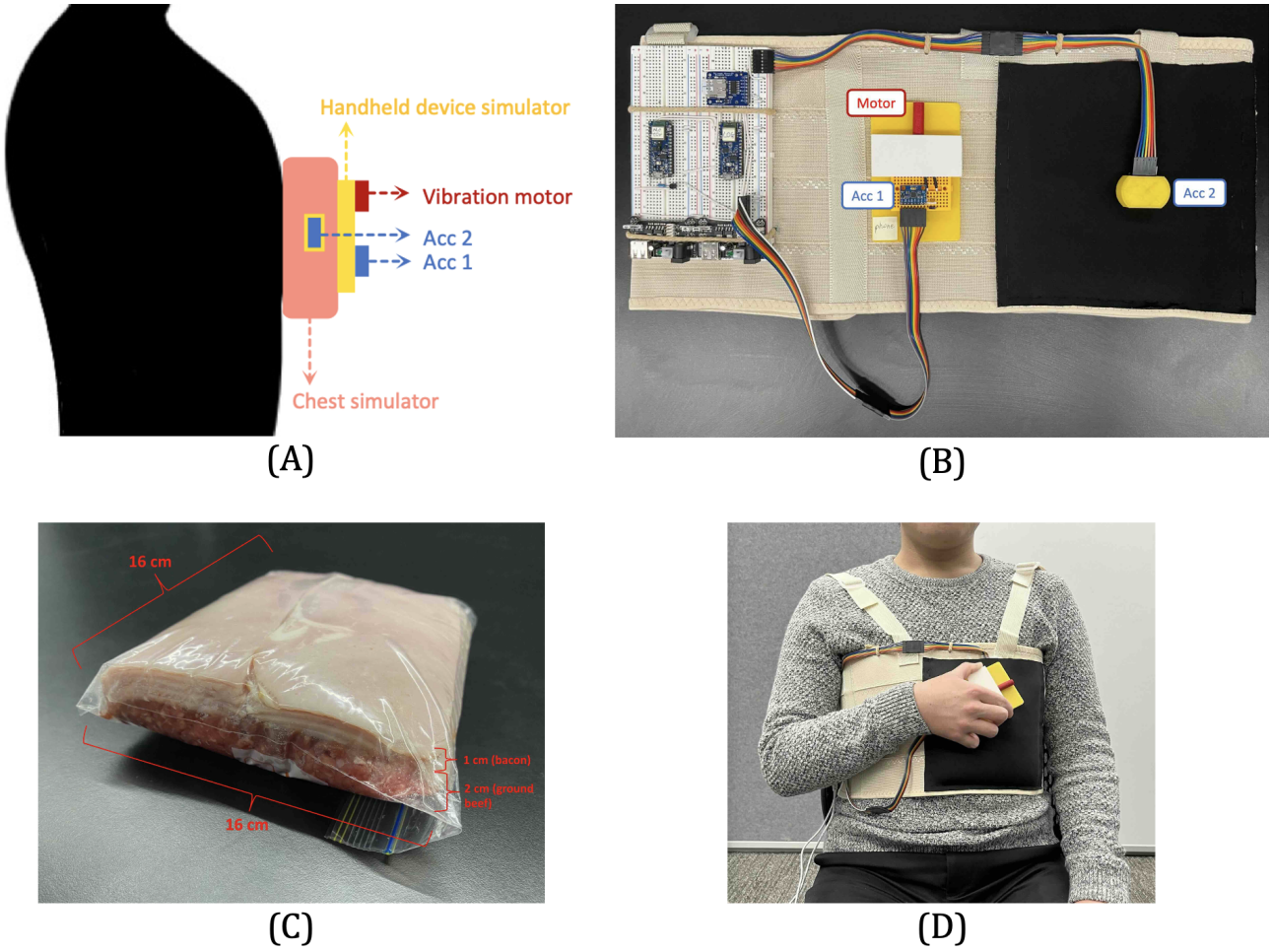

IMD

We use an InvenSense triaxial MPU-6050 accelerometer [52] to simulate a pacemaker and house it inside a 3D-printed case (Acc2 in Figure 6B). An Arduino Nano 33 BLE board interfaces with the sensor, which contains a 32-bit Cortex-M microcontroller and closely resembles the capabilities of an IMD [53]. The sampling rate of the accelerometer is set at 250 Hz, the same as in previous work [31].

External Device (the Vibration Transmitter)

We do not directly use a smartphone as the external device because the most common operating systems on mobile devices—Android and iOS systems do not provide an API interface for direct control of the vibration motor frequency. Instead, we use an eccentric rotating mass type vibration motor [54], along with another MPU-6050 sensor (Acc1 in Figure 6B) to simulate an external device. These components are mounted on an 11 cm × 7 cm × 0.5 cm plastic cuboid board, replicating the size and shape of a typical smartphone.

We use a separate Arduino Nano 33 BLE board to control both the vibration motor and the accelerometer. Particularly, this Arduino board connects to the vibration motor and supplies voltage to it. By using the pulse width modulation technique [31], the board can adjust the driving voltage, allowing the vibration motor's frequency to be altered accordingly. In addition, the accelerometer is set to a sampling rate of 250 Hz.

Chest Environment

Given that pacemakers are embedded inside the body, it is important for our experiments to mimic an environment that resembles the human chest. We adopt the design in previous research [5,26,40] and use 1 cm layer of bacon and 2 cm layer of lean ground beef to replicate the chest's physical properties (see Figure 6C). The 1 cm depth is a standard depth for pacemaker implantation [55]. In our study, we embed our pacemaker simulator within the meat layers, which are kept inside a food storage bag at room temperature. This bag of meat is subsequently placed in a pocket stitched onto an elastic chest band, positioned around an area corresponding to the human heart's location (see Figure 6B). Participants were asked to wear the chest strap throughout the user study to mimic the conditions of pacemaker users.

Participant Recruitment

We first conducted a pilot study with 6 individuals (ages 22 to 32 years, 4 females and 2 males) to identify and resolve any problems with our experimental setup. Subsequently, we recruited 24 participants for the main study, including 11 males and 13 females of ages ranging from 18 to 52.

Moreover, given that patients who carry IMDs are often seniors [56], we also conducted a co-design workshop with 2 senior individuals who had intimate knowledge and experience with pacemakers: (1) a 74-year-old female cardiology doctor and (2) a 79-year-old male pacemaker patient.

Experiment Procedure

In total, 2 essential vibration settings, frequency, and duration, were manipulated to measure the effect on pairing performance. Based on experiences gained from our pilot study, we set vibration motor frequencies to 50 Hz, 75 Hz, and 100 Hz, and vibration durations to 400 ms, 700 ms, and 1000 ms. The 9 frequency–duration combinations enabled successful pairing and avoided excessive participant workload.

During the user study, participants were instructed to wear our prototype and sit on a chair. Then they need to grasp the external device simulator and repeatedly attach it to the black pocket area of the chest strap, as shown in Figure 6D. They were advised to attach the device in a random manner (such as to random positions), and (in each cycle) stay attached until the vibration had completely ceased. Before starting the data collection, participants were asked to acquaint themselves with the prototype to understand the pairing process. This introductory process took under a minute for all participants. Subsequently, for each of the 9 vibration conditions, participants were asked to conduct the attachment for 5 consecutive cycles as one run and complete 4 such runs in total. The order in which participants used different vibration frequencies was counterbalanced.

At the end of the user study, participants were requested to fill out a standard system usability scale (SUS) questionnaire [57] to assess the usability of the pairing method. We then conducted an interview with them to gather further insights. Full details of the questionnaire and interview are given in Multimedia Appendix 1.

During the co-design workshop, we asked the two senior participants to try our prototype for only 6 runs (considering their physical conditions) and provide their opinions and advice.

Evaluation Metrics

Our study focuses on certain metrics to evaluate the pairing performance.

Accuracy

The accuracy of a pairing system is typically measured by false rejection rate (FRR) and false acceptance rate (FAR) [43,58,59]. FRR is the frequency at which the pairing between legitimate devices is incorrectly rejected. FAR indicates the frequency that a pair of illegitimate devices (such as the IMD and a malicious external device) is mistakenly authorized and gauges the resilience of pairing against impersonation attacks. A high FRR and FAR could lead to poor usability and security, respectively. These 2 metrics are calculated as follows:

$$\text{FRR} = \frac{\text{Number of rejected pairings between legitimate devices}}{\text{All pairing attempts between legitimate devices}}$$

$$\text{FAR} = \frac{\text{Number of successful pairings between illegitimate devices}}{\text{All pairing attempts between illegitimate devices}}$$

During the pairing process, there is often a mismatch (denoted by d) between the readings of the IMD and the external device due to inherent noises. As aforementioned, we use a fuzzy extractor scheme to correct the mismatch. At the core of this method is the selection of a threshold (denoted by Thr): the mismatch can be rectified (and thus the pairing is accepted) if $d \leq \text{Thr}$; otherwise, the pairing is rejected. As such, one can balance FRR and FAR by adjusting Thr. Because security is of utmost importance for the IMDs, we set a smaller Thr to ensure FAR=0 and use the corresponding lowest FRR to represent accuracy.

Security

The FAR metric evaluates the system's security against impersonation attacks. The resilience against brute-force attacks is determined by the randomness level of the attachment motions, which can be measured in two primary ways: (1) By the National Institute of Standards and Technology (NIST) statistical test suite [60] that provides a comprehensive randomness assessment of a random number generator, a method widely recognized within the cybersecurity community [19,31,43]. (2) By measuring Shannon entropy, which quantifies the amount of information contained in each motion event [17,31,61,62].

Usability

Usability is assessed based on the results from our SUS questionnaires and interviews.

Ethical Considerations

This study involved human participants and underwent thorough ethical review, particularly given the potential involvement of older participants. Ethics approval was obtained from the relevant institutions prior to participant recruitment and user study, in accordance with institutional regulations (the University of Melbourne: approved by the Human Ethics Committee, application number: 2022-24851-31088-3; the University of Birmingham: approved by the Science,

Technology, Engineering and Mathematics Ethics Committee, application number: ERN_2022 - 0255).

Participants were recruited via online advertisements and were offered US $30 for their time. All participants provided informed consent prior to participation. The data collected during the user study were specifically processed to ensure anonymity and untraceability of identity and were securely stored in the University of Melbourne's data center. All participant data were anonymized by removing personally identifiable information before analysis, and participants were assigned unique identification codes to ensure confidentiality. The entire user study process was overseen by a departmental delegate of the university's ethics committee, with all study details reported to them on a weekly basis.

Results

Performance of the Pairing Technique

Figure 7 shows the distribution of all peak locations (ie, the secret) collected by the IMD from 24 participants. We observe that for a specific vibration frequency, such as 50 Hz, the peak locations range between 30 and 70 Hz and generally approximate a normal distribution centered by the motor's frequency, suggesting a certain degree of randomness from the user. Additionally, it appears that the distribution is slightly flatter (thereby the level of randomness increases) with an increase in vibration frequency. Notably, the possible options for peak locations in the frequency domain are not continuous due to the sample-based nature of the time domain acceleration data.

Figure 7. Distribution of peak location measured by the IMD among 24 participants. The black dashed lines indicate frequencies of the vibration motor. IMD: implantable medical device.

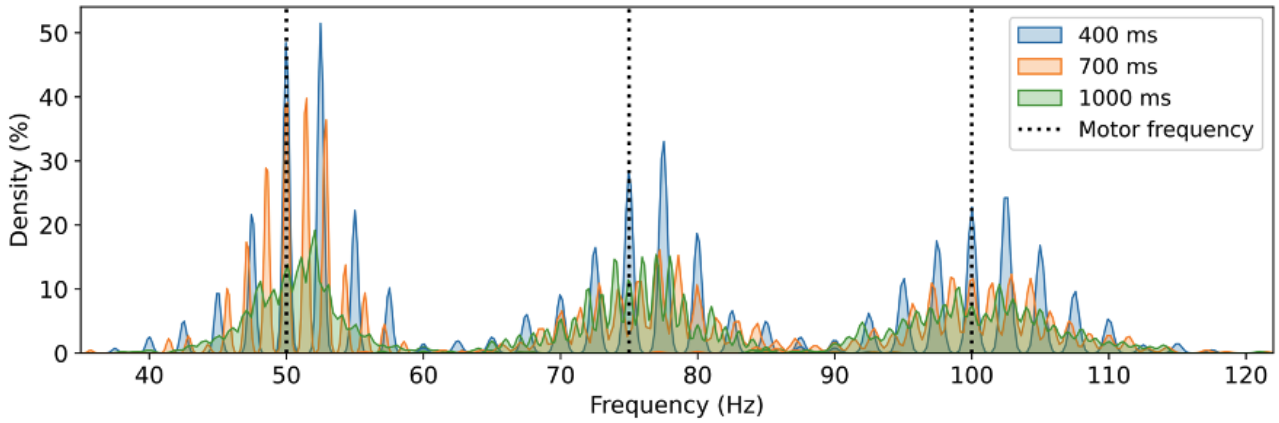

Mismatch is calculated by subtracting peak location values between the IMD and the external device and represents the level of noise and error. The mismatch distribution for our prototype, as illustrated in Figure 8A, resembles a normal distribution centered around a mean near zero and with a standard deviation of 2.8 Hz. This implies that user-induced errors and sensor noise are limited. Note that this result considers situations where participants did not strictly follow our pairing norms during the study. For instance, there were a number of occasions when participants released the external device while it was still vibrating. Such cases were not excluded from our dataset as they present a more realistic use scenario; otherwise, we expect that the mismatch levels would be even lower. On the other hand, Figure 8B and C show that the degree of mismatch does not have a straightforward correlation with either the vibration frequency or the duration.

Figure 8. Mismatch between the IMD and the external device. (A) Mismatch of all data among participants. (B) Mismatch with vibration frequency. (C) Mismatch with vibration time. IMD: implantable medical device.

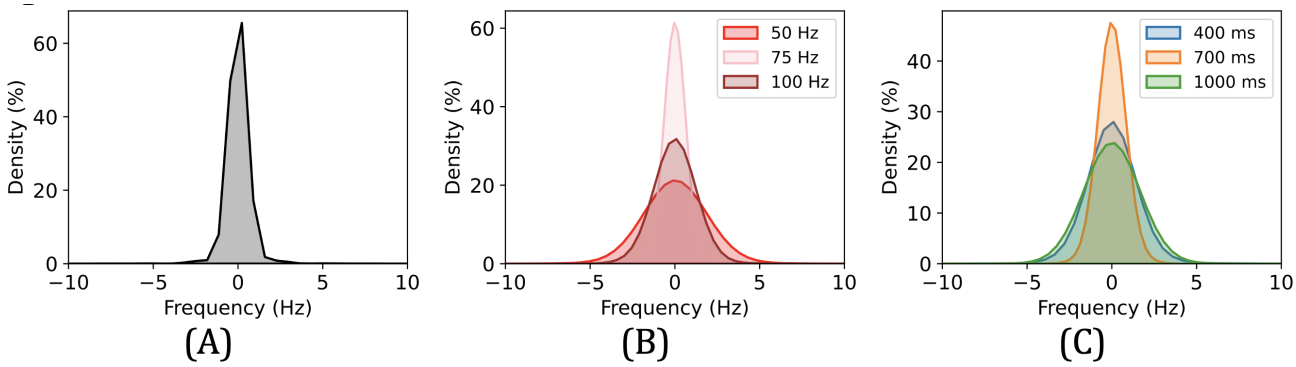

Experimental Evaluation

Accuracy Assessment

For each of the 9 vibration conditions, we build two sets to measure accuracy:

Set I comprises 96 (=24 × 4) pairs of peak locations, each with a length of 5 (since we collected 5 cycles per run). All the pairs in Set I come from legitimate pairings of an IMD and an external device. This set calculates the FRR metric as aforementioned.

Set II has 96 pairs of peak locations (the same size as Set I), where each pair is created by randomly mixing data from illegitimate device pairings. This set calculates the FAR metric as aforementioned.

An effective pairing technique should maximize the acceptance of pairs from Set I (ie, low FRR), while minimizing the acceptance of pairs from Set II (ie, low FAR). Note that not all five motions are necessarily needed, ie, we can vary the length of runs ranging from 1 to 5, by truncating the initial elements.

The following figures show the accuracy of our prototype across various numbers of attachment motions performed. FAR is 0 in all cases, and we consider that an FRR below 5% signifies good usability [43,61]. As expected, increasing the number of motions consistently improves the accuracy of the pairing. Moreover, given a specific vibration frequency, longer vibration duration leads to higher accuracy, which will be further discussed in the coming sections. An additional observation is that with a fixed vibration duration and number of motions, the FRR tends to drop as the vibration frequency rises.

Overall, the red circles in the above figures indicate the 5 out of 9 vibration conditions that offer acceptable accuracy levels (with FAR=0 and FRR <5%). For example, a vibration condition of 50 Hz for 1000 ms per cycle requires the user to execute five attachments to achieve pairing with FAR=0 and FRR=3.7% (see Figure 9A). Note that for other vibration conditions, more than five motions are likely to also yield satisfactory accuracy. However, this would demand more effort from the user, which could harm usability and even safety in emergencies.

Figure 9. FRR versus number of attachments under different vibration frequencies: (A) 50 Hz, (B) 75 Hz, and (C) 100 Hz. FRR: false rejection rate.

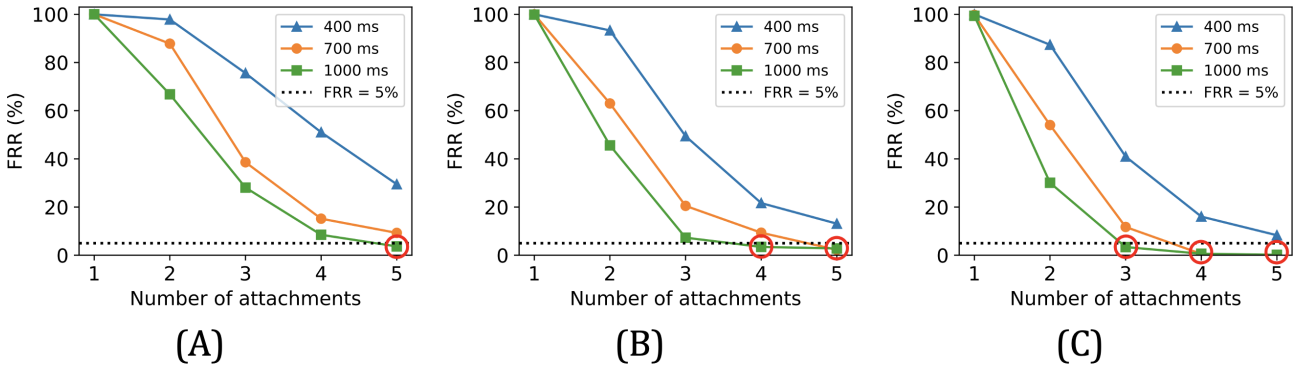

Security Assessment

We refer to previous work [19,31,43] to assess the randomness of the secret generated by our technique: For each of the vibration conditions, we take the floor of the (fractional) entropy value for that specific setting (refer to Table 2) and extract that number of least significant bits from each peak location value. Subsequently, we combine these bitstrings from all vibration conditions (following the order in our user study) as a single 8.6 kbits string and evaluate its randomness using the NIST statistical test suite [60]. The full results are given in Table 3. The outputs of the NIST tests are *P* values that represent the probability the data is generated by an eligible random number generator. If a *P* value is smaller than a threshold (usually .01 [19,31,43]), the randomness hypothesis is rejected. Table 3 shows that all *P* values are larger than .01 and hence pass the NIST tests.

Table . Entropy of each attachment motion (unit is bit).

	50 Hz	75 Hz	100 Hz
400 ms	2.61	3.12	3.87
700 ms	3.03	3.86	4.15
1000 ms	3.15	4.01	4.48

Table . NIST statistical test results for attachment motions.

Test	*P* value	Test	*P* value
Frequency	.88	Block frequency	.14
Runs	.11	Longest runs	.10
Binary matrix rank	.17	FFT[a]	.62
Non-overlap template	.16	Overlapping template	.38
Serial (*P* value$_1$)	.64	Linear complexity	.72
Serial (*P* value$_2$)	.68	Approximate entropy	.18
Cumulative sums (forward)	.19	Random excursions	.22
Cumulative sums (reverse)	.26	Random excursions var.	.40

[a]FFT: fast Fourier transform.

Table 2 shows the entropy value contained in each motion across different vibration conditions. Overall, a single motion in our study carries an entropy from 2.61 to 4.48 bits. For a certain vibration frequency, the entropy grows with higher vibration durations. This is because extended measurements yield larger sample size and frequency resolution, enabling more possible peak locations and thus higher entropy. Furthermore, for a given vibration duration, the entropy value rises with an increase in vibration frequency. We leave the study of this phenomenon to future work. Nevertheless, the choice of vibration frequency is often limited by the capability of the motor and accelerometer in practice.

It is noteworthy that some entropy is sacrificed when rectifying mismatches between the 2 devices. Here, we make a preliminary estimation of the entropy loss: Using the encoding method in [43] on our dataset, the maximum bit mismatch rates (ie, percentage of different bits between two devices) for our prototype vary between 0.7% and 3.0% for different vibration conditions. This can be addressed by a fuzzy extractor with (31, 29) Reed-Solomon code that has a 3.23% error tolerance [11,63], potentially leading to an entropy loss of 6.5%.

Usability Assessment

The average SUS score for our pairing technique is 73.6 (SD 18.14), which generally passes the typical benchmark value of 68 for “good usability” [57]. It is important to note that the SUS questionnaires were completed after an extensive data collection process including a repetition of 180 attachment motions. We expect that users carrying out a more realistic task would report even higher usability scores.

We gained further insights into usability from the interviews. Over half of the participants (15 out of 24) explicitly indicated that our technique was easy to use. For example, one participant (p8) commented, “The attachment doesn’t require me to think. This is an advantage. I don’t know what is happening here, but I prefer it as it requires less effort,” and another participant (p13) remarked, “It’s easy. You don’t really have to move that much, and you can do it while you’re sitting as well.” Some participants expressed their preference for the vibrational feedback. One participant (p1) said, “The vibration is good feedback, and I don’t have to visually see anything,” and another participant (p22) noted, “The process is like listen to my heart.” In addition, some participants conveyed that they found the pairing process to be enjoyable and fun. For example, 3 participants described the vibration as a hand massage and 2 compared the pairing activity to using a stethoscope.

Most participants (18 out of 24) experienced no discomfort during the study. Nonetheless, the rest of the 6 people did report some discomfort at the end of the study. In total, 4 participants noted that the intensity of the vibrations was excessive; for example, one participant (p4) stated, “I feel like my entire chest is vibrating, and I don’t like the feeling.” This concern might be resolved by selecting a vibration motor with lower amplitude. In addition, 4 participants reported feeling fatigued after the data collection process, but also noted this was due to the repetition of 180 attachments and that less motions will alleviate this issue. Furthermore, one participant (p3) criticized the prototype design and mentioned that the external device simulator was too big. We leave the refinement of our prototype as future work.

Valuable insights were also gathered from the co-design workshop. Both participants initially found the vibration-based pairing technique interesting and somewhat surprising, but they quickly became accustomed to it and could easily complete the remaining required motions. They both explicitly noted that the pairing operations were easy to learn and perform. The cardiology doctor described the pairing operation as “using a stethoscope” and confirmed that the vibration signal in the experiment would pose minimal risks to patients with IMDs. Both participants also appreciated the tactile feedback from the vibrations. The doctor commented, “The vibration tells you if you’re on track,” while the pacemaker patient added, “The vibration encourages me towards the end of pairing.” However, both participants pointed out that the prototype used in the study was bulky and heavy—an improvement we leave for future work. Overall, both participants found the pairing experience acceptable and expressed willingness to use it in real-world scenarios if required.

Optimal Setups

Based on our analysis so far, we summarize all pairing configurations that (1) exhibit high accuracy with zero FAR and FRR under 5%, and (2) generate a level of entropy surpassing a standard four-digit PIN code (with an entropy of

13.3 bits), which is commonly used in pairing of Bluetooth technologies and other security systems [8]. All viable settings that meet these requirements (with minimum required number of motions) are shown in Table 4. Note that the time values include both the vibration duration and an additional "preparation time" necessary for a user to detach and then reattach the external device to their body; in our study, this interval was 0.5 seconds.

In summary, we find that with a vibration configuration set at 100 Hz and 700 ms, a user can carry out 4 attachment motions to enable the exchange of a secret with (FAR, FRR)=(0, 0.6%) and entropy of 15.5 bits. This process can be completed in a mere 4.8 seconds.

Table . Summary of well-performing pairing configurations.

Vibration condition	Motion, n	FAR[a], FRR[b] (%)	Entropy	Time (s)
50 Hz, 1000 ms	5	0, 3.7	14.7	7.5
75 Hz, 700 ms	5	0, 2.2	18.0	6
75 Hz, 1000 ms	4	0, 3.5	15.0	6
100 Hz, 700 ms	4	0, 0.6	15.5	4.8
100 Hz, 1000 ms	4	0, 0.6	16.8	6

[a]FAR: false acceptance rate.

[b]FRR: false rejection rate.

Discussion

Principal Findings

Our work introduces a new and reliable vibration-based pairing approach for IMDs, which only requires a low sampling rate accelerometer and relies on the natural randomness inherent in human behavior. We empirically validate the feasibility of our technique through a user study. Overall, we find that the workload required to bootstrap a secure pairing is minimal, and we estimate that it requires the user to attach a device to the body only 4 times in roughly 5 s. With an FAR of 0 and an FRR of 0.6%, the risk posed by adversaries is low, and legitimate users will likely experience very few failures.

As mentioned in the related work section, the use of a PAKE eliminates offline brute-force attacks. In addition, it also restricts the number of online MITM attempts. Typically, the adversary has a very limited period to obtain the secret and usually only one chance for a MITM attack [44]. As an estimate, 4 motions with 15.5 bits entropy reduce the adversary's success probability on online brute-force attacks to 0.002% [42] (assuming the adversary is limited to guessing only). Therefore, we believe these motions serve as adequate input for a PAKE. If needed, higher entropy can be easily achieved by performing more motions.

Our user study confirmed the high usability of our pairing method. Participants found it straightforward to understand, learn, and perform. The process of attaching the device is very intuitive, like using a stethoscope as described by the participants. Our technique also brings about certain entertainment to users, being both relaxing and enjoyable (such as described as hand massage). This could be advantageous in certain therapeutic treatments, where physical interaction can enhance memory, concentration, and mental health [64]. Moreover, it is worth noting that for patients who are unable (eg, due to disabilities or unconsciousness in emergencies) or unwilling to execute the motions, our pairing allows medical practitioners or caregivers (who have received appropriate training) to execute the motions on the patient's body on their behalf.

Our proposed method only requires an accelerometer, a component already present in the latest generation IMDs [23-25]. The signal processing and other cryptographic algorithms for the IMD are computationally lightweight and work efficiently on 32-bit Cortex-M microcontrollers, which closely resemble IMDs' capabilities [11,43,53]. Our approach solely depends on vibration at a constant frequency, which can be easily implemented on readily available consumer devices such as smartphones and tablets. This is beneficial considering that medical device companies already equip the IMDs with the ability to connect to personal mobile devices [65]. Moreover, while our work assumes that the IMD is a pacemaker, we argue that the technique can be easily transferred to other types of IMDs or even external wearables. Furthermore, our proposed pairing technique incurs minimal costs. In our prototype implementation, the combined cost of the vibration motor and accelerometer was under $30, and this cost could be further reduced during mass production.

Comparison With Prior Vibration-Based Work

Our pairing technique significantly relaxes the demands on the IMD's sampling capability. We use an accelerometer operating at 250 Hz, in contrast to previous work that often relies on sampling rates of several thousand Hz or more. In particular, the sampling rate can be further decreased by using lower vibration frequencies. For example, with a 50 Hz vibration, the frequency domain peaks cluster between 30 and 70 Hz (see Figure 7), indicating that an accelerometer with a 140 Hz maximum is adequate.

Conventional approaches typically try to avoid user-generated noise. For instance, the user needs to ensure stable contact between devices during data transmission. Conversely, our method harnesses user noise and benefits from it as a source of entropy. Indeed, our dataset includes many instances with significant user error, like when a participant releases the external device before the vibration completely stops. In such

scenarios, the IMD only captures a portion of the vibration within its measurement window. Despite this, our technique maintains high reliability.

Furthermore, previous work that encodes secrets into vibrations often demands precise time synchronization in milliseconds between devices, which itself is a challenging task for resource-constrained devices [66]. In contrast, our approach allows for more lenient synchronization—as long as the two devices capture similar vibration signals within most of their measurement windows, the peak locations effectively match. This aspect greatly enhances the feasibility of our technique for IMDs.

Notably, our data throughput is significantly lower than [26,27,29,32] and is comparable with [31,33]. Considering the scenario of transmitting a 4-digit PIN code for use in a PAKE, previous work [26,27,29,32] only needs 0.0004 to 0.665 s, which is much faster than the 4.8 seconds required by our method. However, this rapid transmission, while advantageous in many daily applications, may not be suitable for IMD pairing contexts, where the vibration serves not only for secret exchange but also as a crucial cue for patients to be aware of the pairing process. In contrast, we argue that a duration of 4.8 s strikes a balance: it is long enough to be noticeable, yet short enough to maintain usability and safety in emergencies.

Considerations of Health Implications With Vibrations

Our proposed pairing technique incorporates vibration, a feature that naturally raises concerns regarding the potential long-term health impacts on patients. However, current research indicates that only long-term and excessive exposure to vibrations is linked to adverse effects on mental and physical health [67,68]. In contrast, our method involves brief vibrational interactions, which last less than 5 seconds and may not occur every day. This limited exposure could reduce the likelihood of the negative health consequences.

Resilience to Acoustic Eavesdropping Attacks

Vibration is essentially a low-frequency audio signal, which inevitably emits acoustic side-channel information that might be eavesdropped using a microphone. This is particularly threatening for methods that encode secrets within vibration signals. For example, Halevi and Saxena [69] found that secrets transmitted this way could be severely compromised using an off-the-shelf microphone from a few meters away. To mitigate this, Kim et al [26] and Anand and Saxena [70,71] proposed using Gaussian white noise or masking signals to obscure the acoustic leaks. These approaches have shown promise in reducing side-channel vulnerabilities against advanced eavesdropping attacks.

In comparison, as shown in [31], the risks associated with eavesdropping are significantly reduced when the vibration is not the carrier of the secret. Our research aligns with this guideline, using a constant vibration signal across sessions to minimize acoustic leakage. In addition, existing countermeasures [26,70,71] are also applicable to our method.

Limitations

Our work has certain limitations. Our experiments did not explicitly recruit participants who were IMD patients (mainly due to ethics constraints of the institutions where the user study was conducted). Further validation of our approach with these patient groups is necessary.

We designed our prototype in line with previous work in the IMD security community [5,26,40]. However, there is room for enhancement, particularly in its size and weight. Future research should develop more skin-conformable and miniaturized prototypes.

Another aspect of future work is to empirically evaluate the susceptibility of our pairing technique against microphone-based eavesdropping attacks at a distance.

Conclusion

In this paper, we explore the potential of leveraging vibration to pair with an IMD. We propose a novel technique that uses a straightforward constant-frequency vibration to extract secrets from natural and random human motor behavior for device pairing. We implement and validate our technique through a user study. Overall, we show that it is feasible to establish a cryptographic key in 5 s with high usability, based only on standard vibration motors and accelerometers with low sampling capabilities. The ubiquity of accelerometers in today's commercial smart devices and IMDs maximizes the chance of acceptance of our design. In general, we hope that our work will serve as a reference for pairing with resource-constrained devices using vibrations in body area networks.

Acknowledgments

MZ is funded by the Priestley PhD Scholarship program organized by the University of Melbourne and University of Birmingham.

Data Availability

The data collected from the user study and the software used in our prototype are publicly available at GitHub [72]. All data have been anonymized in accordance with the requirements of the institutional ethics committees to protect participant privacy. Additional supporting documentations are included in the repository to facilitate reuse.

Conflicts of Interest

None declared.

Multimedia Appendix 1
Questionnaire and interview design.
[DOCX File, 13 KB - biomedeng_v10i1e57091_app1.docx]

References

1. Global number of pacemakers in 2016 and a forecast for 2023. Statista. 2022. URL: https://www.statista.com/statistics/800794/pacemakers [accessed 2025-08-18]
2. Halperin D, Heydt-Benjamin TS, Fu K, Kohno T, Maisel WH. Security and privacy for implantable medical devices. IEEE Pervasive Comput 2008;7(1):30-39. [doi: 10.1109/MPRV.2008.16]
3. Marin E, Singelée D, Garcia FD, Chothia T, Willems R, Preneel B. On the (in)security of the latest generation implantable cardiac defibrillators and how to secure them. Presented at: ACSAC '16: 2016 Annual Computer Security Applications Conference; Dec 5-8, 2016; Los Angeles, California, USA. [doi: 10.1145/2991079.2991094]
4. Marin E, Singelée D, Yang B, Verbauwhede I, Preneel B. On the feasibility of cryptography for a wireless insulin pump system. Presented at: CODASPY'16: Sixth ACM Conference on Data and Application Security and Privacy; Mar 9-11, 2016; New Orleans, Louisiana, USA. [doi: 10.1145/2857705.2857746]
5. Marin E, Singelée D, Yang B, et al. Securing wireless neurostimulators. Presented at: CODASPY '18: Eighth ACM Conference on Data and Application Security and Privacy; Mar 19-21, 2018; Tempe, AZ, USA. [doi: 10.1145/3176258.3176310]
6. Reverberi L, Oswald D. Breaking (and fixing) a widely used continuous glucose monitoring system. Presented at: 11th USENIX Workshop on Offensive Technologies; Aug 14-15, 2017; Vancouver, Canada.
7. Daemen J, Rijmen V. AES proposal: Rijndael. CMU School of Computer Science. 1999. URL: https://www.cs.cmu.edu/afs/cs/project/pscico-guyb/realworld/www/docs/rijndael.pdf [accessed 2025-08-18]
8. Bisdikian C. An overview of the Bluetooth wireless technology. IEEE Commun Mag 2001;39(12):86-94. [doi: 10.1109/35.968817]
9. Rocha EA, Cunha GS, Tavares AB, et al. Syncope in patients with cardiac pacemakers. Braz J Cardiovasc Surg 2021 Feb 1;36(1):18-24. [doi: 10.21470/1678-9741-2020-0076] [Medline: 33594860]
10. Adams C, Lloyd S. Understanding PKI: Concepts, Standards, and Deployment Considerations: Addison-Wesley Professional; 2003.
11. Zhang M, Marin E, Oswald D, Singelée D. FuzzyKey: comparing fuzzy cryptographic primitives on resource-constrained devices. In: Grosso V, Pöppelmann T, editors. In Smart Card Research and Advanced Applications: Springer International Publishing; 2022:289-309.
12. Rushanan M, Rubin AD, Kune DF, Swanson CM. SoK: security and privacy in implantable medical devices and body area networks. In: 2014 IEEE Symposium on Security and Privacy (SP): IEEE; 2014:524-539. [doi: 10.1109/SP.2014.40]
13. Rasmussen KB, Castelluccia C, Heydt-Benjamin TS, Capkun S. Proximity-based access control for implantable medical devices. Presented at: CCS '09; Nov 9-13, 2009; Chicago, Illinois, USA. [doi: 10.1145/1653662.1653712]
14. Tomlinson WJ, Banou S, Yu C, Nogueira M, Chowdhury KR. Secure on-skin biometric signal transmission using galvanic coupling. In: IEEE INFOCOM 2019 - IEEE Conference on Computer Communications: IEEE; 2019:1135-1143. [doi: 10.1109/INFOCOM.2019.8737540]
15. Denning T, Fu K, Kohno.2008 T. Absence makes the heart grow fonder: new directions for implantable medical device security. Presented at: HOTSEC'08: Proceedings of the 3rd conference on Hot topics in security; Jul 29, 2008; San Jose, CA, USA.
16. Gollakota S, Hassanieh H, Ransford B, Katabi D, Fu K. They can hear your heartbeats: non-invasive security for implantable medical devices. In: Proceedings of the ACM SIGCOMM 2011 Conference: Association for Computing Machinery; 2011:2-13. [doi: 10.1145/2018436.2018438]
17. Lin Q, Xu W, Liu J, et al. H2B: heartbeat-based secret key generation using piezo vibration sensors. In: Proceedings of the 18th International Conference on Information Processing in Sensor Networks: Association for Computing Machinery; 2019:265-276. [doi: 10.1145/3302506.3310406]
18. Poon CCY. A novel biometrics method to secure wireless body area sensor networks for telemedicine and m-health. IEEE Commun Mag 2006;44(4):73-81. [doi: 10.1109/MCOM.2006.1632652]
19. Rostami M, Juels A, Koushanfar F. Heart-to-heart (H2H): authentication for implanted medical devices. In: Proceedings of Conference on Computer and Communications Security: Association for Computing Machinery; 2013:1099-1112. [doi: 10.1145/2508859.2516658]
20. Marin E, Argones Rúa E, Singelée D, Preneel B. On the difficulty of using patient's physiological signals in cryptographic protocols. In: Proceedings of the 24th ACM Symposium on Access Control Models and Technologies: Association for Computing Machinery; 2019:113-122. [doi: 10.1145/3322431.3325099]
21. Dierks T, Allen C. The TLS protocol version 1.0. : The Internet Society; 1999.
22. Ryu J. Psychophysical model for vibrotactile rendering in mobile devices. Presence (Camb) 2010:364-387. [doi: 10.1162/PRES_a_00011]

23. Rate response feature. Medtronic. 2016. URL: https://www.medtronicacademy.com/features/rate-response-rr-feature [accessed 2025-08-18]
24. Pacing & defibrillation. Cardiocases. URL: https://www.cardiocases.com/en/pacingdefibrillation [accessed 2025-08-18]
25. Puppala VK, Hofeld BC, Anger A, et al. Pacemaker detected active minutes are superior to pedometer-based step counts in measuring the response to physical activity counseling in sedentary older adults. BMC Geriatr 2020 May 6;20(1):162. [doi: 10.1186/s12877-020-01559-y] [Medline: 32375676]
26. Kim Y, Lee WS, Raghunathan V, Jha NK, Raghunathan A. Vibration-based secure side channel for medical devices. In: Proceedings of the 52nd Annual Design Automation Conference: Association for Computing Machinery; 2015:1-6. [doi: 10.1145/2744769.2744928]
27. Lee K, Raghunathan V, Raghunathan A, Kim Y. SYNCVIBE: fast and secure device pairing through physical vibration on commodity smartphones. In: 2018 IEEE 36th International Conference on Computer Design (ICCD: IEEE; 2018:234-241. [doi: 10.1109/ICCD.2018.00043]
28. Roy N, Choudhury RR. Ripple {II}: faster communication through physical vibration. Presented at: 13th USENIX Symposium on Networked Systems Design and Implementation; Apr 2-5, 2013; Lombard, IL, USA.
29. Roy N, Gowda M, Choudhury RR. Ripple: communicating through physical vibration. Presented at: 12th USENIX Symposium on Networked Systems Design and Implementation; Apr 25-27, 2012; San Jose.
30. Saxena N, Uddin MB, Voris J. Treat'em like other devices: user authentication of multiple personal RFID tags. In: SOUPS 2009, Vol. 9:1-1. [doi: 10.1145/1572532.1572573]
31. Wang W, Yang L, Zhang Q. Resonance-Based Secure Pairing for Wearables. IEEE Trans on Mobile Comput 2018;17(11):2607-2618. [doi: 10.1109/TMC.2018.2809736]
32. Xiao R, Mayer S, Harrison C. VibroComm: using commodity gyroscopes for vibroacoustic data reception. Presented at: MobileHCI '20; Oct 5-8, 2020; Oldenburg, Germany. [doi: 10.1145/3379503.3403540]
33. Saxena N, Uddin MB, Voris J, Asokan N. Vibrate-to-unlock: mobile phone assisted user authentication to multiple personal RFID tags. In: 2011 IEEE International Conference on Pervasive Computing and Communications (PerCom): IEEE; 2011:181-188. [doi: 10.1109/PERCOM.2011.5767583]
34. de Vaal MH, Neville J, Scherman J, Zilla P, Litow M, Franz T. The in vivo assessment of mechanical loadings on pectoral pacemaker implants. J Biomech 2010 Jun 18;43(9):1717-1722. [doi: 10.1016/j.jbiomech.2010.02.028] [Medline: 20202638]
35. Stenerson M, Cameron F, Payne SR, et al. The impact of accelerometer use in exercise-associated hypoglycemia prevention in type 1 diabetes. J Diabetes Sci Technol 2015 Jan;9(1):80-85. [doi: 10.1177/1932296814551045] [Medline: 25231116]
36. Stenerson M, Cameron F, Wilson DM, et al. The impact of accelerometer and heart rate data on hypoglycemia mitigation in type 1 diabetes. J Diabetes Sci Technol 2014 Jan;8(1):64-69. [doi: 10.1177/1932296813516208]
37. Khan A, Hammerla N, Mellor S, Plötz T. Optimising sampling rates for accelerometer-based human activity recognition. Pattern Recognit Lett 2016 Apr;73:33-40. [doi: 10.1016/j.patrec.2016.01.001]
38. Adewusi SA, Rakheja S, Marcotte P, Boutin J. Vibration transmissibility characteristics of the human hand–arm system under different postures, hand forces and excitation levels. J Sound Vib 2010 Jul;329(14):2953-2971. [doi: 10.1016/j.jsv.2010.02.001]
39. Adewusi S, Thomas M, Vu VH, Li W. Modal parameters of the human hand-arm using finite element and operational modal analysis. Mechanics & Industry 2014;15(6):541-549. [doi: 10.1051/meca/2014060]
40. Halperin D, Heydt-Benjamin TS, Ransford B, et al. Pacemakers and implantable cardiac defibrillators: software radio attacks and zero-power defenses. 2008 Presented at: 2008 IEEE Symposium on Security and Privacy p. 129-142.
41. Schechter S. Security that is meant to be skin deep: using ultraviolet micropigmentation to store emergency-access keys for implantable medical devices. Presented at: 1st USENIX Workshop on Health Security and Privacy; Aug 10, 2010; Washington, DC.
42. Katz J, Ostrovsky R, Yung M. Forward secrecy in password-only key exchange protocols. In: International Conference on Security in Communication Networks: Springer; 2002:29-44. [doi: 10.1007/3-540-36413-7_3]
43. Li X, Zeng Q, Luo L, Luo T. T2Pair: secure and usable pairing for heterogeneous iot devices. In: Proceedings of the 2020 ACM SIGSAC Conference on Computer and Communications Security: Association for Computing Machinery; 2020:309-323. [doi: 10.1145/3372297.3417286]
44. Bellovin SM, Merritt M. Encrypted key exchange: password-based protocols secure against dictionary attacks. Presented at: CCS93: 1st ACM Conference on Communications and Computing Security; Nov 3-5, 1993; Fairfax, Virginia, USA. [doi: 10.1145/168588.168618]
45. Han J, Chung AJ, Sinha MK, et al. Do you feel what i hear? Enabling autonomous iot device pairing using different sensor types. In: 2018 IEEE Symposium on Security and Privacy (SP): IEEE; 2018:836-852. [doi: 10.1109/SP.2018.00041]
46. Introduction. CMSIS. 2022. URL: https://www.keil.com/pack/doc/CMSIS/DSP/html/group RealFFT.html [accessed 2025-08-18]
47. Zhang L, Pathak PH, Wu M, Zhao Y, Mohapatra P. Accelword: energy efficient hotword detection through accelerometer. Presented at: MobiSys'15: The 13th Annual International Conference on Mobile Systems, Applications, and Services; May 18-22, 2015; Florence Italy. [doi: 10.1145/2742647.2742658]
48. Doran RW. The gray code. J Univers Comput Sci 2007 [FREE Full text]

49. Dodis Y, Ostrovsky R, Reyzin L, Smith A. Fuzzy extractors: how to generate strong keys from biometrics and other noisy data. SIAM J Comput 2008 Jan;38(1):97-139. [doi: 10.1137/060651380]
50. Xu F, Qin Z, Tan CC, Wang B, Li Q. IMDGuard: securing implantable medical devices with the external wearable guardian. Presented at: IEEE Annual Joint Conference: INFOCOM, IEEE Computer and Communications Societies; Apr 10-15, 2011; Shanghai, China.
51. Dolev D, Yao A. On the security of public key protocols. IEEE Trans Inform Theory 1983 Mar;29(2):198-208. [doi: 10.1109/TIT.1983.1056650]
52. MPU-6000 and MPU-6050 product specification revision 34. Adafruit. 2013. URL: https://cdn-learn.adafruit.com/downloads/pdf/mpu6050-6-axis-accelerometer-and-gyro.pdf [accessed 2025-08-18]
53. Azure pacing system. Medtronic. 2022. URL: https://europe.medtronic.com/xd-en/healthcare-professionals/products/cardiac-rhythm/pacemakers/azure.html [accessed 2025-08-18]
54. Model no307-103 vibration motor. Precision Microdrives. 2021. URL: https://catalogue.precisionmicrodrives.com/product/datasheet/307-103-9mm-vibration-motor-25mm-type-datasheet.pdf [accessed 2025-08-18]
55. Petronio AS, Sinning JM, Van Mieghem N, et al. Optimal implantation depth and adherence to guidelines on permanent pacing to improve the results of transcatheter aortic valve replacement with the Medtronic CoreValve System: The CoreValve Prospective, International, Post-Market ADVANCE-II Study. JACC Cardiovasc Interv 2015 May;8(6):837-846. [doi: 10.1016/j.jcin.2015.02.005] [Medline: 25999108]
56. Lim WY, Prabhu S, Schilling RJ. Implantable cardiac electronic devices in the elderly population. Arrhythm Electrophysiol Rev 2019 May 2;8(2):143-146. [doi: 10.15420/aer.2019.3.4]
57. Lewis JR. The System Usability Scale: past, present, and future. International Journal of Human–Computer Interaction 2018 Jul 3;34(7):577-590. [doi: 10.1080/10447318.2018.1455307]
58. Ahmed I, Ye Y, Bhattacharya S, et al. Checksum gestures: continuous gestures as an out-of-band channel for secure pairing. Presented at: UbiComp '15: The 2015 ACM International Joint Conference on Pervasive and Ubiquitous Computing; Sep 7-11, 2015; Osaka, Japan. [doi: 10.1145/2750858.2807521]
59. Li X, Yan F, Zuo F, Zeng Q, Luo L. Touch well before use: intuitive and secure authentication for iot devices. Presented at: MobiCom '19: The 25th Annual International Conference on Mobile Computing and Networking; Oct 21-25, 2019; Los Cabos, Mexico. [doi: 10.1145/3300061.3345434]
60. Rukhin A, Soto J, Nechvatal J, et al. A statistical test suite for random and pseudorandom number generators for cryptographic applications. : NIST; 2001.
61. Mayrhofer R, Gellersen H. Shake well before use: intuitive and secure pairing of mobile devices. IEEE Trans on Mobile Comput 2009;8(6):792-806. [doi: 10.1109/TMC.2009.51]
62. Thomas M, Joy AT. Elements of Information Theory: Wiley-Interscience; 2006.
63. Lin S, Costello DJ. Error Control Coding: Prentice Hall; 2001, Vol. 2.
64. Hedayati M, Sum S, Hosseini SR, Faramarzi M, Pourhadi S. Investigating the effect of physical games on the memory and attention of the elderly in adult day-care centers in Babol and Amol. Clin Interv Aging 2019;14:859-869. [doi: 10.2147/CIA.S196148] [Medline: 31190772]
65. MyCareLink heart mobile app. Medtronic. 2021. URL: https://global.medtronic.com/xg-en/mobileapps/patient-caregiver/cardiac-monitoring/mycarelink-heart-app.html [accessed 2025-08-18]
66. Wang C, Sarsenbayeva Z, Luo C, Goncalves J, Kostakos V. Improving wearable sensor data quality using context markers. Presented at: UbiComp '19: The 2019 ACM International Joint Conference on Pervasive and Ubiquitous Computing; Sep 9-13, 2019; London United Kingdom. [doi: 10.1145/3341162.3349334]
67. Bovenzi M. Health effects of mechanical vibration. G Ital Med Lav Ergon 2005;27(1):58-64. [Medline: 15915675]
68. Seidel H. Selected health risks caused by long‐term, whole‐body vibration. American J Industrial Med 1993 Apr;23(4):589-604. [doi: 10.1002/ajim.4700230407]
69. Halevi T, Saxena N. On pairing constrained wireless devices based on secrecy of auxiliary channels: the case of acoustic eavesdropping. Presented at: CCS '10: 17th ACM Conference on Computer and Communications Security 2010; Oct 4-8, 2010; Chicago, Illinois, USA. [doi: 10.1145/1866307.1866319]
70. Anand SA, Saxena N. Coresident evil: noisy vibrational pairing in the face of co-located acoustic eavesdropping. Presented at: WiSec '17: 10th ACM Conference on Security & Privacy in Wireless and Mobile Networks; Jul 18-20, 2017; Boston, Massachusetts. [doi: 10.1145/3098243.3098256]
71. Anand SA, Saxena N. Noisy vibrational pairing of IoT devices. IEEE Trans Dependable Secure Comput 2018:530-545 [FREE Full text]
72. MrZMN/vibkey. GitHub. URL: https://github.com/MrZMN/VibKey [accessed 2025-08-18]

Abbreviations

FAR: false acceptance rate
FFT: fast Fourier transform
FRR: false rejection rate

IMD: implantable medical device
IoT: Internet of things
MITM: man in the middle
NIST: National Institute of Standards and Technology
OOB: out-of-band
PAKE: password-authenticated key agreement
SUS: system usability scale

Edited by S Rizvi, T Leung; submitted 05.02.24; peer-reviewed by K Daripa, Y Liu; revised version received 09.07.25; accepted 09.07.25; published 26.08.25.

Please cite as:
Zhang M, Wang C, Jiang W, Oswald D, Murray T, Marin E, Wei J, Ryan M, Kostakos V
Using Vibration for Secure Pairing With Implantable Medical Devices: Development and Usability Study
JMIR Biomed Eng 2025;10:e57091
URL: https://biomedeng.jmir.org/2025/1/e57091
doi:10.2196/57091

Estimation of Brachial-Ankle Pulse Wave Velocity With Hierarchical Regression Model From Wrist Photoplethysmography and Electrocardiographic Signals: Method Design

Chih-I Ho[1], MEng; Chia-Hsiang Yen[1], BEng; Yu-Chuan Li[1], MEng; Chiu-Hua Huang[1], MEng; Jia-Wei Guo[1], MEng; Pei-Yun Tsai[2], PhD; Hung-Ju Lin[3], MD, PhD; Tzung-Dau Wang[3], MD, PhD

[1]Department of Electrical Engineering, National Central University, Taoyuan, Taiwan

[2]Graduate School of Advanced Technology, National Taiwan University, Taipei, Taiwan

[3]Cardiovascular Center and Divisions of Cardiology and Hospital Medicine, Department of Internal Medicine, National Taiwan University Hospital, No.7, Chung Shan S Rd, Taipei, Taiwan

Corresponding Author:
Tzung-Dau Wang, MD, PhD
Cardiovascular Center and Divisions of Cardiology and Hospital Medicine, Department of Internal Medicine, National Taiwan University Hospital, No.7, Chung Shan S Rd, Taipei, Taiwan

Abstract

Background: Photoplethysmography (PPG) signals captured by wearable devices can provide vascular age information and support pervasive and long-term monitoring of personal health condition.

Objective: In this study, we aimed to estimate brachial-ankle pulse wave velocity (baPWV) from wrist PPG and electrocardiography (ECG) from smartwatch.

Methods: A total of 914 wrist PPG and ECG sequences and 278 baPWV measurements were collected via the smartwatch from 80 men and 82 women with average age of 63.4 (SD 13.4) and 64.3 (SD 11.6) years. Feature extraction and weighted pulse decomposition were applied to identify morphological characteristics regarding blood volume change and component waves in preprocessed PPG and ECG signals. A systematic strategy of feature combination was performed. The hierarchical regression method based on the random forest for classification and extreme gradient boosting (XGBoost) algorithms for regression was used, which first classified the data into subdivisions. The respective regression model for the subdivision was constructed with an overlapping zone.

Results: By using 914 sets of wrist PPG and ECG signals for baPWV estimation, the hierarchical regression model with 2 subdivisions and an overlapping zone of 400 cm per second achieved root-mean-square error of 145.0 cm per second and 141.4 cm per second for 24 men and 26 women, respectively, which is better than the general XGBoost regression model and the multivariable regression model (all $P<.001$).

Conclusions: We for the first time demonstrated that baPWV could be reliably estimated by the wrist PPG and ECG signals measured by the wearable device. Whether our algorithm could be applied clinically needs further verification.

(JMIR Biomed Eng 2025;10:e58756) doi:10.2196/58756

KEYWORDS

photoplethysmography; PPG; pulse wave velocity; brachial-ankle pulse wave velocity; XGBoost; electrocardiography; signal processing; random forest

Introduction

Cardiovascular disease (CVD) is a major cause of death and disability globally. Hemodynamic parameters are essential to the assessment of CVD risks. Arterial compliance is defined as the change of arterial blood volume for a given change in pressure and reflects the extent of arterial stiffness. Pulse wave velocity (PWV) describes the propagation of pulsatile activity due to ventricular ejection of blood and its interaction with arterial compliance [1]. Carotid-femoral PWV (cfPWV) and brachial-ankle PWV (baPWV) are associated with future CVD risk and commonly measured for clinic use. Compared with cfPWV, baPWV can be easily obtained by the oscillometric method with cuffs on the 4 limbs and is more widely used [2].

Owing to the advance of technology, wearable devices with automatic or self-assisted monitoring have been recognized as a promising tool to facilitate the assessment and management of CVD risks. Photoplethysmography (PPG) [3,4], ballistocardiography [5,6], electrical bioimpedance [7], or tonometry [8] has been widely studied for these purposes. Due

to the ease of implementation, the optical PPG module is more often integrated into the wearable devices. The potential of estimation of BP [9,10] and PWV [11-13] from PPG signals attracts much attention.

Various approaches have been investigated to estimate PWV from PPG signals of different measurement sites [14]. The contour of PPG and its associated time interval features have been used to estimate either baPWV or cfPWV by approaches including multiple regression, artificial neural network, and support vector machine [15,16]. Most of the prior works used finger PPG signals for PWV estimation because of its clear contour and ease of feature extraction, compared with wrist PPG [17,18]. However, with the growing popularity of smartwatches as wearable health care devices, the use of wrist-based PPG in biomedical applications has attracted considerable attention. In this study, we aimed to estimate baPWV from wrist PPG and electrocardiography (ECG).

Methods

Methods and statistical analysis are briefly summarized in this section. Further details are provided in the Supplementary Section.

Data Collection

Figure 1 shows the measurement flow. Each volunteer wore a SENSIO smartwatch recording wrist PPG and ECG during the experimental period. For volunteers in the health management center, 3 rounds of measurements were conducted. For volunteers in the outpatient clinic, 5 rounds of measurements were made. In each round, the participants maintained the sitting position, and ECG was measured in the first minute. Blood pressures were then measured by the sphygmomanometer on the other arm (not wearing the smartwatch) with the cuff aligned at the heart level. A one-minute rest was reserved between 2 adjacent rounds. The wrist PPG signals were continuously recorded throughout the course. In the end, baPWV was measured by the OMRON noninvasive vascular screening device, with the cuffs on 4 limbs in the supine position.

Figure 1. Measurement flow. baPWV: brachial-ankle pulse wave velocity; ECG: electrocardiography; PPG: photoplethysmography.

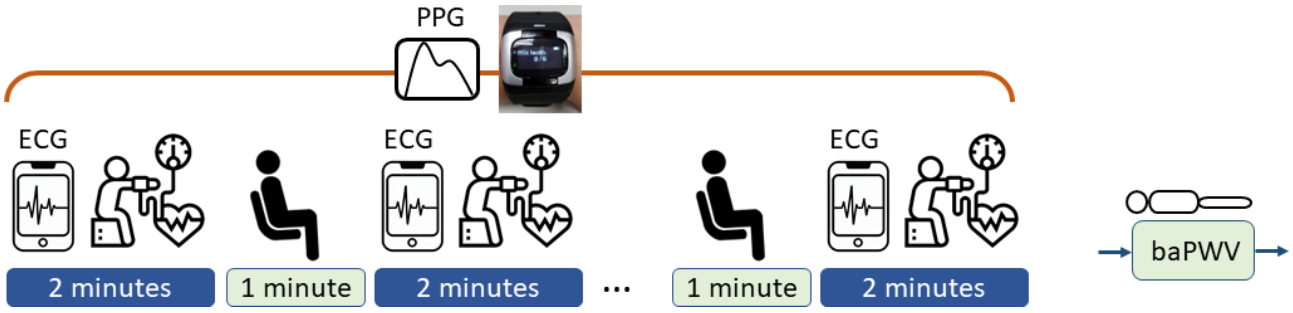

Ethical Considerations

The experiment was approved by the research ethics committee of National Taiwan University Hospital (number 201902087RIPA). All data were collected in accordance with the approved protocol. Importantly, the dataset used in this study did not contain any personally identifiable information, and all records were fully anonymized prior to analysis. Informed consent was obtained from all participants, and the study was conducted in compliance with the ethical standards set forth in the Declaration of Helsinki and relevant national regulations.

Processing Flow

The signal-processing flow is indicated in Figure 2. The PPG and ECG, sampled at 256 Hz, were extracted from the first minute of each round in the synchronization phase (Figures S1 A and S1 B in Multimedia Appendix 1). In the preprocessing phase, baseline wandering of signals was corrected by the discrete wavelet transform, and the 60-Hz power interference was suppressed by the notch filter. The amplitude of the whole signal segment was then normalized to [−1, +1]. The R peak of ECG and the valley of PPG signals were detected to calculate cycle length (Figures S1 C and S1 D in Multimedia Appendix 1). The skewness and variation of ECG and PPG cycle lengths were adopted to establish the signal quality index to exclude suboptimal ECG or PPG cycles for feature extraction. The first-order derivative PPG (FDPPG) and the second-order derivative PPG (SDPPG) signals were calculated. The systolic peak, notch, and diastolic peak were marked by the algorithm [19] for each PPG cycle (Figure 3A). The maximal slope (max slope) of the ascending systolic pulse, corresponding to the maximal rate of blood volume change, was identified by the first local maximum in FDPPG (Figure 3B) [20]. The local extrema of the SDPPG in systole are defined as a, b, c, and d points, where points a and c are local maxima and points b and d are local minima (Figure 3C) [21]. Point e is the local maximum around the boundary of systole and diastole in SDPPG. Point f is the first local minimum after point e.

The PPG pulse is regarded as a summation of several component waves, including the forward waves by left ventricular contraction and the distally reflected waves due to aortic elasticity and reservoir property [22]. The pulse decomposition analysis helps segregate the component waves [23]. With proper weighting, the variation of component waves can be reduced [24]. Five Gaussian waves are used for synthesizing the PPG pulse. Given $\theta i=\alpha i,\beta i,\gamma i$ corresponding to pulse amplitude, pulse position, and pulse width of the component wave i, and $\Theta=\{\theta 1, \theta 2, \ldots,\theta 5\}$, the summation of the Gaussian waves takes the form of

$$(1)\quad G(t|\theta)=\sum i=15 g(t|\theta i)$$

with

(2)g(t|θi)=αie(t−βiTs)22(γiTs)2

Denote G_i as the component wave described by g(t|θi). Given the boundary constraints, Lαi≤αi≤Uαi, Lβi≤βi≤Uβi, and Lγi≤γi≤Uγi [24], the interior-point method is used to solve the following optimization problem,

(3)Θ^=arg minΘ1M∑n=1Mw(n)[s(n)−G(nTs|Θ)],

where w(n) is the weight to emphasize the informative portion of the PPG pulse sn with length M and is given by

(4)w(n)={ωna≤n≤nf1else

Variables na and nf refer to the position of points a and f. The weight ω is set to 80 for stabilizing the variation of component waves in the sequence with acceptable mean square error between the synthesized waveform and original waveform.

Once the component waves are acquired, the forward wave is generated by combining G_1 and G_2. The systolic wave and diastolic wave are derived by combining G_1 to G_3 and G_4 to G_5, respectively. The respective peaks of the synthesized forward wave, systolic wave, and diastolic wave are named as pf, ps, and pd. In the following, the amplitude and position of feature x in the PPG pulse are indicated by Ax and nx, respectively. The amplitude of feature x in the ith-order derivative PPG is represented byAx(i). The result of decomposed component waves by weighted pulse decomposition (WPD) is shown in Figure 4.

Figure 2. Signal-processing flow. ECG: electrocardiography; PPG: photoplethysmography; SQI: signal quality index; WPD: weighted pulse decomposition.

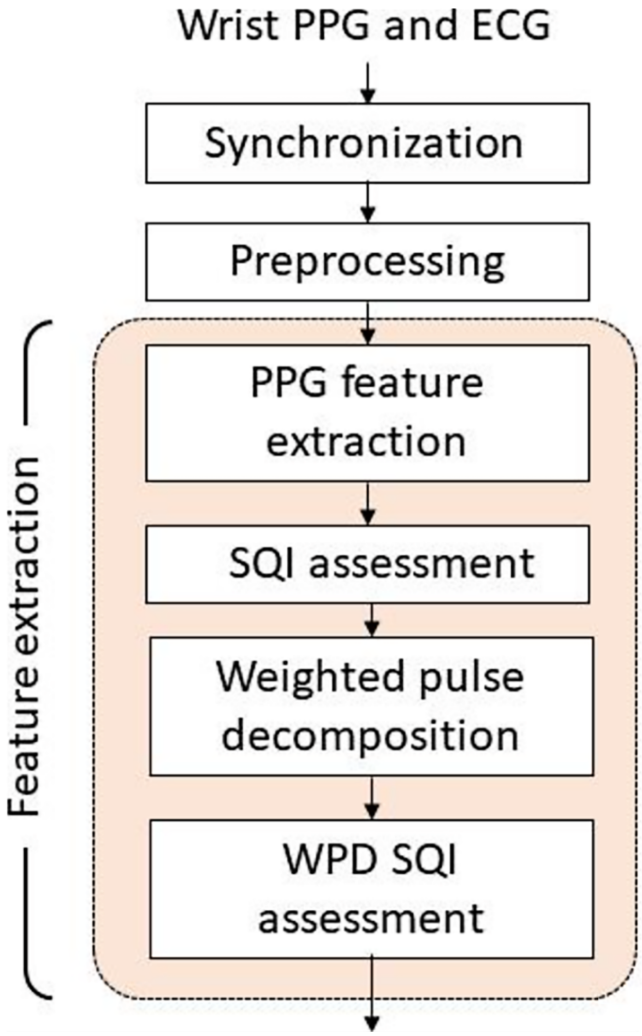

Figure 3. Photoplethysmography, first-order derivative photoplethysmography, and second-order derivative photoplethysmography waveforms and features in 1 cardiac cycle (from A to C). FDPPG: first-order derivative photoplethysmography; PPG: photoplethysmography; SDPPG: second-order derivative photoplethysmography.

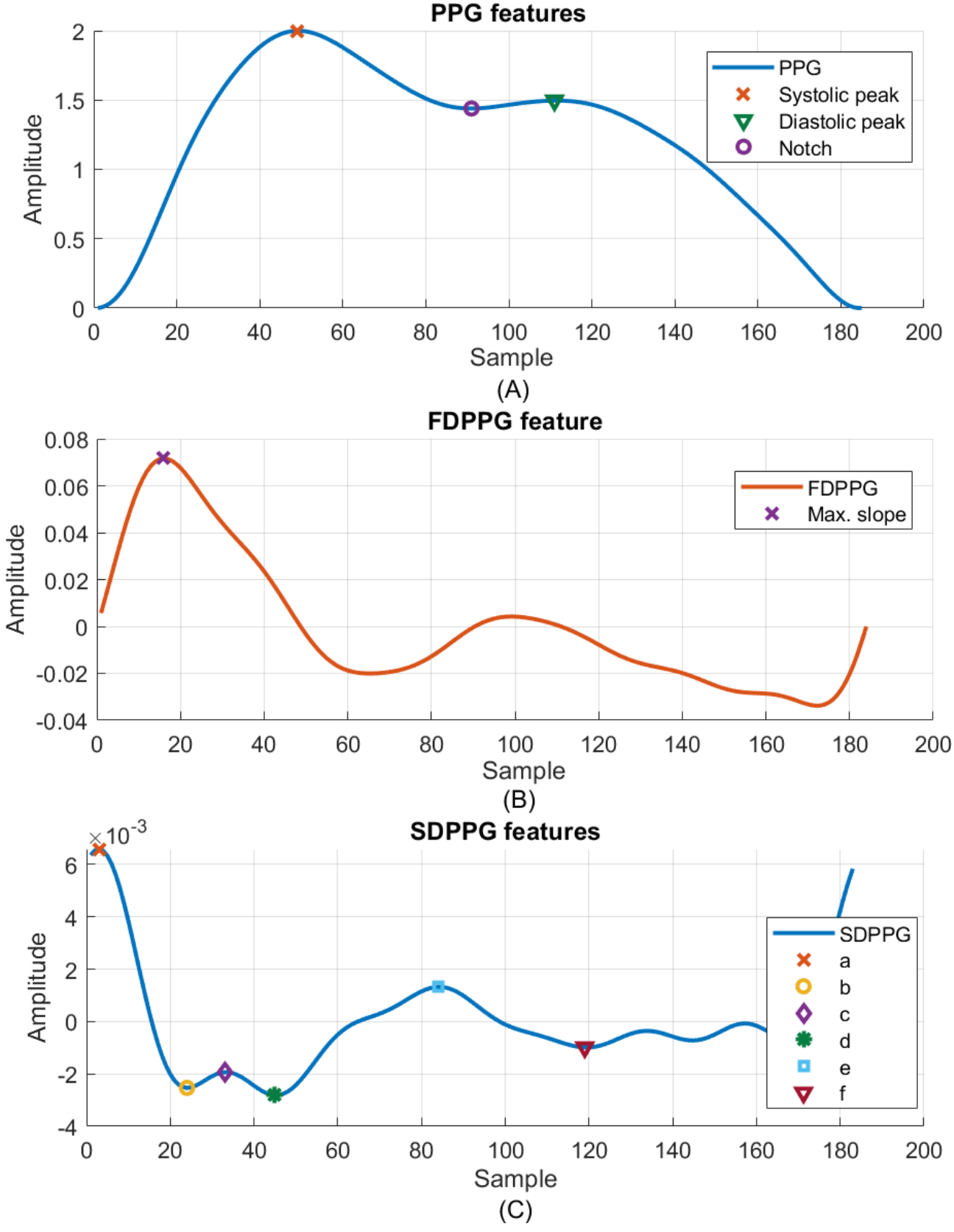

Figure 4. Component waves after weighted pulse decomposition. G1: Gaussian component wave 1; G2: Gaussian component wave 2; G3: Gaussian component wave 3; G4: Gaussian component wave 4; G5: Gaussian component wave 5; WPD: weighted pulse decomposition.

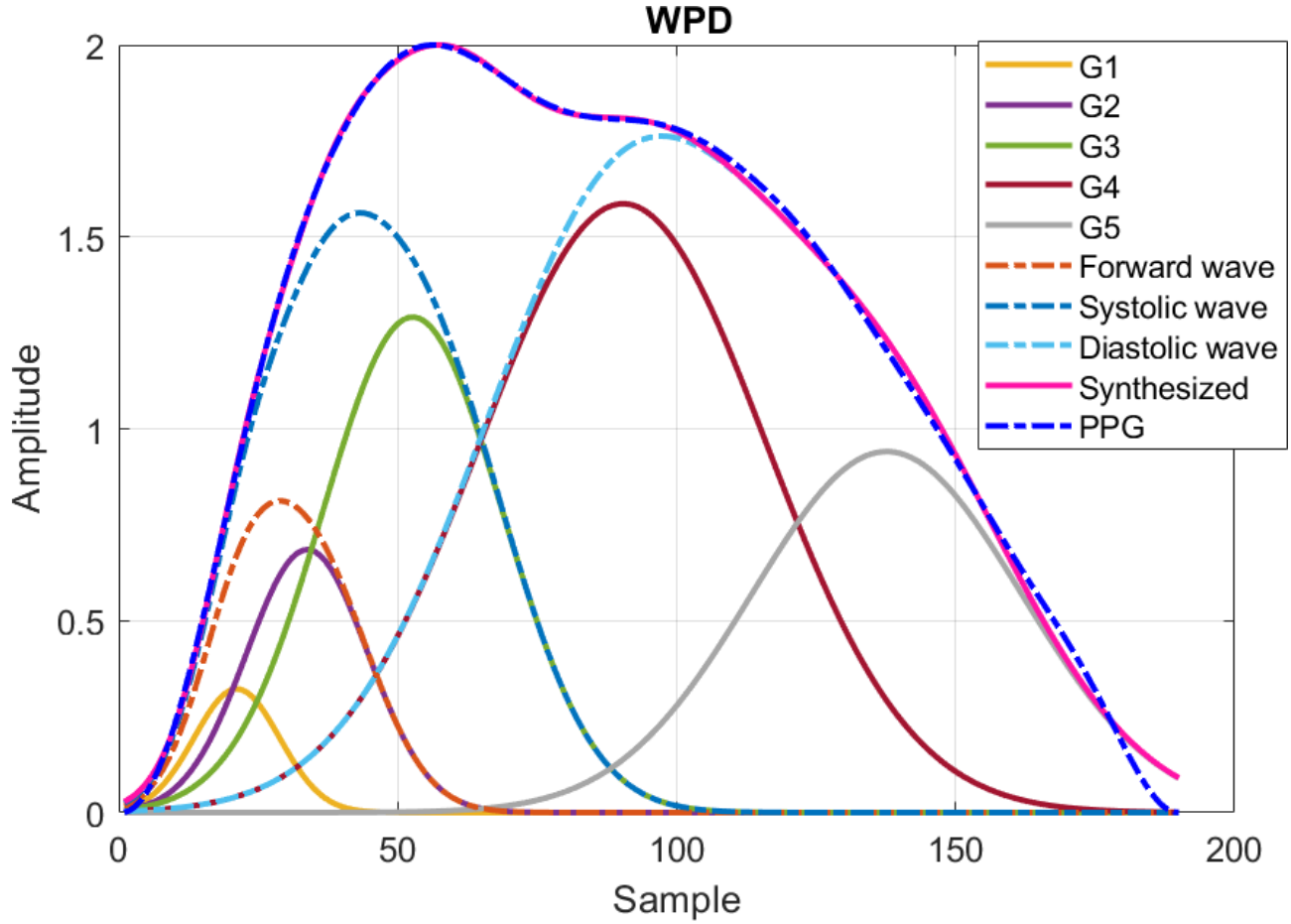

To assess the quality of WPD, WPD signal quality index, which was defined as mean square error between the PPG pulse, s(n), and the synthesized pulse, G(nTs|Θ), of >2×10-3, was implemented to remove disqualified pulses.

A total of 22 features were derived from the PPG pulse, FDPPG, and SDPPG (Table S1 A in Multimedia Appendix 2). The age index, which has been shown to be correlated with the augmentation index of aortic pressure [21,25],

(5)Ab(2)−Ac(2)−Ad(2)−Ae(2)Aa(2)

and its related variant combining only highly correlated components,

(6)Ab(2)−Ac(2)−Ad(2)Aa(2)

were also used. There were 27 features derived from WPD (Table S1 B in Multimedia Appendix 2). The stiffness index (SI) is defined as the time interval between the peaks of systolic and diastolic waves [23] and is denoted by npd-nps. The time intervals of the third or fourth component wave to the forward wave were also calculated. Note that nps and npd were obtained from synthesized systolic wave peak ps and diastolic wave peak pd of WPD as shown in Figure 4 while nsys and ndia were marked as the positions of systolic peak and diastolic peak in PPG as shown in Figure 3.

The ECG-related features were also adopted (Table S1 C in Multimedia Appendix 2). The R peak and T peak of the ECG waveform were identified and marked as nR and nT. Since the R peak occurs earlier than the PPG valley of the same heartbeat, nR is negative in number. The pulse arrival time (PAT) measures the time span between R peak and PPG valley, denoted by -nR. PAT^2 and $Height^2/PAT^2$ were included since either linear or nonlinear relationship between BP and pulse transit time has been shown [26]. The time span from R peak to maximum slope, peak of systolic wave, or component wave 2 was also considered.

Basic information (Table S1 D in Multimedia Appendix 2) contains age, height (H), weight, BMI, and lengths from arm to wrist (Law) and finger (Laf). The lengths from heart to brachium (Lb) and from heart to ankle (La) can be approximated by [27]

(7)La=0.8219H+12.328

(8)Lb=0.2195H−2.073.

The length difference between ankle and brachium could be expressed by La-Lb.

Feature normalization is often adopted since the relative change of 2 features could provide additional information than each feature alone. To systematically derive the normalization results, we generate combined features by dividing the value of feature u by value of feature v. The combined features contain not only magnitude-normalized or time-normalized features but also basic information features.

Estimation Approach

Multivariable Regression

Linear regression and multivariable regression had been applied for baPWV estimation [12,28]. The time difference between the systolic peak to diastolic peak has been used and normalized by the Fridericia formula [28] while the systolic peak to the next onset (P2O), M-nsys (feature 1 in Table S1 A in Multimedia Appendix 2), of the PPG signal normalized by the PPG pulse length was also examined for PWV estimation [12]. These 2 variables were selected from the finger PPG features by the authors due to their high correlation to baPWV reported in the literature. The wrist PPG was used in this study for baPWV estimation. Because diastolic peak often vanished in wrist PPG pulses, we used SI (feature 51 in Table S1 B in Multimedia Appendix 2), which denotes the time span between peaks of decomposed systolic wave and diastolic wave according to WPD, and its normalized form with the Friderician formula is given by SI/M1/3. The multivariable linear equations are described by [12,28]

(9)PWV=C1Age+C2SIM1/3+C3

and

(10)PWV=C1Age+C2P2OM+C3.

Hierarchical Regression

The linear estimation regarding the correlations between PPG features and PWV, as used in multivariable regression analysis, may oversimplify the vascular hemodynamic state. The machine learning algorithms have been prosperously developed and used for biomedical applications, such as neural network and decision tree regression for estimation of vascular age [29] and gradient boosting decision tree regression for estimation of blood pressure [30]. We herein developed the hierarchical regression model based on the random forest and extreme gradient boosting (XGBoost) algorithms. A general regression model by XGBoost was also implemented for comparison.

The random forest and XGBoost algorithms of high scalability have been shown to achieve excellent performance in many fields [31]. In the random forest algorithm, a large number of decision trees are constructed. A different subset of the data and a random selection of features are used for each decision tree to prevent overfitting in the training process. The final classification is often made by taking the majority vote. On the other hand, inherited from gradient boosting, XGBoost adds the new regression tree in each iteration to improve the previous prediction and to approach the target. The XGBoost introduces the regularization term that considers the complexity of the tree so as to avoid overfitting. In addition, the second-order gradient statistics are used for accelerating the computation.

The concept of hierarchical regression can be described as classification by random forest algorithm and then regression by XGBoost algorithm (Multimedia Appendix 3). The whole PWV range is partitioned into several subdivisions. Thus, a global classifier handles the entire PWV range, and several local regressors are in charge of the respective subdivisions. First, an outcome regarding the possible baPWV subdivision is generated by the global classifier. Then, the estimation result is calculated by the associated local regressor. Because it is possible that the data around the subdivision boundary are erroneously classified, the adjacent regressors are designed to have an overlapping zone to extend the respective coverages. Owing to the data quantity, 2 subdivisions were adopted and the boundary threshold was set at 1600 cm per second. The widths of the overlapping zone were set as 200 cm per second, 400 cm per second, and 600 cm per second.

Statistical Analysis

The differences between the estimated results v^j and the measured PWV vj of the jth measurement are shown by the mean absolute error, mean error, SD, and root-mean-square error (RMSE), which are defined as follows.

(11)ej=vj−vj^

(12)MAE=E{|ej|}

(13)ME=e−=E{ej}

(14)SD=1N−1∑j=1N(ej−e−)2

(15)RMSE=E{ej2}.

The correlation coefficients together with *P* values are also provided. Since some participants have more than 1 measurement, to avoid unbalanced weighting, averaged PWV estimation and averaged PWV measurement are used for the statistical results per participant.

Results

In this study, 80 male participants and 82 female participants were recruited. Their demographic characteristics are shown in Table 1. The averaged PWV value of left baPWV and right baPWV was used. The PWV values of male participants and female participants were 1591 (SD 266) cm per second and 1613 (SD 321) cm per second. Among total participants, 39 male participants and 23 female participants had more than 1 PWV values due to their multiple visits. A total of 914 PPG as well as ECG sequences were collected from the smartwatch, corresponding to 278 PWV values. On average, 1 male participant has 3.5 PPG and ECG sequences associated with 1 PWV measurement while 1 female participant has 3.1 PPG and ECG sequences for 1 PWV measurement. Among 278 PWV measurements, there are 123 PWV measurements from participants taking antihypertensive medications on the same day.

The medians of the respective combined features in the 528 and 386 sequences were used for computing correlation coefficients for men and women. The correlation coefficients of combined features defined by the X and Y indices are often higher than the original one (Multimedia Appendix 4). For example, the correlation coefficients of the age and maximum slope time (nms) to baPWV are 0.334 and −0.281, whereas the correlation coefficient of the combined feature Age/nms becomes 0.491 (Multimedia Appendix 5). The correlation coefficients of SI corrected by Friderician's formula and the time interval between systolic peak to the onset of next PPG (P2O) normalized by pulse length from the wrist PPG versus baPWV are −0.271 (*P*<.001), −0.036 (*P*=.413) and −.370 (*P*<.001), −0.070 (*P*=.171) for men and women, respectively.

The reproducibility of the measured baPWV was also checked. The PWVs of 31 participants were measured twice by the same OMRON noninvasive vascular screening device with 1-minute separation. The maximal differences of left baPWV and right baPWV of these participants were 276 cm per second and 210 cm per second, respectively. The maximal difference of averaged baPWV from left baPWV and right baPWV was 196.5 cm per second. The RMSEs of 2 consecutively measured left baPWV and right baPWV were 83.4 cm per second and 62.0 cm per second, respectively. The RMSE of consecutive averaged baPWV was 68.8 cm per second.

For multivariable regression, 39 and 34 PWV measurements from 24 male participants and 26 female participants, respectively, were reserved as the testing dataset. The medians of the respective features from the sequences associated with the same PWV measurement were averaged. The testing dataset was selected to approach uniform distribution in the range between 1000 cm per second and 2100 cm per second. The mean and SD of the male and female PWV values in the testing dataset were 1538 (SD 237) cm per second and 1638 (SD 283) cm per second. The training dataset for deriving the coefficients contained 114 PWV measurements with 391 PPG per ECG sequences from 56 male participants and 91 PWV measurements with 291 sequences from 56 female participants. The participant-split criterion is obeyed. The baPWV estimation results by multivariable regression are shown in Table 2 for men and women, respectively.

Table . Demographic summary.[a]

Characteristics	Male participants, mean (SD; n)	Female participants, mean (SD; n)
Age (years)	63.4 (13.4; 80)	64.3 (11.6; 82)
Heart rate (bps)	73.9 (12.7; 528)	71.0 (8.2; 386)
SBP[b] (mm Hg)	126.0 (15.7; 528)	125.9 (17.9; 386)
DBP[c] (mm Hg)	79.4 (10.6; 528)	77.0 (12.0; 386)
PWV[d] (cm per second)	1591 (266; 153)	1613 (321; 125)

[a]Among a total of 278 pulse wave velocity measurements, 123 measurements were obtained from participants taking antihypertensive medications on the same day.

[b]SBP: systolic blood pressure.

[c]DBP: diastolic blood pressure.

[d]PWV: pulse wave velocity.

Table . Estimation results from multivariate regression[a].

Methods	N	MAE[b] (cm per second)	ME[c] (cm per second)	SD (cm per second)	RMSE[d] (cm per second)	Correlation coefficient (*P* value)
Men						
PWV=C1Age+C2SM2+C3 [28[e,f]]	39 rounds	179.1	−49.0	214.3	217.2	0.44 (.006)
	24 participants	160.4	−40.4	195.7	195.8	0.55 (.006)
PWV=C1Age+C2P2O+C3 [12]	39 rounds	189.0	−57.7	219.8	224.6	0.37 (.02)
	24 participants	176.1	−48.1	207.8	209.1	0.43 (.04)
Women						
PWV=C1Age+C2SM2+C3 [28]	34 rounds	165.2	1.8	211.7	208.6	0.66 (<.001)
	26 participants	157.4	−12.1	197.4	194.0	0.72 (<.001)
PWV=C1Age+C2P2O+C3 [12]	34 rounds	196.0	10.0	233.0	229.8	0.62 (<.001)
	26 participants	188.8	8.6	221.8	217.6	0.67 (<.001)

[a]The testing set contained 39 and 34 pulse wave velocity measurements from 24 male participants and 26 female participants, respectively.

[b]MAE: mean absolute error.

[c]ME: mean error.

[d]RMSE: root-mean-square error.

[e]PWV indicates pulse wave velocity.

[f]SI: stiffness index.

[g]P2O: systolic peak to the next onset.

For hierarchical regression, the same training and testing datasets as those in multivariable regression were used to keep participants split. The training dataset was oversampled to make the distribution balanced in each interval of 100 cm per second.

Several parameters, such as the shrinkage factor, tree depth, and column subsampling, are required for the random forest and XGBoost algorithms. Hence, a validation set split from the training dataset was used for parameter settings. Because the number of PWV measurements of extreme high and low values was not sufficiently large, leave-one-out validation was used to ensure that the model for validation is similar to that for training. For the general model, the male validation set contained 23 participants and 33 PWV measurements, while the female validation set had 22 participants and 39 PWV measurements. The validation set consisted of more than one-third of participants in the training dataset and kept uniformly distributed in the range from 1000 cm per second to 2100 cm per second. During leave-one-out validation, all the PPG or ECG sequences associated with the PWV measurements of 1 validation participant were removed from the training dataset to avoid data leak. For each submodel of the local regressor, the validation dataset in each subdivision includes those with the PWV measurements in the overlapping zone. Given the overlapping zone of 400 cm per second, there were 24 PWV measurements from 13 male participants and 26 PWV measurements from 12 female participants in the high submodel for validation from 1400 cm per second. On the other hand, 25 PWV measurements from 13 male participants and 25 PWV measurements from 16 female participants were used in the low submodel for validation up to 1800 cm per second.

Table 3 lists the estimation results from the general and hierarchical regression models by the random forest classification and XGBoost regression algorithms with different settings of the width of the overlapping zones. First, the RMSE results from the hierarchical regression models are better than those from the multivariable linear regression model. The hierarchical regression model also outperforms the general regression model. Figures 5 and 6 show the Bland-Altman and scatter plots of regression results by the hierarchical regression model with overlapping zone of 400 cm per second for men and women participants. Their participant numbers are indicated in the legend. Good estimation was obtained for this setting. The left subfigures indicate the Bland-Altman plot. The scatter plots in the right subfigures provide the final estimation results. The classification accuracies of total rounds from male participants and female participants are 76.9% and 91.2%, respectively. The estimation of erroneously classified data close to the boundary got improved with the introduction of an overlapping zone. The best estimation results achieve RMSE of 145.0 cm per second and 141.4 cm per second for men and women, respectively. In the random forest classifier for male participants, the number of estimators is 100 and the maximum tree depth is 20. As to the random forest for female participants, the number of estimators is 250 and the maximum tree depth is 9. In both cases, the minimum samples for tree split should be larger than 2 and the minimum number of samples in leaf nodes is 1. As to the XGBoost regressors, the number of estimators is 200; the fraction of features sampled for each tree is 0.7; and the minimum loss reduction for further partition is 0. The maximum depth of the low submodel for male participants is 5 and is set to 3 for the remaining submodels.

The XGBoost algorithm performs tree splitting by evaluating structure scores to accumulate gradient statistics according to the sorted feature values while the random forest algorithm can assess the impact on pureness of the leaves from a feature. Hence, both can report the feature importance. Given the overlapping zone of 400 cm per second in the hierarchical regression model, besides PAT (nR), PAT square (nR2), and age, PPG features and WPD features were also frequently used (Multimedia Appendix 6). Local regression models used features different from those used in global classification models. Features from component wave, points a, b, c, and d of SDPPG were often adopted.

Table . Hierarchical regression results for men and for women are listed.

Method	Overlapping zone (cm per second)	N	MAE[a] (cm per second)	ME[b] (cm per second)	SD (cm per second)	RMSE[c] (cm per second)	Correlation coefficient (*P* value)
Men							
General regression	—[d]	39 rounds	157.4	−16.5	187.0	185.3	0.61 (<.001)
General regression	—	24 participants	141.7	−8.4	173.1	169.7	0.66 (<.001)
Hierarchical regression	200	39 rounds	156.0	−19.4	185.3	183.9	0.64 (<.001)
Hierarchical regression	200	24 participants	152.1	−18.4	185.6	182.6	0.63 (.001)
Hierarchical regression	400	39 rounds	133.6	−8.1	160.1	158.3	0.74 (<.001)
Hierarchical regression	400	24 participants	126.5	−8.9	147.8	*145.0* [e]	*0.77*[e] (<.001)
Hierarchical regression	600	39 rounds	153.6	−2.3	182.9	180.5	0.63 (<.001)
Hierarchical regression	600	24 participants	143.6	13.7	165.0	162.1	0.70 (<.001)
Women							
General regression	—	34 rounds	174.3	−36.0	217.0	216.8	0.67 (<.001)
General regression	—	26 participants	177.7	−22.4	217.8	214.7	0.66 (<.001)
Hierarchical regression	200	34 rounds	141.5	−20.7	171.0	169.7	0.80 (<.001)
Hierarchical regression	200	26 participants	131.4	−29.2	157.4	157.0	0.83 (<.001)
Hierarchical regression	400	34 rounds	127.3	−3.5	156.7	154.5	0.83 (<.001)
Hierarchical regression	400	26 participants	116.7	−6.0	144.1	*141.4* [e]	*0.86*[e] (<.001)
Hierarchical regression	600	34 rounds	144.3	24.2	173.9	173.0	0.79 (<.001)
Hierarchical regression	600	26 participants	141.2	24.0	173.5	171.8	0.79 (<.001)

[a]MAE:mean absolute error.

[b]ME: mean error.

[c]RMSE: root-mean-square error.

[d]Not applicable.

[e]Values in italics indicate best estimation result with acceptable accuracy set by the ARTERY Society.

Figure 5. (A) Bland-Altman plot and (B) scatter plot of pulse wave velocity regression by the hierarchical regression model with 2 submodels and overlapping zone of 400 cm per second for 24 men. PWV: pulse wave velocity.

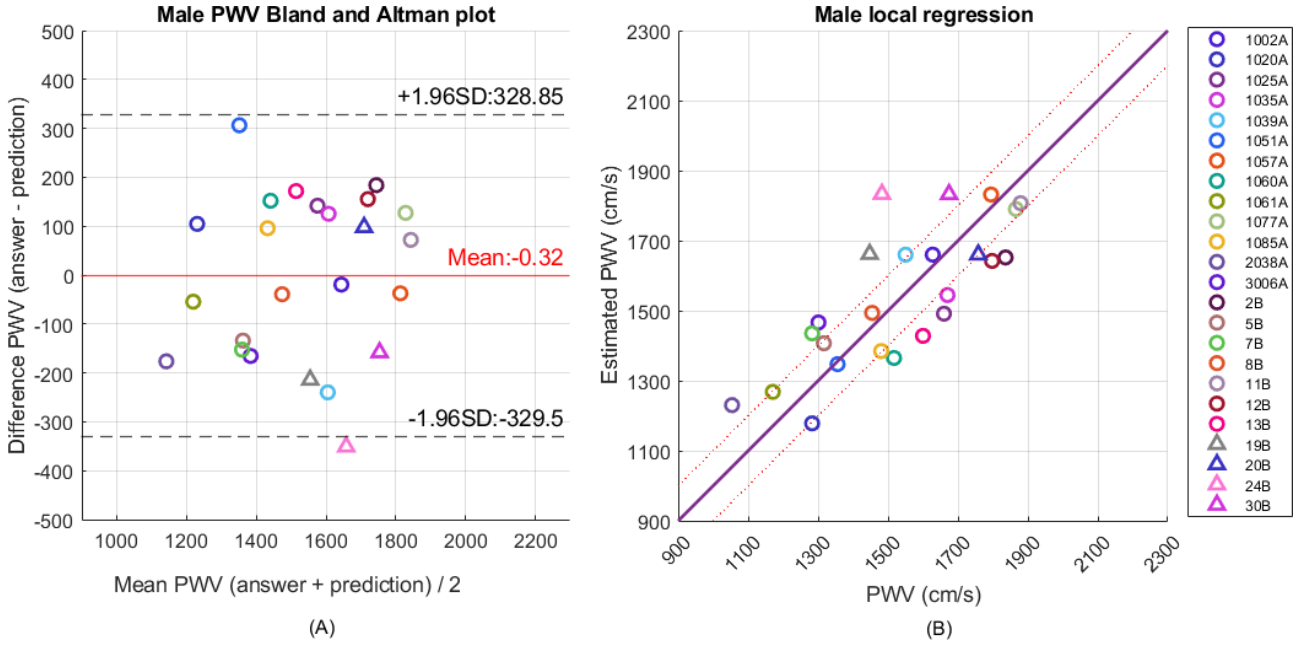

Figure 6. (A) Bland-Altman plot and (B) scatter plot of pulse wave velocity regression by the hierarchical regression model with 2 submodels and overlapping zone of 400 cm per second for 26 women. PWV: pulse wave velocity.

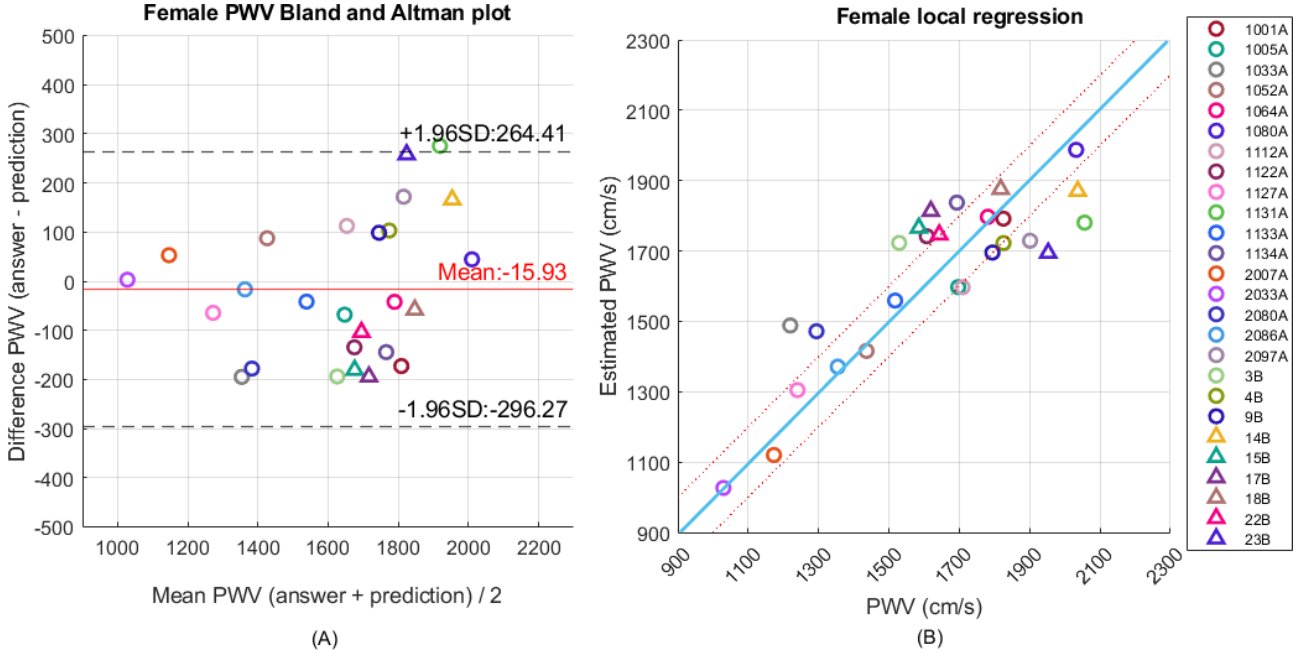

Discussion

Principal Findings

In this study, we used wrist PPG and ECG signals to estimate baPWV. The morphology of wrist PPG signals is quite different from that of finger PPG signals. The conventional approach that used finger PPG morphology features may encounter the problem of feature missing due to much fewer identifiable features of wrist PPG signals. In addition, the multivariable regression model used in prior works may be too simple to describe the complicated hemodynamic state in the vessels. Hence, we resorted to the machine learning algorithm to deal with the estimation. Although the wrist PPG and ECG signals were acquired before the baPWV measurement, they are still related to the vessel condition and stiffness. To further improve and refine the estimation results, hierarchical regression was adopted to shrink the range handled in the submodel. The achieved RMSE and SD by our hierarchical regression models for both men and women are lower than the threshold (150 cm per second) of acceptable accuracy for PWV estimation set by the ARTERY Society [32].

Comparison With Prior Work

With the WPD and feature imputation techniques developed by us, more than 98% of all ambiguous and missing features of wrist PPG can be identified [19]. From the correlation results (Multimedia Appendix 4), besides age (feature 23) and age

square (feature 63), correlation related to SDPPG amplitude of point c (feature 18), point d (feature 19), and point e (feature 20) are still obvious as what has been mentioned in finger PPG [25]. In addition, SI (npd-nps; feature 51), which are often missing in the original wrist PPG pulses, can be computed through the synthesized systolic and diastolic waves in decomposed wrist PPG. According to the feature importance (Multimedia Appendix 6), it still plays an important role for PWV estimation.

The multivariable regression uses only a few features. If significantly high correlations of those features to baPWV do not appear, the performance of estimation will be degraded. However, the machine learning algorithm can help exploit more linear or nonlinear information embedded in the PPG waveform or its component waves and thus is suitable for these applications. Furthermore, the combined features from PPG and ECG morphology, WPD, and basic information supplied more feature information sources that can be selected by the model.

Hierarchical Model Insights

The concept of hierarchical regression is to introduce different models to refine the estimation results. However, the global classifier or regressor must provide sufficiently correct classification to avoid model mismatch. From the hierarchical regression results, it is clear that the inclusion of overlapping zone in local regressors indeed improved the estimation results, as reflected in the improved correlation coefficients (Table 2). However, the determination of optimal range of overlapping zone is still controversial. If the overlapping zone is too wide, the hierarchical regression model would become similar to the general regression model. On the other hand, if the overlapping zone is too narrow, the misclassified data cannot be properly handled. In this study, we recommend the overlapping zone of 400 cm per second of 2 subdivision models because the misclassified data are near the boundary due to good capability of the global classifier and can be appropriately covered by the submodel. We conducted further analysis on the features that were misclassified for those samples not near the decision boundary. The results showed no significant outliers. Additionally, the vote counts for 2 classes across the entire forest were close, indicating low confidence among the trees. The latent properties beyond the observed features should be further studied. On the other hand, we also applied a Kernel Density Estimation–based mutual information analysis [33] to assess the relevance of individual features in male and female datasets. The mutual information values from male features were lower than those from female features, which can also explain the lower classification accuracy in male participants of our dataset.

Limitations and Future Directions

This study has limitations, which point to the directions for future research. First, the sample size remained small and more older adult people were recruited in the study, which might limit its applicability in younger populations. While the current dataset demonstrates feasibility in estimating PWV using wrist PPG in older individuals, the skewed dataset toward older individuals may have influenced the performance due to age-related vascular characteristics. In future work, we plan to expand the study population by actively recruiting more young participants. The inclusion of younger participants will help balance the age distribution and allow for more robust assessment of the model performance across different age groups. This extension will not only improve the generalizability of the model but also enable a more comprehensive evaluation of age-related vascular changes. Second, the current model adopts machine learning algorithms to exploit linear and nonlinear features within the scope of this dataset. As the dataset grows in size and diversity, other deep learning algorithms, such as Bayesian neural networks or multilayer perceptrons, can be applied, which may offer better uncertainty quantification or modeling capabilities. Third, the feature space used in the current model is relatively high-dimensional, which may hinder its practical deployment on wearable or edge devices with limited computational resources. Feature compression or dimensionality reduction techniques can be considered to decrease model complexity in the future. This optimization will help make the system more suitable for real-time, low-power applications in wearable health care settings. Together, these improvements aim to enhance both the robustness and the applicability of the proposed approach, facilitating its transition toward practical use in diverse and real-world scenarios.

Acknowledgments

The authors would like to acknowledge Mr Bowen Ku of Mediatek Inc for his design experience feedback about wearable devices in biomedical applications. This work is supported by Mediatek Inc (grant numbers MTKC-2021 - 0477 and MTKC-2023 - 1363).

Authors' Contributions

P-YT, C-HH, and Y-CL contributed to conceptualization; P-YT contributed to methodology; C-IH, C-HY, C-HH, Y-CL, and J-WG contributed to software; C-IH, C-HY, and Y-CL participated in validation; T-DW and H-JL contributed to resources; P-YT participated in writing—original draft preparation; T-DW participated in writing—review and editing; and T-DW, P-YT, and H-JL participated in supervision. All authors have read and agreed to the published version of the manuscript.

Conflicts of Interest

PYT has received research grants (grant numbers MTKC-2021 - 0477 and MTKC-2023 - 1363) from Mediatek Company. All other authors have no relevant relationships to disclose.

Multimedia Appendix 1
(A) Electrocardiography before preprocessing, (B) photoplethysmography before preprocessing, (C) electrocardiography with R peak after preprocessing, and (D) photoplethysmography with valley after preprocessing.
[PNG File, 97 KB - biomedeng_v10i1e58756_app1.png]

Multimedia Appendix 2
List of extracted features: (A) photoplethysmography features, (B) weighted pulse decomposition features, (C) electrocardiography features, and (D) basic information.
[DOCX File, 23 KB - biomedeng_v10i1e58756_app2.docx]

Multimedia Appendix 3
Concept of hierarchical regression.
[PNG File, 251 KB - biomedeng_v10i1e58756_app3.png]

Multimedia Appendix 4
Heat map of correlation coefficients of combined features (defined in Tables S1 A, S1 B, S1 C, and S1 D in Multimedia Appendix 2) versus brachial-ankle pulse wave velocity for (A) 80 male participants and (B) 82 female participants with 528 and 386 data, respectively. The diagonal elements are the correlation coefficients of original features. The off-diagonal elements are the correlation coefficients of combined features.
[PNG File, 71 KB - biomedeng_v10i1e58756_app4.png]

Multimedia Appendix 5
The distributions of brachial-ankle pulse wave velocity versus (A) age, (B) n_{ms}, and (C) Age/n_{ms} for 386 female data.
[PNG File, 79 KB - biomedeng_v10i1e58756_app5.png]

Multimedia Appendix 6
Top 10 important features of classification and local regression for (A) men and (B) women.
[DOCX File, 24 KB - biomedeng_v10i1e58756_app6.docx]

References

1. Pereira T, Correia C, Cardoso J. Novel methods for pulse wave velocity measurement. J Med Biol Eng 2015;35(5):555-565. [doi: 10.1007/s40846-015-0086-8] [Medline: 26500469]
2. Ohkuma T, Ninomiya T, Tomiyama H, et al. Brachial-ankle pulse wave velocity and the risk prediction of cardiovascular disease. Hypertension 2017 Jun;69(6):1045-1052. [doi: 10.1161/HYPERTENSIONAHA.117.09097]
3. Kachuee M, Kiani MM, Mohammadzade H, Shabany M. Cuffless blood pressure estimation algorithms for continuous health-care monitoring. IEEE Trans Biomed Eng 2017 Apr;64(4):859-869. [doi: 10.1109/TBME.2016.2580904] [Medline: 27323356]
4. Yan C, Li Z, Zhao W, et al. Novel deep convolutional neural network for cuff-less blood pressure measurement using ECG and PPG signals. Presented at: 2019 41st Annual International Conference of the IEEE Engineering in Medicine & Biology Society (EMBC); Jul 23-27, 2019; Berlin, Germany. [doi: 10.1109/EMBC.2019.8857108]
5. Wu Q, Yang J, Zheng G, et al. An ambulatory blood pressure monitoring system based on the uncalibrated steps of the wrist. Presented at: 2019 12th International Congress on Image and Signal Processing, BioMedical Engineering and Informatics (CISP-BMEI); Oct 19-21, 2019; Suzhou, China p. 1-6. [doi: 10.1109/CISP-BMEI48845.2019.8966011]
6. Yousefian P, Shin S, Mousavi AS, et al. Pulse transit time-pulse wave analysis fusion based on wearable wrist ballistocardiogram for cuff-less blood pressure trend tracking. IEEE Access 2020 Jul;8:138077-138087. [doi: 10.1109/ACCESS.2020.3012384]
7. Krivoshei A, Min M, Uuetoa H, Lamp J, Annus P. Electrical bio-impedance based non-invasive method for the central aortic blood pressure waveform estimation. Presented at: 2014 14th Biennial Baltic Electronic Conference (BEC); Oct 6-8, 2014; Tallinn, Estonia. [doi: 10.1109/BEC.2014.7320586]
8. Meidert AS, Saugel B. Techniques for non-invasive monitoring of arterial blood pressure. Front Med (Lausanne) 2018;4:231. [doi: 10.3389/fmed.2017.00231] [Medline: 29359130]
9. Priyanka KNG, Chao PCP, Tu TY, et al. Estimating blood pressure via artificial neural networks based on measured photoplethysmography waveforms. Presented at: 2018 IEEE Sensors; Oct 28-31, 2018; New Delhi p. 1-4. [doi: 10.1109/ICSENS.2018.8589796]
10. Schlesinger O, Vigderhouse N, Eytan D, Moshe Y. Blood pressure estimation from PPG signals using convolutional neural networks and Siamese network. Presented at: ICASSP 2020 - 2020 IEEE International Conference on Acoustics, Speech and Signal Processing (ICASSP); May 4-8, 2020; Barcelona, Spain. [doi: 10.1109/ICASSP40776.2020.9053446]

11. Warren S. High resolution wireless body area network with statistically synchronized sensor data for tracking pulse wave velocity. 2012 Presented at: 2012 34th Annual International Conference of the IEEE Engineering in Medicine and Biology Society (EMBC); Aug 28 to Sep 1, 2012; San Diego, CA p. 2080-2083. [doi: 10.1109/EMBC.2012.6346369]
12. Jang DG, Park SH, Hahn M. Enhancing the pulse contour analysis-based arterial stiffness estimation using a novel photoplethysmographic parameter. IEEE J Biomed Health Inform 2015 Jan;19(1):256-262. [doi: 10.1109/JBHI.2014.2306679] [Medline: 25561448]
13. Padilla JM, Berjano EJ, Facila SJ, Diaz P L, Merce S. Assessment of relationships between blood pressure, pulse wave velocity and digital volume pulse. Presented at: 2006 Computers in Cardiology; Sep 17-20, 2006; New Delhi, India p. 893-896.
14. Nabeel PM, Jayaraj J, Mohanasankar S. Single-source PPG-based local pulse wave velocity measurement: a potential cuffless blood pressure estimation technique. Physiol Meas 2017 Nov 30;38(12):2122-2140. [doi: 10.1088/1361-6579/aa9550] [Medline: 29058686]
15. Salvi P, Magnani E, Valbusa F, et al. Comparative study of methodologies for pulse wave velocity estimation. J Hum Hypertens 2008 Oct;22(10):669-677. [doi: 10.1038/jhh.2008.42] [Medline: 18528411]
16. Alty SR, Angarita-Jaimes N, Millasseau SC, Chowienczyk PJ. Predicting arterial stiffness from the digital volume pulse waveform. IEEE Trans Biomed Eng 2007 Dec;54(12):2268-2275. [doi: 10.1109/tbme.2007.897805] [Medline: 18075043]
17. Hartmann V, Liu H, Chen F, Qiu Q, Hughes S, Zheng D. Quantitative comparison of photoplethysmographic waveform characteristics: effect of measurement site. Front Physiol 2019;10:198. [doi: 10.3389/fphys.2019.00198] [Medline: 30890959]
18. Rajala S, Lindholm H, Taipalus T. Comparison of photoplethysmogram measured from wrist and finger and the effect of measurement location on pulse arrival time. Physiol Meas 2018 Aug 1;39(7):075010. [doi: 10.1088/1361-6579/aac7ac] [Medline: 29794339]
19. Tsai PY, Huang CH, Guo JW, et al. Coherence between decomposed components of wrist and finger PPG signals by imputing missing features and resolving ambiguous features. Sensors (Basel) 2021 Jun 24;21(13):4315. [doi: 10.3390/s21134315] [Medline: 34202597]
20. Warren S, Li K. Initial study on pulse wave velocity acquired from one hand using two synchronized wireless reflectance pulse oximeters. Annu Int Conf IEEE Eng Med Biol Soc 2011:6907-6910. [doi: 10.1109/IEMBS.2011.6091739]
21. Hashimoto J, Watabe D, Kimura A, et al. Determinants of the second derivative of the finger photoplethysmogram and brachial-ankle pulse-wave velocity: the Ohasama study. Am J Hypertens 2005 Apr;18(4 Pt 1):477-485. [doi: 10.1016/j.amjhyper.2004.11.009] [Medline: 15831356]
22. Davies JE, Baksi J, Francis DP, et al. The arterial reservoir pressure increases with aging and is the major determinant of the aortic augmentation index. Am J Physiol Heart Circ Physiol 2010 Feb;298(2):H580-H586. [doi: 10.1152/ajpheart.00875.2009] [Medline: 20008272]
23. Couceiro R, Carvalho P, Paiva RP, et al. Assessment of cardiovascular function from multi-Gaussian fitting of a finger photoplethysmogram. Physiol Meas 2015 Sep;36(9):1801-1825. [doi: 10.1088/0967-3334/36/9/1801] [Medline: 26235798]
24. Huang CH, Guo JW, Yang YC, et al. Weighted pulse decomposition analysis of fingertip photoplethysmogram signals for blood pressure assessment. Presented at: 2020 IEEE International Symposium on Circuits and Systems (ISCAS); 2020; Seville, Spain. [doi: 10.1109/ISCAS45731.2020.9180616]
25. Takazawa K, Tanaka N, Fujita M, et al. Assessment of vasoactive agents and vascular aging by the second derivative of photoplethysmogram waveform. Hypertension 1998 Aug;32(2):365-370. [doi: 10.1161/01.hyp.32.2.365] [Medline: 9719069]
26. Ding X, Zhang YT. Pulse transit time technique for cuffless unobtrusive blood pressure measurement: from theory to algorithm. Biomed Eng Lett 2019 Feb;9(1):37-52. [doi: 10.1007/s13534-019-00096-x] [Medline: 30956879]
27. Tomiyama H, Yamashina A, Arai T, et al. Influences of age and gender on results of noninvasive brachial-ankle pulse wave velocity measurement--a survey of 12517 subjects. Atherosclerosis 2003 Feb;166(2):303-309. [doi: 10.1016/s0021-9150(02)00332-5] [Medline: 12535743]
28. Jang DG, Farooq U, Park SH, Goh CW, Hahn M. A knowledge-based approach to arterial stiffness estimation using the digital volume pulse. IEEE Trans Biomed Circuits Syst 2012 Aug;6(4):366-374. [doi: 10.1109/TBCAS.2011.2177835] [Medline: 23853181]
29. Miao F, Wang X, Yin L, Li Y. A wearable sensor for arterial stiffness monitoring based on machine learning algorithms. IEEE Sensors J 2019 Feb;19(4):1426-1434. [doi: 10.1109/JSEN.2018.2880434]
30. Zhang B, Ren J, Cheng Y, Wang B, Wei Z. Health data driven on continuous blood pressure prediction based on gradient boosting decision tree algorithm. IEEE Access 2019;7:32423-32433. [doi: 10.1109/ACCESS.2019.2902217]
31. Chen T, Guestrin C. XGBoost: a scalable tree boosting system. Presented at: Proceedings of the 22nd ACM International Conference on Knowledge Discovery and Data Mining (KDD); Aug 13-17, 2016; San Francisco, CA p. 785-794.
32. Wilkinson IB, McEniery CM, Schillaci G, et al. ARTERY Society guidelines for validation of non-invasive haemodynamic measurement devices: part 1, arterial pulse wave velocity. ARTRES 2010;4(2):34. [doi: 10.1016/j.artres.2010.03.001]
33. Kwak N. Input feature selection by mutual information based on Parzen window. IEEE Trans Pattern Anal Machine Intell 2002 Dec;24(12):1667-1671. [doi: 10.1109/TPAMI.2002.1114861]

Abbreviations

baPWC: brachial-ankle pulse wave velocity
cfPWV: carotid-femoral pulse wave velocity
CVD: cardiovascular disease
ECG: electrocardiography
FDPPG: first-order derivative photoplethysmography
PAT: pulse arrival time
PPG: photoplethysmography
P2O: peak to the next onset
PWV: pulse wave velocity
RMSE: root-mean-square error
SDPPG: second-order derivative photoplethysmography
SI: stiffness index
WPD: weighted pulse decomposition
XGBoost: extreme gradient boosting

Edited by T Leung; submitted 06.06.24; peer-reviewed by R Guo, X Xing; revised version received 05.06.25; accepted 06.06.25; published 26.08.25.

Please cite as:
Ho CI, Yen CH, Li YC, Huang CH, Guo JW, Tsai PY, Lin HJ, Wang TD
Estimation of Brachial-Ankle Pulse Wave Velocity With Hierarchical Regression Model From Wrist Photoplethysmography and Electrocardiographic Signals: Method Design
JMIR Biomed Eng 2025;10:e58756
URL: https://biomedeng.jmir.org/2025/1/e58756
doi:10.2196/58756

Influence of Pre-Existing Pain on the Body's Response to External Pain Stimuli: Experimental Study

Burcu Ozek, PhD; Zhenyuan Lu, PhD; Srinivasan Radhakrishnan, PhD; Sagar Kamarthi, PhD

Mechanical and Industrial Engineering Department, Northeastern University, 360 Huntington Avenue, Boston, MA, United States

Corresponding Author:
Sagar Kamarthi, PhD
Mechanical and Industrial Engineering Department, Northeastern University, 360 Huntington Avenue, Boston, MA, United States

Abstract

Background: Accurately assessing pain severity is essential for effective pain treatment and desirable patient outcomes. In clinical settings, pain intensity assessment relies on self-reporting methods, which are subjective to individuals and impractical for noncommunicative or critically ill patients. Previous studies have attempted to measure pain objectively using physiological responses to an external pain stimulus, assuming that the participant is free of internal body pain. However, this approach does not reflect the situation in a clinical setting, where a patient subjected to an external pain stimulus may already be experiencing internal body pain.

Objective: This study investigates the hypothesis that an individual's physiological response to external pain varies in the presence of preexisting pain.

Methods: We recruited 39 healthy participants aged 22 - 37 years, including 23 female and 16 male participants. Physiological signals, electrodermal activity, and electromyography were recorded while participants were subject to a combination of preexisting heat pain and cold pain stimuli. Feature engineering methods were applied to extract time-series features, and statistical analysis using ANOVA was conducted to assess significance.

Results: We found that the preexisting pain influences the body's physiological responses to an external pain stimulus. Several features—particularly those related to temporal statistics, successive differences, and distributions—showed statistically significant variation across varying preexisting pain conditions, with *P* values <.05 depending on the feature and stimulus.

Conclusions: Our findings suggest that preexisting pain alters the body's physiological response to new pain stimuli, highlighting the importance of considering pain history in objective pain assessment models.

(JMIR Biomed Eng 2025;10:e70938) doi:10.2196/70938

KEYWORDS

pain measurement; sensors; physiological signals; hypothesis testing; pain assessment; ANOVA

Introduction

Accurate pain assessment is vital for ensuring proper treatment and helping patients receive the necessary care to reduce discomfort and prevent complications. Yet, current pain assessment tools and methods, which rely on patients' description of their pain using scales or descriptive measures, often fall short of clinical expectations [1]. These methods are ineffective for noncommunicative patients, such as infants or critically ill patients under sedation or mechanical ventilation. They are also inherently subjective, as pain perception varies widely between individuals [2-5]. These limitations increase the risk of misdiagnosis and mistreatment, highlighting the need for more objective and reliable pain assessment methods [6,7].

To address the limitations of self-reported pain assessments, physiological signals offer a promising alternative. Signals such as skin conductance, heart rate, and muscle activity provide objective data that can reflect the body's response to pain. Unlike self-reporting, physiological signals do not depend on a patient's ability to communicate, making them particularly suitable for critically ill or noncommunicative patients. By monitoring these signals in real-time, health care providers can gain an accurate and continuous understanding of a patient's pain levels, paving the way for timely and appropriate interventions. This shift toward objective, data-driven pain assessment can help reduce the variability and inaccuracies associated with traditional methods, enhancing health care providers' assessments [8,9].

Several studies have explored data-driven approaches for assessing pain through physiological signals [10-12]. These studies primarily collected data such as skin conductance, electromyography (EMG), electrocardiography, and electroencephalography during controlled pain stimuli experiments [9,13-15]. The BioVid Heat Pain Database is one of the most well-known, aiming to differentiate between various pain levels by analyzing physiological responses to heat pain

[9]. Other studies, like Rojas et al [16] and Lin et al [14], also gathered data from participants exposed to heat or cold stimuli, applying machine learning techniques to classify pain levels. These studies have demonstrated the potential of physiological signals for objective pain assessment and established valuable datasets for pain assessment research [9,14,17,18].

While the aforementioned studies provide promising results, they mainly focus on healthy participants responding to a single type of externally induced pain stimulus. One crucial factor that remains underexplored is the impact of preexisting conditions, such as chronic pain, postsurgical pain, or injury pain, that a patient is experiencing when the patient is administered an external pain stimulus. A few studies have investigated different patient populations, such as patients with chronic pain (back pain and shoulder pain) [11,19-22], patients in postsurgery [23], patients who are injured [24], patients with orthopedic trauma [25], patients with musculoskeletal trauma [26], and patients with cancer (eg, breast cancer [27]). These studies have provided insights into pain assessment in these populations, but they have not fully explored how preexisting pain interacts with new pain stimuli in terms of physiological responses.

Although the literature has begun exploring objective pain assessment for a single source of external pain stimuli, insights from medical research reveal that preexisting pain influences responses to new pain stimuli, underscoring the importance of considering preexisting pain. Sacco et al [20] found that individuals without chronic pain (without preexisting pain) exhibit an adaptive response to acute pain (new pain) by activating internal pain regulation mechanisms, including the release of natural painkillers and an increase in blood pressure, which temporarily reduces sensitivity. However, in patients with chronic pain, this adaptive mechanism can become disrupted, leading to heightened sensitivity to both acute and chronic pain. Similarly, Moscato et al [22] found that the autonomic signals of patients with chronic low back pain show differences compared to those of healthy individuals, both at rest and when subjected to a noxious stimulus, as evaluated through a set of physiological indicators. Lee et al [26] showed that preexisting pain can impact specific biomarkers, such as IL−1β, affecting how the body processes musculoskeletal trauma as a new pain. Raza et al [27] also found that women with chronic breast pain experienced more severe postoperative pain, highlighting preexisting pain as a predictor of adverse pain outcomes. In patients with trauma, Fetzh et al [24] observed that preexisting pain serves as a significant predictor for long-term pain following severe injury, emphasizing the complex interaction between pain history and physiological responses.

Although chronic pain is often referenced in the literature, the goal of this study is neither to simulate nor to assess chronic pain specifically. Instead, we use “preexisting pain” as a broader effect that can include various types of ongoing pain, such as postsurgical pain, injury-related pain, or other chronic and nonchronic conditions. Our aim is to investigate how any form of preexisting pain—regardless of origin—might influence the physiological response to a new external pain stimulus.

Our hypothesis is that preexisting pain significantly alters physiological responses to new pain stimuli. For instance, patients with chronic pain or postsurgical pain may show distinct physiological signals—such as changes in skin conductance or EMG—compared to healthy individuals when encountering new pain. To test this hypothesis, we conducted an experimental study examining how different levels of preexisting pain influence physiological responses to new pain stimuli. Understanding these responses could lead to accurate and personalized pain assessments.

In our experiments, we designated “heat pain” as a form of preexisting pain and “cold pain” as a new external stimulus. Heat pain and cold pain were studied at 3 levels: zero, low, and high. We conducted experiments with 9 combinations of no-heat, low-heat, high-heat, no-cold, low-cold, and high-cold pain. We recorded electrodermal activity (EDA) and EMG as time series data during these experimental conditions. Following data collection, we used feature engineering methods to extract features from these time series. We identified distributions, simple temporal statistics, linear and nonlinear autocorrelation, successive differences, and fluctuation analysis as pain-sensitive features. Next, we applied an ANOVA test to investigate whether physiological responses to cold pain stimuli exhibit statistical differences across three levels of preexisting heat pain. By analyzing variations in EDA and EMG features across different pain exposure levels, we aim to gain insights into how preexisting pain modulates the body’s response to new pain.

The aim of this study is to investigate how varying levels of preexisting heat pain affect the physiological response to new cold pain stimuli, using EDA and EMG signals as objective markers.

To our knowledge, this work represents the first experimental study that explores the EDA and EMG features that exhibit statistically significant differences across varying preexisting heat pain levels in response to an external stimulus.

Methods

Ethical Considerations

The research protocol was approved by the Northeastern University Institutional Review Board (IRB #22-11-06). The methods for this study adhered to the guidelines outlined in the Belmont Report. Northeastern University holds a Federal Wide Assurance with the US Department of Health & Human Services, ensuring our compliance with the principles of the Common Rule, 45 CFR 46. Before the experiment, the researcher orally explained the experimental procedure to each participant, the participant’s role, and other relevant information. In addition, the researcher presented each participant with a written consent form to read. The researcher obtained written informed consent from each participant before commencing the experiment. The research team kept participants’ data confidential and anonymized, securely storing all data with access limited to the research team only. No identifying information was included in the manuscript or any related materials. Participants were compensated with a gift card.

Participants

In total, 39 participants were recruited, with 31 completing the experiments. The remaining 8 participants chose not to continue the experiment due to discomfort from the heat pain. The study included 23 female and 16 male participants, with ages ranging from 22 to 37 years, with an average age of 26.1 (SD 3.57) years. All participants were healthy, and none reported experiencing pain before the experiment.

Inclusion and Exclusion Criteria

Participants were recruited from the Northeastern University community, including students, faculty, and staff. Inclusion criteria required participants to be between 18 and 50 years of age, in good general health, and not currently experiencing chronic pain or other medical conditions that could interfere with physiological responses. Only English-speaking individuals were included to ensure clear communication and understanding of study procedures. Pregnant individuals were excluded from participation to ensure their comfort and to avoid the introduction of additional physiological variability. There were no exclusion criteria related to gender, race or ethnicity, socioeconomic status, or literacy level.

Measured Physiological Signals

This study examined two physiological signals, EDA and EMG, to capture responses to pain stimuli.

Electrodermal Activity (EDA)

EDA serves as an indicator of neurocognitive stress through changes in the skin's electrical conductance [28]. Closely linked to the sympathetic branch of the autonomic nervous system, EDA can sense and transmit information about environmental changes, including temperature, pressure, and pain [29-31]. Consequently, EDA reflects emotional and cognitive states, making it a valuable physiological marker across various applications [32].

During emotional arousal or cognitive stress, sweat gland stimulation induces fluctuations in skin conductance, measured by EDA. These changes, largely beyond conscious control, capture subconscious physiological responses to emotions and stress, providing an objective means of assessing an individual's state [33].

In pain assessment, EDA plays a crucial role by offering a quantitative and objective measure of physiological responses to pain. It provides valuable insights into pain intensity, complementing self-reporting to enhance pain assessment accuracy in research and clinical settings [28,34]. EDA encompasses data related to both slow shifts (tonic component) and the signal's rapid alterations (phasic changes). Our analysis focused on gathering information from the tonic component, specifically skin conductance level.

Electromyography (EMG)

EMG is the electrical signal produced by skeletal muscle activity. These signals originate from motor neurons, which are integral components of the central nervous system. Since EMG signals are a reflection of neuromuscular activity, they find application in the diagnosis of conditions such as muscle injuries, nerve damage, and muscle dysfunction arising from neurological and muscular disorders [35-37]. EMG is an excellent choice for developing an objective pain assessment tool because of its unique ability to measure muscle activity directly. It allows real-time monitoring of muscle responses to understand pain intensity, location, and characteristics [14,38,39].

Design of the Experiment

The physiological data were collected using the BIOPAC MP160 data acquisition and analysis systems with AcqKnowledge software (BIOPAC Systems, Inc). Smart amplifiers recorded EMG and EDA. Heat stimulation was delivered using OCOOPA Hand Warmers, which offered two temperature settings: 37 and 45 °C. These temperatures were measured and monitored using a BIOPAC SKT (Skin Temperature) Smart Amplifier. Cold stimulation was provided through iced water, with the temperature continuously monitored using a thermometer. In these experiments, heat pain acts as preexisting pain, while cold pain acts as a new pain stimulus.

Using temperature-based modalities for both preexisting (heat) and new (cold) pain stimuli allowed us to design a consistent, safe, and replicable experimental setup. Temperature stimuli are well-established in pain research and offer practical advantages regarding ecological validity and participant safety. Moreover, the thermal approach enabled controlled comparisons of physiological responses across different pain levels while minimizing variability introduced by mechanical or electrical alternatives.

EDA data were collected using the BIOPAC EDA Smart Amplifier attached to the ring and index fingers of the participant's nondominant hand. Before attaching the sensors to the fingers, the skin was cleaned with wet wipes, and GEL101A was applied to the electrodes to improve conductivity, enhance signal quality, and reduce impedance. EMG data were acquired using the BIOPAC EMG Smart Amplifier, with three electrodes attached to the participant's nondominant forearm. The skin in the sensor placement area was prepared by cleaning it with wet wipes, followed by abrasion and application of ELPREP. GEL100 was applied to the electrodes to improve contact. To minimize motion artifacts, all cables were secured with medical tape. Hand warmers were fastened to the participant's dominant forearm using a strap. Figure 1A shows the picture of the placement of the electrodes.

Figure 1. Data acquisition setup and experimental setup for pain stimuli. (A) EDA data were gathered from the ring and index fingers of the participant's nondominant hand, while EMG data were recorded using three electrodes positioned on the participant's nondominant forearm. (B,C) Hand warmers, serving as heat pain stimuli, were fastened to the participant's dominant forearm using a strap. Cold pain stimuli were induced by iced water when participants placed their fingers or hands in the iced water, depending on the stimulus level the participant is expected to receive in the design of experiments: for low-level cold pain stimulus, participants placed fingers in the iced water, and for high-level cold pain stimulus, participants placed the hand in the iced water.

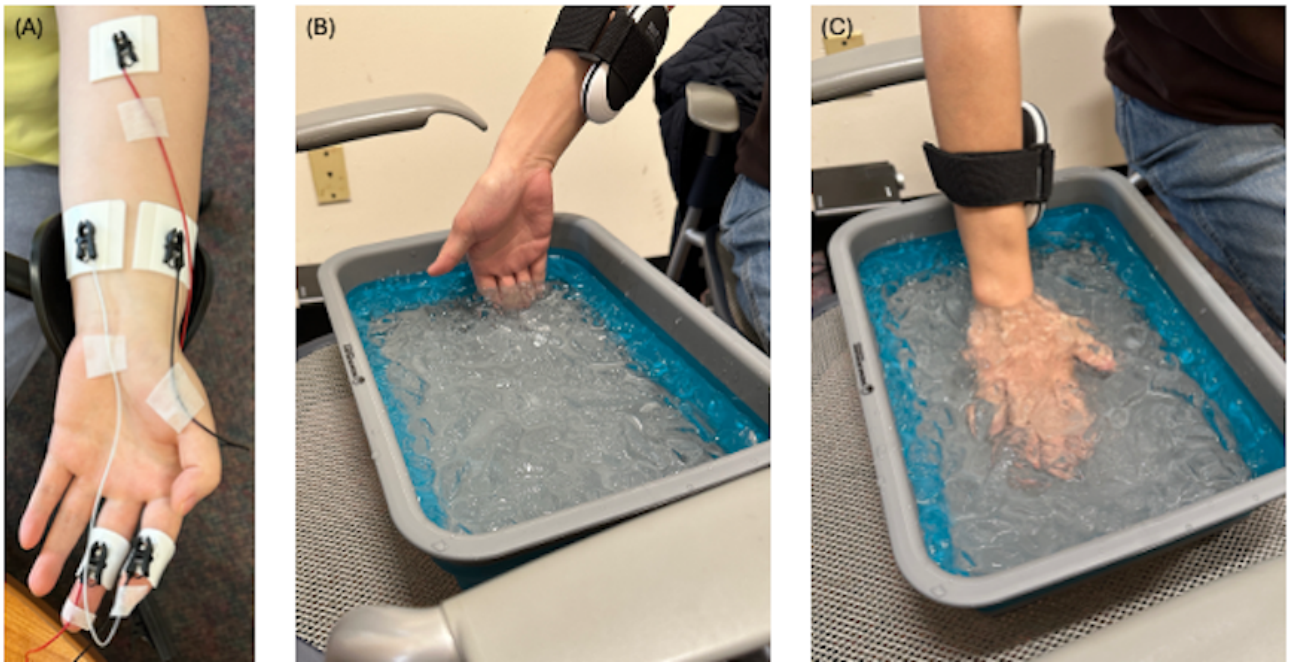

The experiment consisted of two types of pain stimuli: (1) heat pain caused by attaching hand warmers to the forearm and (2) cold pain induced by placing fingers or hands in ice water. Each type of pain had low and high levels. The heat and cold pain stimuli were applied to the dominant hand, while physiological signals were collected from the nondominant hand. At the end of each step, participants were asked to report their pain levels on a scale of 0 to 10. The participants are given a 4-minute relaxation break at the beginning of each data collection session.

We collected baseline data from each participant without inducing any type of pain stimulus. The rest of the experimental procedure consisted of two phases. In the first phase, we collected data from four steps; in Step 1, only the low-level cold pain was applied; in Step 2, only the high-level cold was applied; in Step 3, only low-level heat pain was applied; and in Step 4, only high-level heat pain was applied. In the second phase of the experiments, we applied a different combination of heat and cold pain levels to examine their combined effect in Steps 5 through 8.

The experimental procedures for the first phase involved four steps. First, the participant placed their fingers in iced water and held them there for 8 seconds, representing low-level cold pain. In the second step, they placed their dominant hand in iced water for 8 seconds, representing high-level cold pain. In the third step, using a hand warmer attached to the participant's dominant forearm, they were subjected to 37 °C heat for 1.5 minutes, which caused low-level preexisting heat pain. In the final step of the first phase, using a hand warmer attached to the participant's dominant forearm, they were subjected to 45 °C heat for 1.5 minutes, which caused high-level preexisting heat pain.

The second phase of the experiment involved four additional steps. In the fifth step of the experiment, the participant wore a hand warmer on their nondominant forearm, experiencing a temperature of 37 °C for 1.5 minutes. After 80 seconds into the heat pain stimulus, the participant placed their fingers in iced water for 8 seconds. This scenario represents the simultaneous application of low preexisting heat pain and new low cold pain. In the sixth step, the participant repeated Step 5 with the hand warmer on their nondominant forearm, but at a temperature of 45 °C. Again, after 80 seconds, they placed their fingers in iced water for 8 seconds. This scenario represents the simultaneous application of high preexisting heat pain and new low cold pain. In the seventh step, the participant wore the hand warmer on their nondominant forearm at 37 °C for 1.5 minutes. After 80 seconds had elapsed, they immersed their dominant hand in iced water for 8 seconds. This scenario represents the simultaneous application of low preexisting heat pain and new high cold pain. In the eighth and final step, the participant repeated Step 7 with the hand warmer on their nondominant forearm at 45 °C for 1.5 minutes. After 80 seconds, they immersed their dominant hand in iced water for 8 seconds. This scenario represents the simultaneous application of high preexisting heat pain and new high cold pain.

Figure 1B,C illustrates how the hand warmer is positioned on the forearm and how the fingers or hand are placed in the ice water.

Signal Processing

Both EDA and EMG signals were recorded at a data acquisition rate of 2000 samples per second (2 kHz). For EDA, a low-pass filter with a 1.0 Hz frequency cutoff was used to eliminate high-frequency noise [30,40].

We processed EMG signals through a comb bandstop transformation to eliminate interference from the power line frequency (50 Hz) [41]. The comb bandstop transformation aims to effectively suppress or eliminate interference originating from the power line frequency (50 Hz), ensuring a relatively noise-free EMG signal for analysis and interpretation. Subsequently, a finite impulse response bandpass filter was applied, specifying a low-frequency cutoff at 28 Hz and a high-frequency cutoff at 500 Hz [42]. This step was implemented to filter out both high and low artifacts, such as motion artifacts, and to focus on the EMG signal within the frequency range of 28 to 500 Hz.

Recognizing that the EMG signal centers around 0, a rectified version was generated by averaging samples in sets of 100. This approach makes analysis easy by eliminating negative values and retaining the magnitude of the signal.

To analyze EMG further, the root mean square (RMS) was calculated using a window size of 100 samples. This measurement meaningfully represents the signal's characteristics because EMG is centered around 0.

Feature Extraction

In this study, we derived features from EDA and EMG using the "Canonical Time-series Characteristics" outlined by Lubba et al [43]. These features encompass fundamental statistical metrics of time-series data, stationarity measures, entropy, linear correlations, nonlinear time-series analysis techniques, linear and nonlinear model parameters, predictive capabilities, and fits. Specifically, we identified the subset of 22 features highlighted as the most informative by Lubba et al [43]. These features are listed in Table 1. Following all the data processing and extraction steps, we obtained 22 features from EDA, EMG, rectified EMG, and RMS of EMG signals; this resulted in a total of 22×4=88 features. Then, we applied z-transformation to normalize all features for each participant, using the participant-specific mean and SD.

Table . Time-series feature categories and descriptions using the "Canonical Time-series Characteristics" defined by Lubba et al [43].

Feature category	Features
Distribution	• Mode of *z*-scored distribution (5-bin histogram) • Mode of *z*-scored distribution (10-bin histogram)
Simple temporal statistics	• The longest period of consecutive values above the mean • Time intervals between successive extreme events above the mean • Time intervals between successive extreme events below the mean
Linear autocorrelation	• The first 1/e crossing of the autocorrelation function • The first minimum of the autocorrelation function • Total power in the lowest fifth of frequencies in the Fourier power spectrum • Centroid of the Fourier power spectrum • Mean error from a rolling 3-sample mean forecasting
Nonlinear autocorrelation	• Time-reversibility statistic, $(x_{t+1}-x_t)^3{}_t$ • Auto mutual information, $m=2$, $\tau=5$ • The first minimum of the auto-mutual information function
Successive differences	• Proportion of successive differences exceeding 0.04 σ (Mietus et al [44]) • The longest period of successive incremental decreases • Shannon entropy of two successive letters in equiprobable 3-letter symbolization • Change in correlation length after iterative differencing • Exponential fit to successive distances in 2D embedding space
Fluctuation analysis	• The proportion of slower timescale fluctuations that scale with DFA[a] (50% sampling) • The proportion of slower timescale fluctuations that scale with linearly rescaled range fits
Others	• Trace of covariance of the transition matrix between symbols in the 3-letter alphabet • Periodicity measure (Wang et al [45])

[a]DFA: detrended fluctuation analysis.

Statistical Testing

The initial analysis aims to identify statistically significant features for class differentiation. This includes using the ANOVA test, which assesses variations among the means of various groups. It is applied in various situations to ascertain whether there are any significant differences between the means of the groups [46,47]. The null hypothesis asserts that the means

of the groups are the same, while the alternative hypothesis posits that the means are not equal.

(1)H0:μ1=μ2H1:μ1≠μ2

We reject the null hypothesis if the calculated *P* value is less than the chosen significance level, say, .05.

We used ANOVA to assess the statistical differences in the means of extracted time series features derived from physiological signals. The sample comprises 31 observations. The normality of data, which is a requisite for ANOVA, is confirmed through the Kolmogorov-Smirnov Test for normality of data and examination of quantile-quantile plots (Q-Q plots) for each individual feature. A significance level of .05 is set for the ANOVA test, which is conducted as a 2-tailed analysis.

Results

The following sections present the results of statistical comparisons of EMG and EDA signal features across different combinations of heat and cold pain levels.

Significant Features in the Presence and Absence of Pre-existing Pain

Table 2 summarizes the statistically significant differences (*P*<.05) in EMG and EDA features across experimental groups. Each row corresponds to a specific hypothesis involving two groups. For example, the first row compares Group 1 (participants who experienced low-level cold pain without preexisting heat pain) with Group 2 (participants who experienced the same low-level cold pain while also experiencing mild preexisting heat pain). This comparison examines feature-level differences across EMG and EDA signals under these two conditions.

Table . Statistically significant feature categories and the average *P* values of features within each category for different hypotheses, aiming to study the influence of the presence or absence of pre-existing pain on external pain stimuli between symbols in the 3-letter set.

Groups	EMG,[a] (*P* value)	RMS[b] of EMG, (*P* value)	Rectified EMG, (*P* value)	EDA,[c] (*P* value)
• Group 1: low-level cold pain without any pre-existing pain • Group 2: low-level cold pain with mild pre-existing heat pain	• Linear autocorrelation (<.001) • Successive differences (.002) • Distribution (.02) • Others (.006) • Statistics (.02)	• Linear autocorrelation (.004) • Successive differences (.01)	• Linear autocorrelation (.003) • Successive differences (.001)	• Statistics (.02)
• Group 1: low-level cold pain without any pre-existing pain • Group 2: low-level cold pain with severe pre-existing heat pain	• Linear autocorrelation (.004) • Successive differences (.005) • Others (.02) • Statistics (.02)	• Linear autocorrelation (.02)	• Linear autocorrelation (.02) • Successive differences (.03)	• Statistics (.02) • Others (.04)
• Group 1: high-level cold pain without any pre-existing pain • Group 2: high-level cold pain with mild pre-existing heat pain	• No significant features	• No significant features	• No significant features	• Successive differences (.03)
• Group 1: high-level cold pain without any pre-existing pain • Group 2: high-level cold pain with severe pre-existing heat pain	• No significant features	• No significant features	• Successive differences (.03)	• Others (.03)

[a]EMG: electromyography.

[b]RMS: root mean square.

[c]EDA: electrodermal activity.

For low-level cold pain without any pre-existing pain (Group 1) versus low-level cold pain with mild pre-existing heat pain (Group 2), significant differences were observed in EMG features related to linear autocorrelation, including the "first minimum and the first 1/e crossing of the autocorrelation function." In the EDA signal, temporal statistics, specifically "time intervals between successive extreme events," showed statistically significant differences.

For low-level cold pain without any pre-existing pain (Group 1) versus low-level cold pain with severe pre-existing heat pain (Group 2), EMG features related to linear autocorrelation, such as the first minimum and 1/e crossing of the autocorrelation function, were significantly different. The EDA features that

showed the differences included “time intervals between successive extreme events” and the “longest period of consecutive values above the mean.”

For high-level cold pain without any pre-existing pain (Group 1) versus high-level cold pain with mild pre-existing heat pain (Group 2), the distinguishing features were found in the EDA signal’s successive differences, particularly the “longest period of successive incremental decreases.”

For high-level cold pain without any pre-existing pain (Group 1) versus high-level cold pain with severe pre-existing heat pain (Group 2), statistically significant differences were observed in the rectified EMG signal for features related to successive differences, including the “change in correlation length after iterative differencing” and the “longest period of successive incremental decreases.” In the EDA signal, differences were observed in the “trace of covariance of the transition matrix between symbols in the 3-letter set.”

Significant Features in the Mild and Severe Cases of Pre-existing Pain

Table 3 presents the signals and their respective features that exhibit statistically significant differences ($P<.05$) among the groups. In this section, two hypotheses are investigated. The first hypothesis aims to compare physiological signals to assess the influence of mild and severe pre-existing pain in Groups 1 and 2; Group 1 includes signals from participants subjected to low-level cold pain while already experiencing mild pre-existing heat pain; Group 2 includes signals from participants subjected to low-level cold pain while already experiencing severe pre-existing heat pain. The second hypothesis involves comparing the groups to assess the impact of mild and severe pre-existing heat pain on participants when they are subjected to high-level cold pain. Figure 2 visually illustrates the distribution of the most statistically significant features for each of the two hypotheses.

Table . Statistically significant feature categories and individual features for distinguishing the influence of varying levels of pre-existing pain on the response to low and high levels of cold pain.

Hypotheses and signal	Feature category	Feature (*P* value)
Group 1: low-level cold pain with mild pre-existing heat pain; Group 2: low-level cold pain with severe pre-existing heat pain		
EMG[a]	Distribution	Mode of *z*-scored distribution (10-bin histogram; .03)
RMS[b] of EMG	Successive differences	Longest period of successive incremental decreases (.01)
RMS of EMG	Statistics	Longest period of consecutive values above the mean (.03)
Group 1: high-level cold pain with mild pre-existing heat pain; Group 2: high-level cold pain with severe pre-existing heat pain		
Rectified EMG	Successive differences	Longest period of successive incremental decreases (.007)
Rectified EMG	Statistics	Longest period of consecutive values above the mean (.01)
EMG	Distribution	Mode of *z*-scored distribution (10-bin histogram; .03)
EMG	Statistics	Time intervals between successive extreme events below the mean (.04)
RMS of EMG	Statistics	Time intervals between successive extreme events below the mean (.005)
RMS of EMG	Statistics	Time intervals between successive extreme events above the mean (.009)
Rectified EMG	Statistics	Time intervals between successive extreme events below the mean (.01)
Rectified EMG	Statistics	Time intervals between successive extreme events above the mean (.01)
Rectified EMG	Successive differences	Change in correlation length after iterative differencing (.03)
EDA[c]	Statistics	Time intervals between successive extreme events below the mean (.01)
EDA	Others	Trace of covariance of transition matrix (.02)

[a]EMG: electromyography.

[b]RMS: root mean square.

[c]EDA: electrodermal activity.

Figure 2. Distribution of features with the influence of pre-existing heat pain: (A,B) Illustrate the probability density of two significant EMG features under low- and high-level cold pain conditions. (C,D) Present the corresponding boxplots for each feature, comparing the mild and severe pre-existing pain conditions. EMG: electromyography; RMS: root mean square.

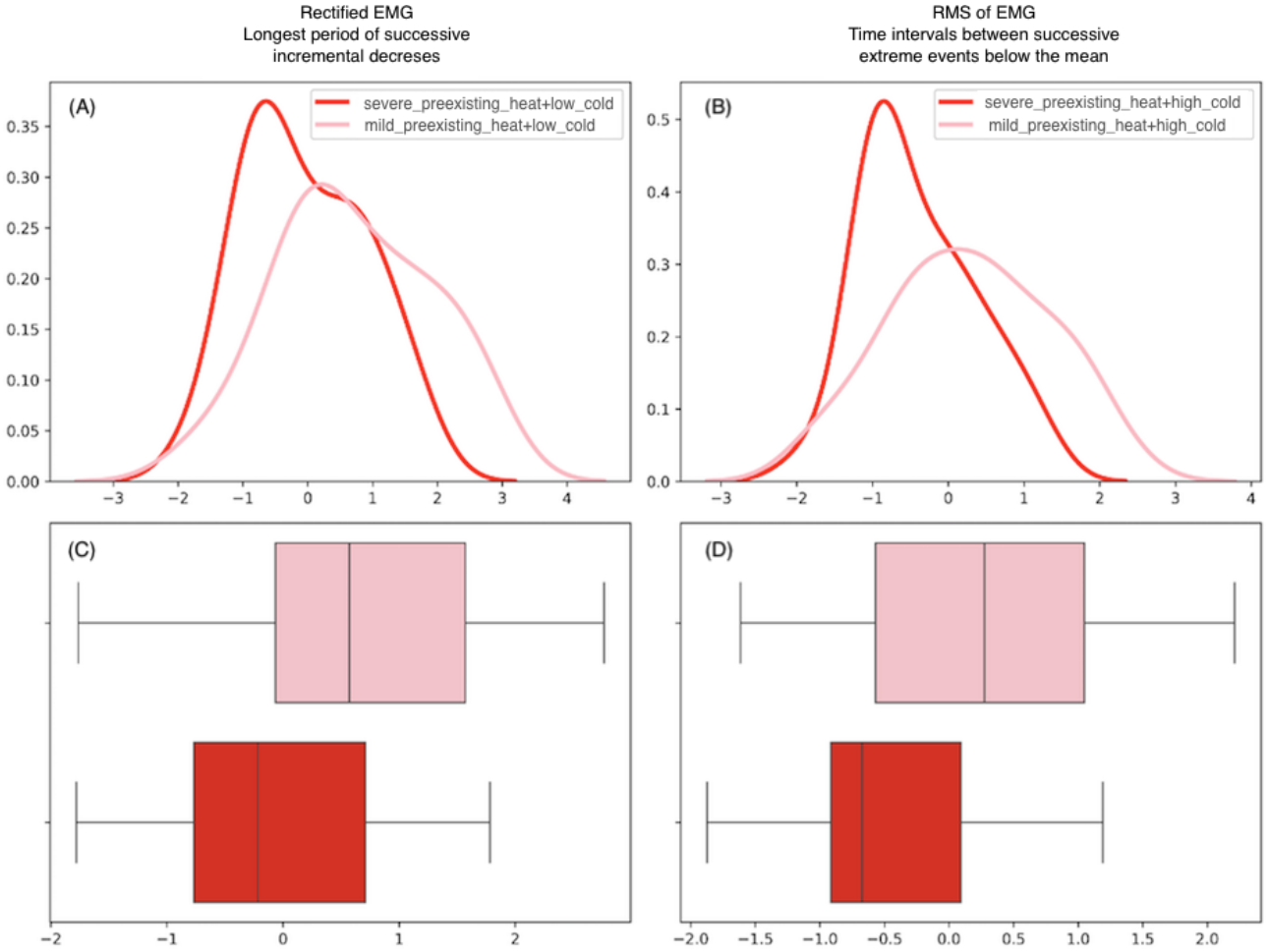

Hypothesis 1 examines the influence of mild and severe pre-existing heat pain on the body's response to low-level cold pain. Significant differences were observed in the EMG signal's "mode of *z*-scored distribution." RMS of EMG showed variations in successive differences and statistics, specifically related to "the longest period of incremental decreases" and "the longest period of consecutive values above the mean." Similar patterns were found in the rectified EMG signal.

Hypothesis 2 investigates the influence of mild and severe pre-existing heat pain on the body's response to high-level cold pain. The "mode of *z*-scored distribution" of EMG exhibited significant differences across the groups. RMS of EMG also showed variations in statistics related to "time intervals between successive extreme events below and above the mean." Rectified EMG signals differed in features pertaining to successive differences and statistics. Additionally, EDA signals showed significant differences in the "trace of covariance of the transition matrix."

Heat and Cold Pain Interactions

This section presents a response surface analysis using marginal mean plots and surface plots. It examines how varying levels of heat and cold pain affect two statistically significant features: the rectified EMG's "longest period of successive incremental decreases" and the RMS of EMG's "time intervals between successive extreme events below the mean." Figure 3A and C show the rectified EMG response values, while Figure 3B and D display the RMS of EMG response values. The analysis includes pain levels coded as 0 (no pain), 1 (mild pain), and 2 (severe pain).

Figure 3. Interaction effects of pre-existing heat pain and new cold pain on EMG features. (A,B) Marginal means plots illustrating how rectified EMG and RMS values vary across different levels of heat pain (0, 1, 2) and cold pain (0, 1, 2). (C,D) Surface plots depicting the variation in responses under various combinations of heat and cold pain levels. EMG: electromyography; RMS: root mean square.

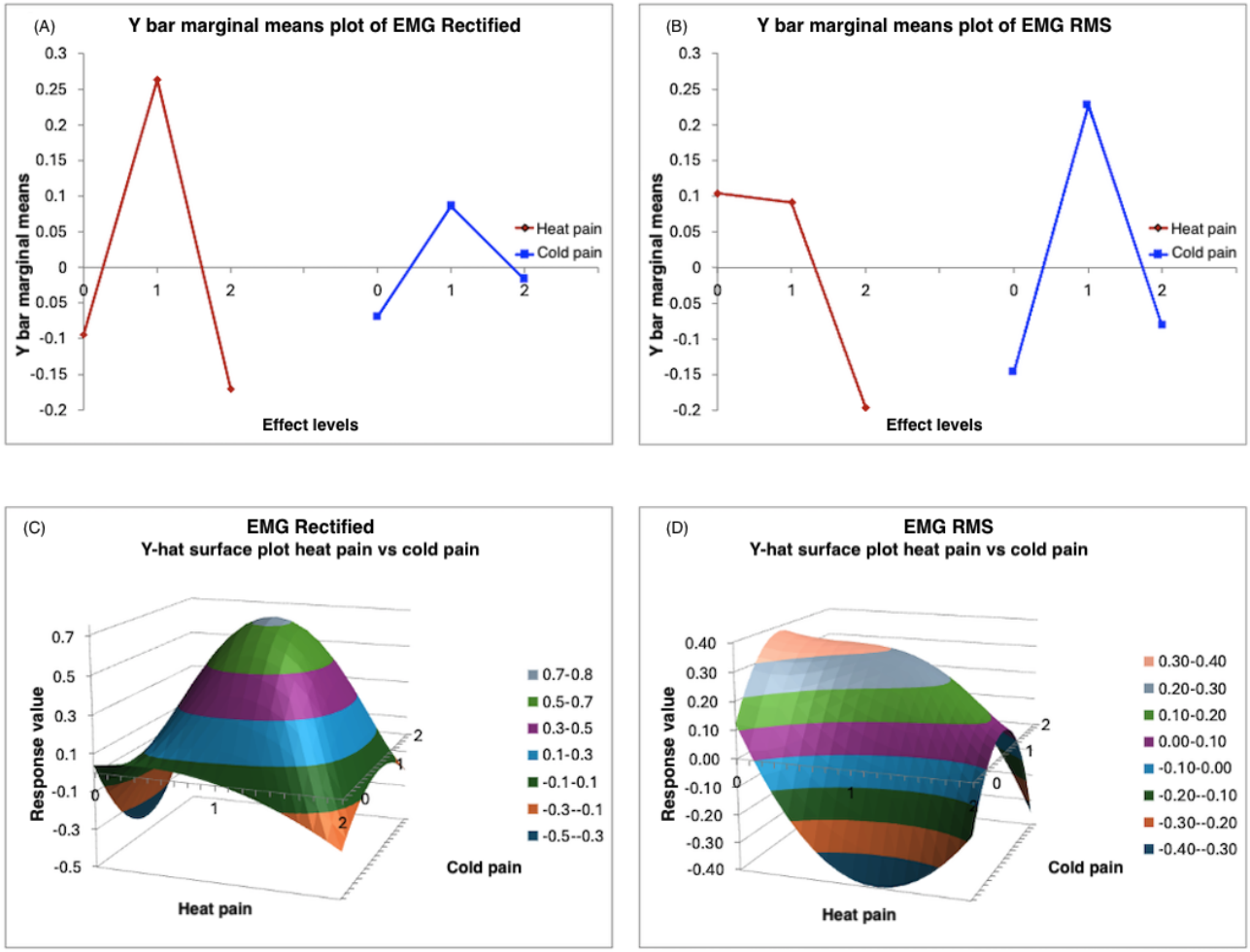

Discussion

Principal Findings

This study was guided by the hypotheses that (1) pre-existing body pain alters the physiological response to a new pain stimulus relative to the physiological response in the absence of pre-existing pain, and (2) pre-existing pain of different intensities produces distinguishably different physiological patterns in response to a new pain stimulus. The use of multimodal physiological signals, EDA, and EMG provides insight into the underlying mechanisms and supports the potential for objective, signal-based pain assessment in complex pain scenarios.

This study found that pre-existing heat pain significantly influences physiological responses to new cold pain stimuli, as indicated by features from EDA and EMG, particularly successive differences, temporal statistics, and distribution features, demonstrating noticeable sensitivity to varying pain combinations.

Comparative Analysis: Features Sensitive to the Presence and Absence of Pre-existing Pain

This section evaluates how the presence or absence of pre-existing heat pain influences physiological responses when the body encounters a cold pain stimulus. EMG signals exhibit significant variation across groups, particularly in features such as “linear autocorrelation” and “successive differences,” while EDA signals indicate differences through statistical features.

When an external low-level cold pain is applied, the pre-existing heat pain, mild or severe, consistently leads to marked changes in both EMG and EDA signals. In the EMG signal, features such as the “first minimum and the first 1/e crossing of the autocorrelation function” capture distinct temporal characteristics of muscle activity. The first minimum identifies a key point of dissimilarity, while the 1/e crossing reflects the timescale at which the signal’s autocorrelation declines to approximately 36.8% of its peak. In the EDA signal, the “time intervals between successive extreme events” and the “longest period of consecutive values above the mean” emerge as distinguishing features. These results indicate that low-level cold pain elicits prominently different physiological features in the presence and absence of pre-existing heat pain.

When a high-level cold pain stimulus is applied, the EDA signal’s sensitivity to successive differences, particularly the “longest period of successive incremental decreases,” emerges as a distinguishing feature. This feature identifies continuous patterns where EDA consistently decreases from one point to the next and the trace of covariance of the “transition matrix

between symbols in the 3-letter set." This method involves encoding and simplifying the EDA signal into sequences, allowing for the analysis of how these sequences change and relate to each other over time, highlighting its utility in capturing autonomic dynamics influenced by layered pain conditions. Similarly, rectified EMG features tied to successive differences are important: the "change in correlation length after iterative differencing" and the "longest period of successive incremental decreases" further underscore the complementary roles of multimodal physiological measurements.

High-intensity cold pain appears to overshadow the physiological responses associated with pre-existing heat pain. Under these conditions, significant differences are limited and primarily observed in EDA and rectified EMG signals. The overwhelming nature of high-level cold pain reduces the detectability of pre-existing pain effects, making it difficult to distinguish their individual contributions to the physiological response. Despite this, certain features remain sensitive. In the EDA signal, successive differences, particularly the "longest period of successive incremental decreases," identify continuous patterns where EDA consistently decreases from one point to the next. Additionally, the "trace of covariance of the transition matrix between symbols in the 3-letter" set captures how patterns evolve over time, offering insights into autonomic dynamics under layered pain conditions. Similarly, rectified EMG features related to successive differences, including the "change in correlation length after iterative differencing" and the "longest period of successive decreases," emphasize the value of combining multimodal physiological measurements to capture subtle effects that may persist despite dominant pain stimuli.

Together, these findings suggest that the influence of pre-existing heat pain on the body's physiological response is more discernible when cold pain is mild, particularly through EMG and EDA signals. In contrast, high-intensity cold pain may mask these effects, making it difficult to detect the physiological changes due to pre-existing pain. Understanding these interactions between physiological responses due to external and pre-existing pains is essential for interpreting pain states in complex and overlapping pain scenarios. The presence of statistically significant and diverse features supports the notion that pre-existing heat pain has a measurable impact on physiological responses.

Comparative Analysis: Significant Features in the Mild and Severe Cases of Pre-existing Pain

This section examines how the severity of pre-existing heat pain, ranging from mild to severe, influences the body's physiological response when exposed to a new cold pain stimulus. The findings reveal distinct alterations in EMG and EDA signals that differentiate these pain intensities.

When participants experience low-level cold pain while the body is already encountering varying degrees of pre-existing heat pain, the physiological responses captured through EMG are particularly sensitive to the severity of pre-existing heat pain. Features like "mode of *z*-score distribution," which refers to the value or range of values that occur most frequently, indicate shifts in the most dominant muscle activity patterns. Additionally, the RMS of EMG shows differences in features related to successive differences and statistics, specifically the "longest period of incremental decreases" and the "longest period of consecutive values above the mean." The first feature refers to the duration in the time series where the EMG signal's RMS consistently decreases incrementally. In simpler terms, it identifies the most extended continuous period during which the RMS values decrease step by step. The second feature pertains to the time series duration in which the EMG signal's RMS values remain consistently above the mean. This duration captures the longest continuous segment where the RMS values are consistently higher than the average. These features are further supported by similar patterns observed in the rectified EMG signal, reinforcing the robustness of these distinctions.

In the high-level cold pain condition, EMG signals continue to reveal statistically significant differences across pre-existing pain intensities. The "mode of the *z*-scored distribution" emerges as an important marker, indicating distinctive patterns in muscle activity under mild and severe pre-existing heat pain conditions. Analysis of the RMS of EMG signals unveils notable variations in statistics involving "time intervals between successive extreme events above or below the mean." This observation highlights the complex temporal dynamics associated with the interaction of high-level cold pain and the severity of pre-existing pain. The distribution of rectified EMG signals further reinforces these findings, highlighting distinct patterns in successive differences and statistics, which contribute to the differentiation of the influence of different pre-existing pain conditions. Beyond EMG, EDA signals also contribute to this differentiation. The "trace of the covariance of the transition matrix" emerges as a key feature. This reveals variation in how these patterns evolve over time under different pre-existing pain conditions. The inclusion of EDA signals in our analysis deepens our understanding of physiological responses to the influence of varying pre-existing pain intensities.

The results of this study highlight that the body exhibits distinct responses to cold pain stimuli when experiencing mild versus severe pre-existing heat pain. These findings highlight the intricate relationship between pain conditions and physiological responses. The identified features within EMG and EDA signals offer valuable insights into the body's mechanisms, highlighting the influence of pre-existing pain on physiological signals.

Analysis of Heat and Cold Pain Interactions

Response surface analysis provides comprehensive insight into how varying levels of pre-existing heat pain and externally introduced cold pain interact to influence physiological responses.

Figure 3A displays the marginal means plot of the rectified EMG response. Marginal means plots illustrate the responses by considering only the level of one type of pain, independent of the levels of any other type of pain. For example, the response is the strongest when the heat pain is mild. Similarly, when considering only cold pain, the response peaks again at the mildest level of pain. The surface plot represents the interactions between the two types of pain and their effects on the response. The surface plot in Figure 3Creveals a convex shape with a peak, indicating that the rectified EMG responses reach their

highest values when both heat and cold pain are at a mild level. The plot shows that the response is low when there is no heat pain and mild cold pain, and similarly low under severe heat pain with no accompanying cold pain.

Figure 3B presents a marginal mean plot of the RMS of EMG responses. Here, it is evident that mild cold levels yield the highest response values. Both "no heat" pain and "mild heat" pain conditions result in high response values, while severe heat pain significantly reduces the RMS of EMG responses. In Figure 3D, surface plots of the RMS of EMG responses are displayed.

Notably, as heat pain increases, the RMS value decreases, reaching its peak when heat pain is absent or mild. Conversely, instances of mild heat paired with no cold pain result in the lowest RMS of EMG response values.

These patterns underscore the importance of considering multidimensional pain contexts, as overlapping pain experiences can interact in nonintuitive ways that meaningfully alter physiological signatures.

Limitations

The relatively small and homogeneous sample size, consisting of 31 healthy young adults aged 22 to 37 years, is one of the shortcomings of this study. This may limit the generalizability of the findings to broader and clinically relevant populations. Additionally, the study was conducted in a controlled laboratory environment, which may not fully replicate real-world clinical settings, thus limiting its ecological validity. While the use of fixed-intensity heat and cold stimuli was effective for controlled experimental design, it may not capture the full complexity of pre-existing pain conditions and individual pain thresholds. Furthermore, the fixed-intensity nature of these stimuli does not account for interindividual variability in pain sensitivity, which could influence physiological responses. The devices used in this study did not support personalized stimulus calibration, which we recognize as a limitation.

Future Directions

Future work is open to expanding the sample population to include individuals from diverse age groups and clinical backgrounds, particularly those experiencing chronic or postsurgical pain, to improve the generalizability of findings. Validation in real-world clinical environments is also crucial for enhancing ecological validity. To better reflect the complexity of pain experiences, future studies should explore alternative or multimodal pain induction methods beyond heat and cold stimuli and incorporate personalized calibration to account for individual pain thresholds. Additionally, expanding the range of physiological signals—such as heart rate variability, electroencephalography, and functional neuroimaging—may offer a more comprehensive understanding of the neural and autonomic correlates of pain.

This study used statistical analysis to examine the significance of physiological differences across pain conditions. In future work, we will further explore machine learning models to analyze physiological responses to new external pain stimuli. This approach will enable us to assess the intensity of pre-existing pain caused by chronic conditions, injuries, or surgeries. By integrating machine learning, we aim to develop predictive models that can objectively assess pain intensity and support personalized, effective pain management, particularly in clinical settings where patients are unable to verbally communicate their pain levels.

Conclusions

Accurate pain assessment is crucial for the correct diagnosis and effective treatment of many diseases. While existing literature has developed tools for estimating pain levels based on physiological responses, these studies often focus on healthy individuals experiencing acute pain, overlooking the potential influence of pre-existing conditions, such as postsurgical pain, chronic pain, and physical discomfort, on the physiological signals triggered by acute pain. Acknowledging this factor is essential, as individuals may respond differently to new pain stimuli depending on the intensity of their pre-existing pain.

This study examined the impact of pre-existing heat pain through experimental research when participants were exposed to cold pain stimuli. We used heat pain as the pre-existing pain condition, cold pain as the new pain stimulus, and EMG and EDA as physiological signals. By using statistical tests, we observed significant differences in specific EDA and EMG signal features across varying levels of pre-existing heat pain and new cold pain combinations. Notably, simple temporal statistics (the most extended period of consecutive values, time intervals between successive extreme events), successive differences (change in correlation length after iterative differencing), distribution (mode of *z*-scored distribution), and autocorrelation (the first 1/e crossing of the autocorrelation function) emerged as primary feature categories that significantly varied across pre-existing heat pain and new cold pain intensity combinations.

Our investigation into the differences in EMG and EDA signals in the presence of different levels of pre-existing heat pain has revealed valuable insights. The distinction between the absence of pre-existing pain and the presence of mild or severe pre-existing heat pain, particularly when stimulated with new low-level cold pain, highlighted statistically significant differences in both EMG and EDA signals. Notably, when we switched to high-level cold pain, EDA emerged as a more reliable indicator of variation in pre-existing pain than EMG. During high-level cold pain, the time series features of "successive differences" proved to be effective indicators of the level of the pre-existing pain. Furthermore, our analysis of mild and severe pre-existing heat pain scenarios revealed that EMG exhibited statistically significant differences, particularly in response to the new low-level cold pain, whereas EDA remained relatively unchanged. However, when we switched to high-level cold pain, both EMG and EDA signal features exhibited statistically significant differences. Successive difference, temporal statistics, and distribution features of time series emerged as reliable indicators of the pre-existing heat pain in these cases. These findings shed light on the changes in EMG and EDA signals across different levels of pre-existing pain, advancing our understanding of physiological responses in pain assessment.

Data Availability

The datasets generated or analyzed during this study are available from the corresponding author on reasonable request.

Authors' Contributions

BO, ZL, SR, and SK designed the experiment. BO conducted the experiments, analyzed the data, and prepared the manuscript. All authors reviewed the manuscript.

Conflicts of Interest

None declared.

References

1. Huo J, Yu Y, Lin W, Hu A, Wu C. Application of AI in multilevel pain assessment using facial images: systematic review and meta-analysis. J Med Internet Res 2024 Apr 12;26:e51250. [doi: 10.2196/51250] [Medline: 38607660]
2. Liu R, Gutiérrez R, Mather RV, et al. Development and prospective validation of postoperative pain prediction from preoperative EHR data using attention-based set embeddings. NPJ Digital Med 2023 Nov 16;6(1):209. [doi: 10.1038/s41746-023-00947-z] [Medline: 37973817]
3. Ozek B, Lu Z, Radhakrishnan S, Kamarthi S. Uncertainty quantification in neural-network based pain intensity estimation. PLoS One 2024;19(8):e0307970. [doi: 10.1371/journal.pone.0307970] [Medline: 39088473]
4. Pouromran F, Radhakrishnan S, Kamarthi S. Exploration of physiological sensors, features, and machine learning models for pain intensity estimation. PLoS One 2021;16(7):e0254108. [doi: 10.1371/journal.pone.0254108] [Medline: 34242325]
5. Amidei J, Nieto R, Kaltenbrunner A, Ferreira De Sá JG, Serrat M, Albajes K. Exploring the capacity of large language models to assess the chronic pain experience: algorithm development and validation. J Med Internet Res 2025 Mar 31;27:e65903. [doi: 10.2196/65903] [Medline: 40163858]
6. Lu Z, Ozek B, Kamarthi S. Transformer encoder with multiscale deep learning for pain classification using physiological signals. Front Physiol 2023;14:1294577. [doi: 10.3389/fphys.2023.1294577] [Medline: 38124717]
7. Billot M, Ounajim A, Moens M, et al. The added value of digital body chart pain surface assessment as an objective biomarker: multicohort study. J Med Internet Res 2025 Apr 16;27:e62786. [doi: 10.2196/62786] [Medline: 40239206]
8. Ozek B, Lu Z, Pouromran F, Radhakrishnan S, Kamarthi S. Analysis of pain research literature through keyword co-occurrence networks. PLOS Digital Health 2023 Sep;2(9):e0000331. [doi: 10.1371/journal.pdig.0000331] [Medline: 37676880]
9. Walter S, Gruss S, Ehleiter H, et al. The biovid heat pain database data for the advancement and systematic validation of an automated pain recognition system. Presented at: 2013 IEEE International Conference on Cybernetics (CYBCO); Jun 13-15, 2013; Lausanne, Switzerland p. 128-131. [doi: 10.1109/CYBConf.2013.6617456]
10. Jiang M, Mieronkoski R, Syrjälä E, et al. Acute pain intensity monitoring with the classification of multiple physiological parameters. J Clin Monit Comput 2019 Jun;33(3):493-507. [doi: 10.1007/s10877-018-0174-8] [Medline: 29946994]
11. Luebke L, Gouverneur P, Szikszay TM, Adamczyk WM, Luedtke K, Grzegorzek M. Objective measurement of subjective pain perception with autonomic body reactions in healthy subjects and chronic back pain patients: an experimental heat pain study. Sensors (Basel) 2023 Oct 3;23(19):8231. [doi: 10.3390/s23198231] [Medline: 37837061]
12. Lancaster J, Mano H, Callan D, Kawato M, Seymour B. Decoding acute pain with combined eeg and physiological data. Presented at: 2017 8th International IEEE/EMBS Conference on Neural Engineering (NER); May 25-28, 2017; Shanghai, China. [doi: 10.1109/NER.2017.8008404]
13. Guo Y, Wang L, Xiao Y, Lin Y. A personalized spatial-temporal cold pain intensity estimation model based on facial expression. IEEE J Transl Eng Health Med 2021;9:4901008. [doi: 10.1109/JTEHM.2021.3116867] [Medline: 34650836]
14. Lin Y, Xiao Y, Wang L, et al. Experimental exploration of objective human pain assessment using multimodal sensing signals. Front Neurosci 2022;16:831627. [doi: 10.3389/fnins.2022.831627] [Medline: 35221908]
15. Chu† Y, Zhao X, Yao† J, Zhao Y, Wu Z. Physiological signals based quantitative evaluation method of the pain. IFAC Proc Volumes 2014;47(3):2981-2986. [doi: 10.3182/20140824-6-ZA-1003.01420]
16. Rojas RF, Huang X, Ou KL. A machine learning approach for the identification of a biomarker of human pain using fNIRS. Sci Rep 2019 Apr 4;9(1):5645. [doi: 10.1038/s41598-019-42098-w] [Medline: 30948760]
17. Posada-Quintero HF, Kong Y, Chon KH. Objective pain stimulation intensity and pain sensation assessment using machine learning classification and regression based on electrodermal activity. Am J Physiol Regul Integr Comp Physiol 2021 Aug 1;321(2):R186-R196. [doi: 10.1152/ajpregu.00094.2021] [Medline: 34133246]
18. Ghita M, Ghita M, Copot D, Ionescu CM. Methodologically study for detection of thermal induced pain via skin impedance. : IEEE Presented at: 2019 IEEE 17th World Symposium on Applied Machine Intelligence and Informatics (SAMI); Jan 24-26, 2019; Herlany, Slovakia. [doi: 10.1109/SAMI.2019.8782776]

19. Lucey P, Cohn JF, Prkachin KM, Solomon PE, Matthews I. Painful data: the unbcmcmaster shoulder pain expression archive database. Presented at: 2011 IEEE International Conference on Automatic Face & Gesture Recognition (FG); Mar 21-25, 2011; Santa Barbara, CA, USA. [doi: 10.1109/FG.2011.5771462]
20. Saccò M, Meschi M, Regolisti G, et al. The relationship between blood pressure and pain. J Clinical Hypertension 2013 Aug;15(8):600-605. [doi: 10.1111/jch.12145]
21. Thiam P, Kessler V, Amirian M, et al. Multi-modal pain intensity recognition based on the SenseEmotion database. IEEE Trans Affective Comput 2019;12(3):743-760. [doi: 10.1109/TAFFC.2019.2892090]
22. Moscato S, Zhu W, Guo Y, et al. Comparison of autonomic signals between healthy subjects and chronic low back pain patients at rest and during noxious stimulation. Presented at: 8th National Congress of Bioengineering, GNB 2023 - Proceedings; Jun 21-23, 2023; Padova, Italy.
23. Lötsch J, Ultsch A, Kalso E. Prediction of persistent post-surgery pain by preoperative cold pain sensitivity: biomarker development with machine-learning-derived analysis. Br J Anaesth 2017 Oct 1;119(4):821-829. [doi: 10.1093/bja/aex236] [Medline: 29121286]
24. Fetz K, Lefering R, Kaske S. Pre-trauma pain is the strongest predictor of persistent enhanced pain patterns after severe trauma: results of a single-centre retrospective study. Medicina (Kaunas) 2023 Jul 19;59(7):1327. [doi: 10.3390/medicina59071327] [Medline: 37512138]
25. Clay FJ, Watson WL, Newstead SV, McClure RJ. A systematic review of early prognostic factors for persisting pain following acute orthopedic trauma. Pain Res Manag 2012;17(1):35-44. [doi: 10.1155/2012/935194] [Medline: 22518366]
26. Lee JY, Fakhereddin M, MacDermid JC, Elliott JM, Schabrun SM, Walton DM. An exploration of blood marker×environment interaction effects on pain severity and interference scores in people with acute musculoskeletal trauma. Clin J Pain 2021 Oct 1;37(10):747-758. [doi: 10.1097/AJP.0000000000000961] [Medline: 34292185]
27. Raza MM, Zaslansky R, Gordon DB, et al. Chronic breast pain prior to breast cancer surgery is associated with worse acute postoperative pain outcomes. J Clin Med 2021 Apr 27;10(9):1887. [doi: 10.3390/jcm10091887] [Medline: 33925567]
28. Posada-Quintero HF, Chon KH. Innovations in electrodermal activity data collection and signal processing: a systematic review. Sensors (Basel) 2020 Jan 15;20(2). [doi: 10.3390/s20020479] [Medline: 31952141]
29. Subramanian S, Barbieri R, Brown EN. Point process temporal structure characterizes electrodermal activity. Proc Natl Acad Sci U S A 2020 Oct 20;117(42):26422-26428. [doi: 10.1073/pnas.2004403117] [Medline: 33008878]
30. Horvers A, Tombeng N, Bosse T, Lazonder AW, Molenaar I. Detecting emotions through electrodermal activity in learning contexts: a systematic review. Sensors (Basel) 2021 Nov 26;21(23):7869. [doi: 10.3390/s21237869] [Medline: 34883870]
31. Li S, Sung B, Lin Y, Mitas O. Electrodermal activity measure: a methodological review. Ann Tour Res 2022 Sep;96:103460. [doi: 10.1016/j.annals.2022.103460]
32. Braithwaite JJ, Watson DG, Jones R, Rowe M. A guide for analysing electrodermal activity (EDA) & skin conductance responses (SCRS) for psychological experiments. Psychophysiology 2013;49(1):1017-1034.
33. Subramaniam SD, Dass B. Automated Nociceptive pain assessment using physiological signals and a hybrid deep learning network. IEEE Sensors J 2020;21(3):3335-3343. [doi: 10.1109/JSEN.2020.3023656]
34. Kusumaningrum A, Rustina Y, Abuzairi T, Ibrahim N. The skin conductance-based non-invasive pain assessment instrument for infants. Sri Lanka J Child Health 2022;51(3):448. [doi: 10.4038/sljch.v51i3.10249]
35. Gohel V, Mehendale N. Review on electromyography signal acquisition and processing. Biophys Rev 2020 Nov 10;12(6):1361-1367. [doi: 10.1007/s12551-020-00770-w] [Medline: 33169207]
36. Simao M, Mendes N, Gibaru O, Neto P. A review on electromyography decoding and pattern recognition for human-machine interaction. IEEE Access 2019;7:39564-39582. [doi: 10.1109/ACCESS.2019.2906584]
37. Geisser ME, Ranavaya M, Haig AJ, et al. A meta-analytic review of surface electromyography among persons with low back pain and normal, healthy controls. J Pain 2005 Nov;6(11):711-726. [doi: 10.1016/j.jpain.2005.06.008] [Medline: 16275595]
38. Kelati A, Nigussie E, Dhaou IB, Plosila J, Tenhunen H. Real-Time classification of pain level using zygomaticus and corrugator EMG features. Electronics (Basel) 2022;11(11):1671. [doi: 10.3390/electronics11111671]
39. Gruss S, Treister R, Werner P, et al. Pain intensity recognition rates via biopotential feature patterns with support vector machines. PLoS One 2015;10(10):e0140330. [doi: 10.1371/journal.pone.0140330] [Medline: 26474183]
40. van Bruinessen IR, van den Ende ITA, Visser LNC, van Dulmen S. The impact of watching educational video clips on analogue patients' physiological arousal and information recall. Patient Educ Couns 2016 Feb;99(2):243-249. [doi: 10.1016/j.pec.2015.08.022] [Medline: 26427309]
41. Ree A, Mayo LM, Leknes S, Sailer U. Touch targeting C-tactile afferent fibers has a unique physiological pattern: a combined electrodermal and facial electromyography study. Biol Psychol 2019 Jan;140:55-63. [doi: 10.1016/j.biopsycho.2018.11.006] [Medline: 30468895]
42. Heesink L, Geuze E. Pre-processing of electromyography startle data: a novel semi-automatic method. Presented at: Proceedings of Measuring Behavior; Aug 27-29, 2014; Wageningen, The Netherlands.
43. Lubba CH, Sethi SS, Knaute P, Schultz SR, Fulcher BD, Jones NS. catch22: canonical time-series characteristics: selected through highly comparative time-series analysis. Data Min Knowl Discov 2019;33(6):1821-1852. [doi: 10.1007/s10618-019-00647-x]

44. Mietus JE, Peng CK, Henry I, Goldsmith RL, Goldberger AL. The pNNx files: re-examining a widely used heart rate variability measure. Heart 2002 Oct;88(4):378-380. [doi: 10.1136/heart.88.4.378] [Medline: 12231596]
45. Wang X, Wirth A, Wang L. Structure-based statistical features and multivariate time series clustering. Presented at: Seventh IEEE international conference on data mining (ICDM 2007); Oct 28-31, 2007; Omaha, NE, USA.
46. Walpole RE, Myers RH, Myers SL, Ye K. Probability and Statistics for Engineers and Scientists: Macmillan; 1993, Vol. 5.
47. St»hle L, Wold S. Analysis of variance (ANOVA). Chemometr Intell Lab Syst 1989 Nov;6(4):259-272. [doi: 10.1016/0169-7439(89)80095-4]

Abbreviations

EDA: electrodermal activity
EMG: electromyography
RMS: root mean square

Edited by J Shaikh-Mohammed; submitted 09.01.25; peer-reviewed by J Henderson, Y Li; revised version received 19.06.25; accepted 20.06.25; published 20.08.25.

Please cite as:
Ozek B, Lu Z, Radhakrishnan S, Kamarthi S
Influence of Pre-Existing Pain on the Body's Response to External Pain Stimuli: Experimental Study
JMIR Biomed Eng 2025;10:e70938
URL: https://biomedeng.jmir.org/2025/1/e70938
doi:10.2196/70938

Research Letter

Can Artificial Intelligence Diagnose Knee Osteoarthritis?

Mihir Tandon[1], BA; Nitin Chetla[2], BS; Adarsh Mallepally[3]; Botan Zebari[4], BS; Sai Samayamanthula[2], BA; Jonathan Silva[1], BS; Swapna Vaja[5], BS; John Chen[1], BS; Matthew Cullen[1], BS; Kunal Sukhija[6], MD

[1]Albany Medical College, Albany, NY, United States

[2]University of Virginia School of Medicine, Charlottesville, VA, United States

[3]School of Medicine, Virginia Commonwealth University, Richmond, United States

[4]St. James School of Medicine, Binghamton, NY, United States

[5]Rush Medical College, Chicago, IL, United States

[6]Kaweah Health, Visalia, CA, United States

Corresponding Author:
Mihir Tandon, BA
Albany Medical College
43 New Scotland Ave
Albany, NY, 12208
United States
Phone: 1 3322488708
Email: tandonm@amc.edu

Abstract

This study analyzed the capability of GPT-4o to properly identify knee osteoarthritis and found that the model had good sensitivity but poor specificity in identifying knee osteoarthritis; patients and clinicians should practice caution when using GPT-4o for image analysis in knee osteoarthritis.

(JMIR Biomed Eng 2025;10:e67481) doi:10.2196/67481

KEYWORDS

large language model; ChatGPT; GPT-4o; radiology; osteoarthritis; machine learning; X-rays; osteoarthritis detection

Introduction

Osteoarthritis often affects the knee, causing pain and disability, and is typically diagnosed by X-ray [1]. Advancements in artificial intelligence (AI) offer potential to automate image analysis, reducing diagnostic burden [2]. Given its widespread availability, tools like ChatGPT have potential as point-of-care diagnostic aids. AI has already been incorporated on the physician side through clinical decision support systems and robotic surgery. On the patient side, AI is used in applications such as virtual health assistants [3].

Orthopedic surgeons, radiologists, and primary care physicians can use AI tools to streamline their workflows and reduce errors while analyzing imaging for pathologies like osteoarthritis. Moreover, patients use ChatGPT to analyze their imaging to further understand their condition [4]. The ability of AI to read other radiological images (eg, computed tomography angiograms) has been shown to be subpar [5]. However, studies have shown that AI can perform well with X-rays [6]. As such, it is increasingly important for physicians to understand AI's strengths and limitations to assess its use in imaging and guide patients using AI for self-diagnosis.

Methods

We queried ChatGPT (using the GPT-4o version) and assessed its performance in classifying 500 X-ray images of normal knees and 500 images of knees with osteoarthritis from a publicly available Kaggle database [7]. Images were verified based on consensus among radiologists. A single standardized prompt was used: "This is an x-ray image found on examination, the multiple-choice question is as follows. Based on the x-ray image, does the patient have A) no osteoarthritis, B) osteoarthritis." Key metrics included accuracy, sensitivity, and specificity. No images were rejected by ChatGPT. The code used for statistical analysis is included in Multimedia Appendix 1.

Results

The model's performance in distinguishing osteoarthritis from nonosteoarthritis knee X-rays was mixed. The high recall (0.950, 95% CI 0.964-0.943) suggests that the model was sensitive in

identifying arthritis cases, while the low specificity (0.114, 95% CI 0.134-0.104) indicated a poor ability to correctly identify nonosteoarthritis cases. The F_1-score (0.670, 95% CI 0.699-0.655) balanced precision and recall, showing moderate effectiveness, but the precision (0.517, 95% CI 0.548-0.501) reflected that about half the predicted osteoarthritis cases were correct. Accuracy was 0.532 (95% CI 0.563-0.516). Figure 1 shows sensitivity and specificity.

The binomial test, where the null hypothesis assumed the model's accuracy was 50% or less, indicated that the model was statistically better than random chance (P=.02). Additionally, the χ^2 test (P<.001) indicated a strong dependence between the model's predictions and the actual labels, demonstrating that its classifications were not purely random. However, the significance of this test should be interpreted with caution, as it does not necessarily reflect high accuracy or clinical reliability.

Figure 1. Sensitivity and specificity of Chat-GPT4o in analyzing knee osteoarthritis X-rays.

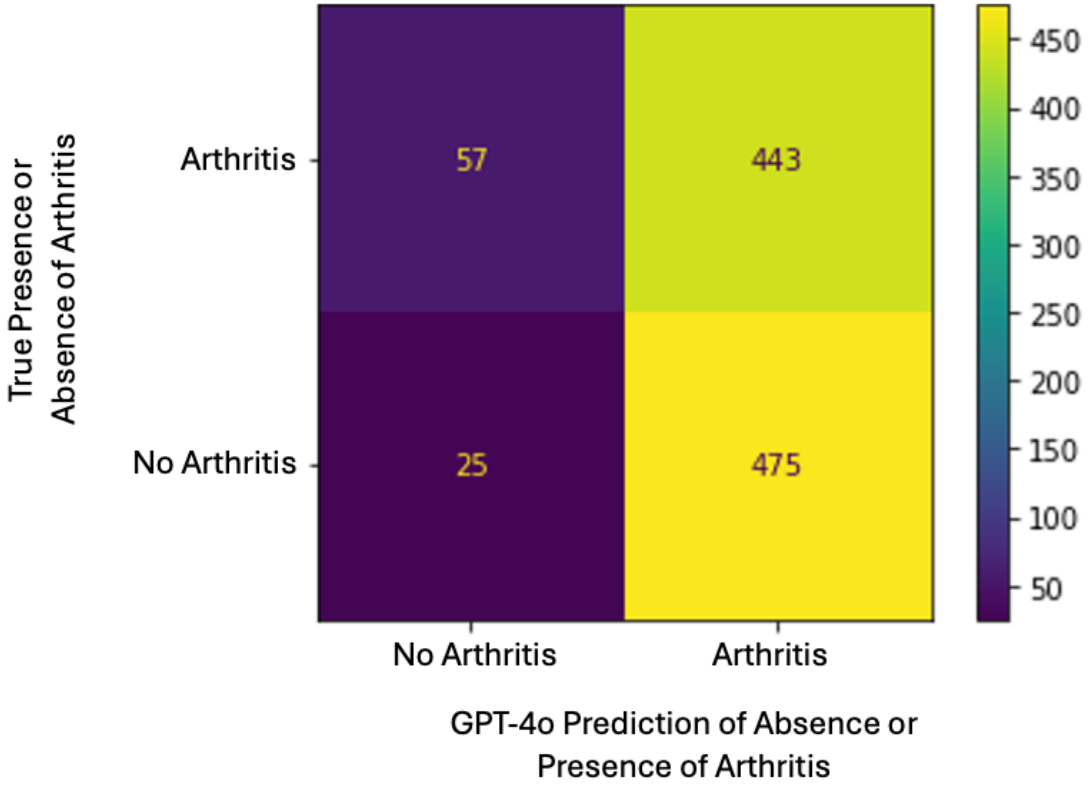

Discussion

The model had difficulty distinguishing between "not arthritis" and "arthritis." While the recall for arthritis was high (0.950), indicating strong performance in identifying true arthritis cases, the low specificity (0.114) reflects a significant number of false positives, with many nonarthritis cases misclassified as arthritis. This bias toward predicting arthritis lowered precision (0.517) and accuracy (0.532); similar misclassification issues have been reported in other ChatGPT studies [8].

Limitations include, first, that the prompt was binary. A binary prompt was used because it would have been difficult to analyze data obtained with an open-ended prompt. Second, the dataset was small; a larger dataset would have yielded more robust conclusions.

Even with its limitations, this study presents important data on GPT4o's use in imaging for diagnosing osteoarthritis. This is vital, as our understanding of tools like this in health care contexts is limited. These results suggest a need for better class balance and improved feature differentiation. Similar misclassification patterns have been noted in previous studies, where overlapping features led to false positives [9]. A higher-resolution, more comprehensively annotated osteoarthritis dataset could improve model training, enhancing overall accuracy, sensitivity, and specificity. Thus, future work should focus on analyzing larger datasets and refining the model to handle more nuanced cases more effectively, improving performance statistics. Using image preprocessing techniques, such as contrast enhancement and noise reduction, and including metadata like medical history and clinical presentation could also help distinguish osteoarthritis from anatomical variations.

Our results suggest that clinicians should use ChatGPT cautiously and as a screening tool prior to their own validation to help mitigate misclassification. Clinicians should also educate patients about the risks of using AI for self-diagnosis of osteoarthritis based on X-rays. Despite its shortcomings, AI has potential for developing more reliable diagnostic models for osteoarthritis.

Conflicts of Interest

None declared.

Multimedia Appendix 1
Code for analysis and prompting.
[DOCX File , 17 KB - biomedeng_v10i1e67481_app1.docx]

References

1. Choi MS, Lee DK. The effect of knee joint traction therapy on pain, physical function, and depression in patients with degenerative arthritis. J Kor Phys Ther 2019 Oct 31;31(5):317-321 [FREE Full text] [doi: 10.18857/jkpt.2019.31.5.317]
2. Bejarano A. The benefits of artificial intelligence in radiology: transforming healthcare through enhanced diagnostics and workflow efficiency. Rev Contemp Sci Acad Stud 2023 Aug 30;3(8):1-4. [doi: 10.55454/rcsas.3.08.2023.005]
3. Chatterjee I, Ghosh R, Sarkar S, Das K, Kundu M. Revolutionizing innovations and impact of artificial intelligence in healthcare. Int J Multidiscip Res 2024 May 14;6(3):19333. [doi: 10.36948/ijfmr.2024.v06i03.19333]
4. Zhang Z, Citardi D, Wang D, Genc Y, Shan J, Fan X. Patients' perceptions of using artificial intelligence (AI)-based technology to comprehend radiology imaging data. Health Informatics J 2021;27(2):14604582211011215 [FREE Full text] [doi: 10.1177/14604582211011215] [Medline: 33913359]
5. Young A, Tan K, Tariq F, Jin MX, Bluestone AY. Rogue AI: cautionary cases in neuroradiology and what we can learn from them. Cureus 2024 Mar;16(3):e56317 [FREE Full text] [doi: 10.7759/cureus.56317] [Medline: 38628986]
6. Wu JT, Wong KCL, Gur Y, Ansari N, Karargyris A, Sharma A, et al. Comparison of chest radiograph interpretations by artificial intelligence algorithm vs radiology residents. JAMA Netw Open 2020 Oct 01;3(10):e2022779 [FREE Full text] [doi: 10.1001/jamanetworkopen.2020.22779] [Medline: 33034642]
7. Kabir F. Osteoarthritis prediction. Kaggle. URL: https://www.kaggle.com/datasets/farjanakabirsamanta/osteoarthritis-prediction [accessed 2024-09-01]
8. Dalalah D, Dalalah OM. The false positives and false negatives of generative AI detection tools in education and academic research: the case of ChatGPT. Int J Manag Educ 2023 Jul;21(2):100822. [doi: 10.1016/j.ijme.2023.100822]
9. Truhn D, Weber CD, Braun BJ, Bressem K, Kather JN, Kuhl C, et al. A pilot study on the efficacy of GPT-4 in providing orthopedic treatment recommendations from MRI reports. Sci Rep 2023 Dec 17;13(1):20159 [FREE Full text] [doi: 10.1038/s41598-023-47500-2] [Medline: 37978240]

Abbreviations

AI: artificial intelligence

Edited by S Rizvi, T Leung; submitted 12.10.24; peer-reviewed by Y Chaibi, A Jahnen, M Nayak; comments to author 25.02.25; revised version received 13.03.25; accepted 25.03.25; published 23.04.25.

Please cite as:
Tandon M, Chetla N, Mallepally A, Zebari B, Samayamanthula S, Silva J, Vaja S, Chen J, Cullen M, Sukhija K
Can Artificial Intelligence Diagnose Knee Osteoarthritis?
JMIR Biomed Eng 2025;10:e67481
URL: https://biomedeng.jmir.org/2025/1/e67481
doi:10.2196/67481
PMID:40266670

Publisher:
JMIR Publications
130 Queens Quay East.
Toronto, ON, M5A 3Y5
Phone: (+1) 416-583-2040
Email: support@jmir.org